Quantum Nonlocality with Spins in Diamond

Hensen, Bas

DOI
10.4233/uuid:b307dca0-79a4-4cc9-af91-a2927a61088e

Publication date
2016

Document Version
Final published version

Citation (APA)
Hensen, B. (2016). *Quantum Nonlocality with Spins in Diamond* (Casimir PhD Series Delft-Leiden 2016-11 ed.). [Dissertation (TU Delft), Delft University of Technology]. https://doi.org/10.4233/uuid:b307dca0-79a4-4cc9-af91-a2927a61088e

Quantum Nonlocality with Spins in Diamond

Bas Jorrit Hensen

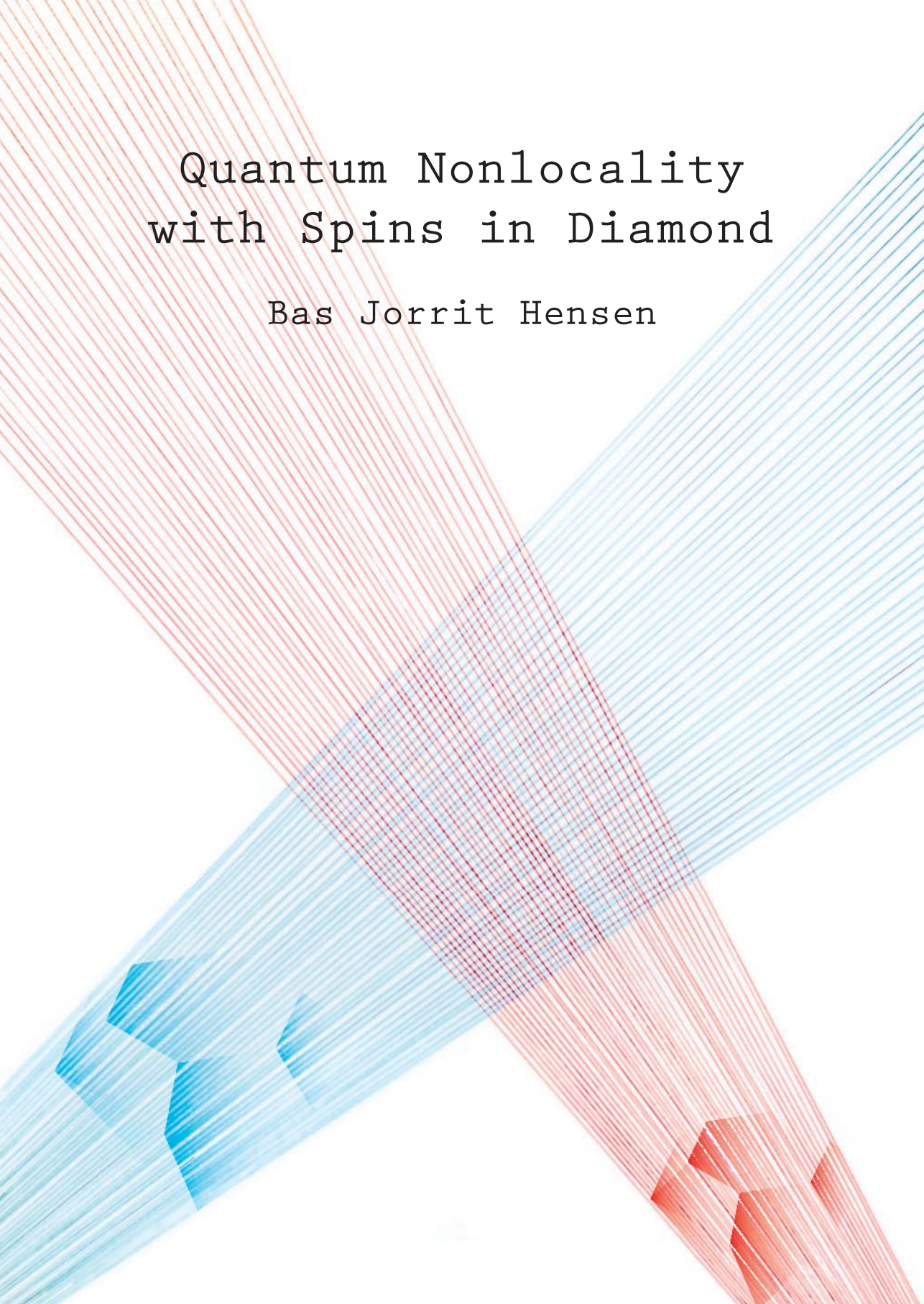

Quantum Nonlocality with Spins in Diamond

Quantum Nonlocality with Spins in Diamond

Proefschrift

ter verkrijging van de graad van doctor
aan de Technische Universtiteit Delft,
op gezag van de Rector Magnificus Prof. ir. K.C.A.M. Luyben,
voorzitter van het College voor Promoties,
in het openbaar te verdedigen op vrijdag 29 april 2016 om 10:00 uur

door

Bas Jorrit HENSEN

Master of Science in Applied Physics
Technische Universiteit Delft, Nederland
geboren te Leiden, Nederland

This dissertation has been approved by the promotor:
Prof. dr. ir. R. Hanson

Composition of the doctoral committee:

Rector Magnificus,	chairman
Prof. dr. ir. R. Hanson,	Delft University of Technology, promotor

Independent members:

Prof. dr. ir. J.E. Mooij,	Delft University of Technology
Prof. dr. ir. L.M.K. Vandersypen,	Delft University of Technology
Prof. dr. N. Gisin,	Université de Genève, GAP-Optique
Prof. dr. D.G.B.J. Dieks,	Utrecht University
Prof. dr. A.F. Koenderink	University of Amsterdam

ISBN 978-90-8593-253-6

Casimir PhD Series Delft-Leiden 2016-11

Cover based on designs by Studio KNOL

Printed by Gildeprint - www.gildeprint.nl

An electronic version of this thesis is available at www.library.tudelft.nl/dissertations

Contents

1 Introduction **1**
1.1 Quantum Information Processing 2
1.1.1 Quantum computation 3
1.1.2 Quantum communication 4
1.2 Entangled Particles and Bell's theorem 4
1.2.1 Locality 5
1.2.2 Bell's test of local causality 6
1.2.3 Experimental Bell test 8
1.2.4 Device independence 10
1.3 The nitrogen-vacancy centre for quantum technologies and fundamental tests 11
1.4 Thesis overview 11
1.5 Bibliography 13

2 Methods **19**
2.1 The NV centre in diamond 20
2.1.1 Defect structure 20
2.1.2 Orbital ground state manifold and hyperfine interactions 21
2.1.3 Transitions, rates and temperature effects 23
2.1.4 The neutral charge state 23
2.2 Device fabrication 25
2.3 Experimental control setup 27
2.4 Initialization, control and readout 27
2.4.1 Electron spin initialisation 29
2.4.2 Electron spin readout 30
2.4.3 Spin control 30
2.4.4 Nuclear spin initialisation and readout 31
2.4.5 Charge state initialization and spectral diffusion 32
2.4.6 Laser stabilization and feedback 35
2.5 Remote entanglement generation 37
2.5.1 Barret and Kok scheme 37

2.6 Bibliography 39

3 Heralded entanglement between remote qubits 43
3.1 Introduction 44
3.2 Heralded entanglement 44
3.3 Implementation 47
3.4 Demonstration of remote entanglement 49
3.5 Conclusion 51
3.6 Supplementary Information 52
3.6.1 Setup 52
3.6.2 Rejection of resonant excitation light 53
3.6.3 Experimental control 53
3.6.4 Optical Rabi oscillations 55
3.6.5 Fidelity measure 55
3.6.6 Spin readout 56
3.6.7 Single-shot readout characterisation 57
3.6.8 Maximum likelihood estimate of the state probabilities 58
3.6.9 Error estimates 60
3.6.10 TPQI signature 66
3.6.11 Phase of the entangled state 67
3.6.12 Relation to TPQI visibility 69
3.7 Bibliography 71

4 Unconditional teleportation between remote qubits 75
4.1 Introduction 76
4.2 Implementation 77
4.3 Results 81
4.4 Conclusion 81
4.5 Supplementary Information 82
4.5.1 Conventions 82
4.5.2 Desired state evolution 82
4.5.3 Data analysis 85
4.5.4 Error model 85
4.5.5 Further analysis of the teleporter performance 88
4.6 Bibliography 96

5 A loophole-free Bell test 99
5.1 Introduction 100
5.2 Implementation 102
5.3 Results 106
5.4 Second run 108
5.5 Combined P-value for the two tests 110
5.6 Choosing different heralding window settings in post-processing 111

5.7 Bell violation for shorter readout duration . . . 112
5.8 Conclusion . . . 113
5.9 Supplementary Information - Experimental . . . 114
5.9.1 Experimental setup . . . 114
5.9.2 Two-photon quantum interference (Fig. 5.4b) . . . 115
5.9.3 Model of the entangled state (Figs. 5.4c and 5.5a) . . . 116
5.9.4 Dynamical decoupling sequence . . . 117
5.9.5 Event-ready signal settings . . . 117
5.9.6 Location and distances . . . 118
5.9.7 Synchronisation of the experimental setups . . . 118
5.9.8 Random number generation . . . 120
5.9.9 Experimental control and stability . . . 121
5.9.10 Data recording and processing . . . 123
5.9.11 Stabilization of the excitation laser frequency . . . 126
5.9.12 Adaptive optics . . . 127
5.10 Supplementary Information - Statistical Analysis . . . 128
5.10.1 How to compute the P-value . . . 129
5.10.2 Properties of the tested models . . . 130
5.10.3 Proof outline . . . 131
5.11 Supplementary Information - Second dataset . . . 132
5.11.1 Random numbers from Twitter . . . 132
5.11.2 APD replacement . . . 133
5.11.3 Joint P-value for psi-minus and psi-plus heralded events . . . 133
5.11.4 Statistical analysis of settings choices . . . 134
5.12 Bibliography . . . 138

6 Conclusions and outlook **143**
6.1 Conclusions . . . 143
6.2 Foundational experiments . . . 144
6.3 Towards quantum networks with spins in diamond . . . 145
6.4 Bibliography . . . 148

Appendix **150**

Summary **151**

Samenvatting **153**

Acknowledgements **155**

List of Publications **159**

Curriculum Vitae **161**

Chapter 1

Introduction

B.J. Hensen

> *But if they mean that the thing is performed without any mechanism by a simple primitive quality or by a law of God who produces that effect without using any intelligible means, it is an unreasonable and occult quality, and so very occult that it is impossible that it should ever be done though an angel or God himself should undertake to explain it.*
>
> —Leibniz, referring to gravity in a letter to Newton (1693) [1]

Quantum nonlocality refers to the various aspects of non-separable quantum states describing physically separated systems. On the one hand, such *entangled* states are at the basis of the many phenomena that make quantum theory difficult to interpret philosophically: the interaction with a measurement apparatus and the subsequent measurement back-action; the consequent non-contextuality of quantum measurement; and last but not least the non-local structure of the theory itself. On the other hand, entangled states are also at the basis of many quantum advantages for tasks in information theory, for example, factoring a large number using a quantum computer running Shor's algorithm, or performing quantum key distribution using a Bell test certified quantum communication channel.

In this chapter an introduction is given to those aspects of quantum nonlocality that are central to the work in this thesis, starting from the application perspective in quantum information processing, and zooming in on the foundational aspect of Bell nonlocality. Additionally we briefly introduce the quantum system used in this thesis, the nitrogen-vacancy (NV) centre, introduced in more detail in the next chapter.

1.1 Quantum Information Processing

The field of quantum information attempts to study and realize applications of quantum theory in the world of information science. Roughly, it can be divided into two categories: quantum computation and quantum communication. In this thesis the focus is on an essential ingredient in both computation and communication applications: creating links of entanglement between isolated quantum systems. In particular, the entanglement is created over human-scale distances using a flying (photonic) quantum link. Such remote entanglement forms the linking operation in a future quantum network, linking together multiple (small) quantum processing units to make a larger one. It also lies at the basis of (device independent) quantum key distribution and randomness generation protocols.

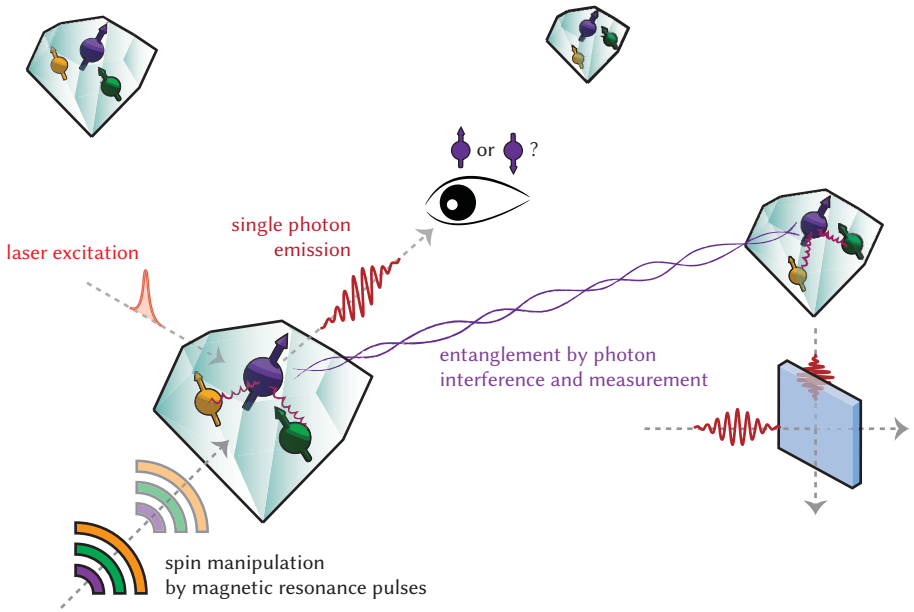

Figure 1.1 — Figure from Pfaff[2] **Vision of a macroscopic quantum network based on spins in diamond.** Nodes consist of single NV centres in diamonds that are separated by macroscopic distances (metres up to kilometres). The NV electronic spin (purple) can be measured optically, and serves as the interface for a quantum register of nuclear spins (orange, green). Entanglement between nodes is established by interference and measurement of photons that are correlated with the electron spins.

1.1.1 Quantum computation

The interest in quantum computation was sparked in the 1980s and 1990s, by the realisation of Deutch, Shor, Grover and others that certain problems in mathematics for which no efficient* algorithmic solution was known, could be solved efficiently on a computer consisting of binary quantum systems (qubits), where the algorithm consisted of a set of unitary operations between those qubits[3].

Additionally, quantum information processing could help to overcome limitations in simulating quantum systems using classical computing[4]. For example, suppose we want to simulate a molecule of 500 degrees of freedom, where each of those dimensions has at least two possible states. The full state information consists of the complex amplitudes of all $\geq 2^{500}$ terms in a general superposition state — more numbers than the estimated total of atoms in the observable universe and thus certainly intractable by any classical computer. However, if controlled and preserved well enough, a quantum system that can be mapped to the very molecule to be described can be used for the task. This idea has been generalized to show that any quantum system can be simulated efficiently on a quantum computer[5].

Capitalising on these potential applications requires unprecedented control over quantum systems. It requires a quantum system that can be controlled and read out and can be shielded from interactions with its environment. At the same time it requires coupling of multiple quantum systems while retaining this shielding from the rest of the world.

For a while it was thought a quantum computer would face similar issues as the existing field of analog computation: promised speed-ups would not be attainable in practice due to the finite precision of operating a continuous computational basis. These doubts were invalidated by the development of quantum error correction codes[3] in the 1990s and the discovery of fault tolerance thresholds for quantum operations, above which scaling to a larger system reduces the overall error in the computation. Recent developments of topological error correction codes[6] have further minimized the required operation fidelities and number of qubits to a regime that no longer seems prohibitively large.

A final reason why developing a quantum computer is considered an important effort, is to study the interplay between quantum mechanics and the observed classical world. It might turn out that nature prohibits the increasingly large entangled states required for the operation of a quantum computer. However, such a barrier would have to result from fundamentally new physics, a prospect considered by some to be even more exciting than the realisation of a quantum computer itself.

*running on a space / in a time polynomial with the problem size

1.1.2 Quantum communication

Another important field where quantum theory may provide an operational advantage is in communication.

The most well known examples are in cryptography, involving communication between parties that might not trust each other or the communication channel they operate. One important task in cryptography is the distribution of a secure key between two trusted parties. Any message sent by encrypting it (for binary messages the encryption would just be a bitwise XOR operation) with a one time use of a random key shared between the two parties is secure against eavesdropping. The main problem is then: how to distribute the keys? In 1984, Bennett and Brassard[7] developed a quantum key distribution protocol, allowing secure distribution of private random keys between two parties by sending individual quantum bits. The protocol relies on the fundamental quantum measurement back-action, that disturbs the sent qubits if eavesdropped. Notably, an equivalent protocol[8] can be implemented using two qubits that are in an entangled state.

Similarly to quantum computation, many applications in quantum communication require high fidelity control over quantum systems. However, often only two, or few qubits are sufficient to show a quantum advantage over the best known classical implementation. For example, a system implementing quantum key distribution over few kilometre distances is already available commercially[†].

1.2 Entangled Particles and Bell's theorem

Consider two electrons, whose spin degree of freedom is brought into the maximally entangled singlet state:

$$\left|\Psi^-\right\rangle = \frac{1}{\sqrt{2}}(\left|\uparrow\right\rangle_A \left|\downarrow\right\rangle_B - \left|\downarrow\right\rangle_A \left|\uparrow\right\rangle_B). \tag{1.1}$$

The electrons are spatially separated, and under control of Alice and Bob, labelled A and B.

Suppose A performs a measurement of the spin along Z with the observable $\hat{S}_z = (+1)\mathbb{P}_\uparrow + (-1)\mathbb{P}_\downarrow = \left|\uparrow\right\rangle\left\langle\uparrow\right| - \left|\downarrow\right\rangle\left\langle\downarrow\right|$. With probability $\frac{1}{2}$ she will find outcome $+1$, which leaves the post-measurement state

$$\left|\Phi'\right\rangle = \frac{(\mathbb{P}_\uparrow \otimes \mathbb{I}^{(B)})\left|\Phi^+\right\rangle}{\sqrt{\frac{1}{2}}} = \left|\uparrow\right\rangle_A \left|\downarrow\right\rangle_B, \tag{1.2}$$

where $\mathbb{I}$ denotes the identity operator. If subsequently B measures the spin of his electron along Z, clearly he will find the opposite outcome to A, -1 with unit

[†] ID Quantique, www.idquantique.com

probability. The same anti-correlation holds for A's outcome -1, and, remarkably, for co-aligned measurements for A and B along any axis.

These predictions bothered Einstein, Podolsky and Rosen[9,10]. In their 1935 paper on the subject[9] they concluded that the quantum mechanical description is incomplete. For example, perhaps the correlations are pre-set in some variables λ carried by each of the electrons, but these are hidden from us: a local-hidden variable explanation of the behaviour[10].

In 1964, John Bell showed[11,12] that no such local-hidden variable explanation can reproduce the statistical predictions of quantum theory for the system of equation (1.1). This meant that quantum theory could not be supplemented with an additional theory that 'fixed' the non-local behaviour.

There exists an overwhelming amount of literature on Bell's theorem, its implications and applications. For a recent operational review see for instance Brunner *et al.*[13]. For an overview of the underlying philosophical principles and a historical background, see for example Wiseman and Cavalcanti[14]. Additionally, the October 2014 issue of Journal of Physics A was devoted to Fifty years of Bell's theorem[15] and contains a comprehensive overview of recent developments and historical background.

In this Section we will try to summarize the arguments presented by Bell in the final chapter of his landmark book[16], aiming to keep the main arguments and assumptions required to obtain the Bell inequality, but inevitably skipping many of the subtle points.

1.2.1 Locality

If two events A and B are correlated ($p(A,B) \neq p(A)p(B)$), then it is natural to try to find a causal explanation for this correlation. For instance B could be a direct effect of A ($p(B|A) = 1$), or vice versa, or A and B could have a direct common cause C ($p(A,B|C) = p(A|C)p(B|C)$). The idea that correlated events should be explainable is known as Reichenbach's principle:

> **Reichenbach's principle** If two sets of events $\mathbb{A}$ and $\mathbb{B}$ are correlated, and no event in either is a cause of any event in the other, then they have a set of common causes $\mathbb{C}$, such that conditioning on $\mathbb{C}$ eliminates the correlation. ($P(\mathbb{A},\mathbb{B}|\mathbb{C}) = P(\mathbb{A}|\mathbb{C})P(\mathbb{B}|\mathbb{C})$)

According to Einstein's theory of relativity, no effect should follow its cause sooner than light could have propagated from the place of the cause to the place of the effect. Consider an ordinary 'flat' region of Minkowski space-time, such as depicted in Fig. 1.2:

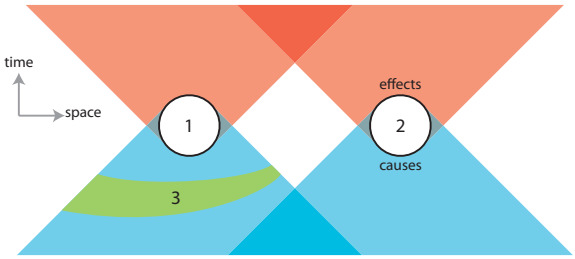

Figure 1.2 — Figure adapted from Bell[17]. Local causality: "Full specification of what happens in 3 makes events in 2 irrelevant for predictions about 1 in a locally causal theory." [17]

> **Relativistic causality** Events in an ordinary area of Minkowski space-time (for example region 1 in Fig. 1.2) can have effects only in its forward light cone (the red region in Fig. 1.2), and causes only in its backward light cone (the blue region in Fig. 1.2).

This concept ensures that superluminal signalling and communication is impossible.

Combining Reichenbach's principle and Relativistic causality leads to Bell's definition of local causality:

> **Local causality** If two space-like separated sets of events $\mathbb{A}$ and $\mathbb{B}$ are correlated, then there is a set of events $\mathbb{C}$ in their common Minkowski past light cone such that conditioning on $\mathbb{C}$ eliminates the correlation.

Indeed, in Fig. 1.2, events in areas 1 and 2 can be correlated, due to mutual causes located in the overlapping regions of their backward light cones. However under local causality, conditioning on the complete specification of events in space-time region 3 should eliminate the correlation between events in areas 1 and 2.

1.2.2 Bell's test of local causality

Bell's test involves two boxes labelled A and B (Fig. 1.3). Each box can accept a binary input (0 or 1) and subsequently delivers a binary output (+1 or −1). In each trial of the Bell test a random input bit is generated on each side and input to the respective box. The random input bit triggers the box to produce an output value, and both input and output bits are recorded. The test concerns correlations between the output values (labeled x and y for box A and B, respectively) and the input bits (labelled a and b for A and B respectively) generated within the same trial.

The goal of Bell's test is now to show that a theory T under investigation, describing the boxes behaviour, cannot be embedded in a locally causal theory, as described in

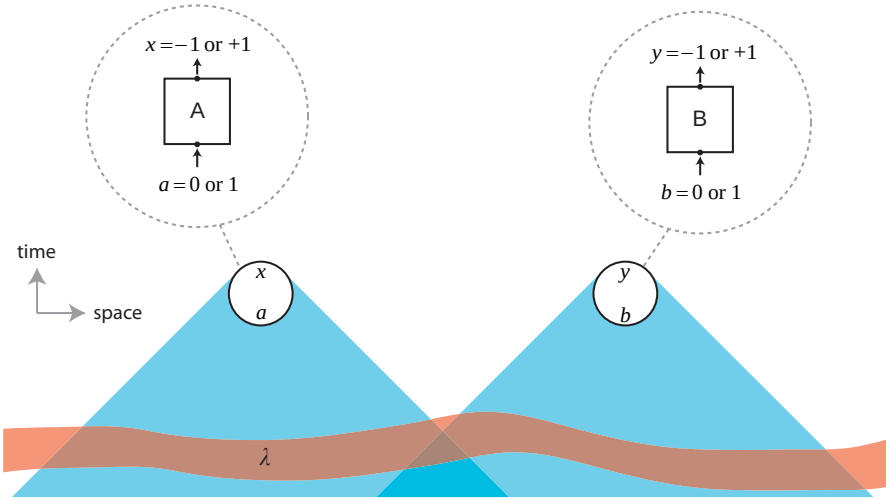

Figure 1.3 — Typical layout of a Bell test of local causality. Two boxes labelled A and B are located in space-like separated regions of a flat space-time. The Bell tests concerns the joint probability of the boxes' outputs x and y conditional on the inputs a and b, and hidden variables λ defined at a specific time (on a space-like hypersurface) in the past light cones of the areas containing the boxes.

Sec. 1.2.1. To do so, we need to be able to realize (if only in principle) the test setup as described above. In particular we need to assume:

(1) **Macro-reality** Once an output value exits the boxes, it can be recorded as a real objective value that cannot be changed, is not relative to anything, nor a probability distribution.

(2) **Minkowksi spacetime** The boxes A and B can be contained in an ordinary part of space-time as shown in Fig. 1.3, with relativistic light cones defined by the speed of light c, a definite arrow of time and without fancy structures like wormholes or closed time-like loops.

(3) **Free choice** Freely chosen bits exist that can be recorded and used as input to the boxes. The choices are free in the sense that they are uncorrelated with any other inputs to the boxes, known or unknown (in particular, of λ, see equation 1.7).

Under assumption (1), we can write a joint probability distribution for the outcomes[‡]

$$p(x, y|a, b, \lambda), \tag{1.3}$$

[‡]Here we are using the short hand notation, where actually $p(x, y|a, b, \lambda) = \text{Prob}(X = x, Y =$

conditional on the input values, and where λ denotes all additional variables, known or unknown, needed to describe the boxes' behaviour, according to theory T. For any theory T that satisfies local causality defined in Fig. 1.3, and using assumption (2), we can factorize the joint probability distribution of the outcomes:

$$p(x, y|a, b, \lambda) = p(x|a, \lambda)p(y|b, \lambda). \tag{1.4}$$

We then define:

$$S := \langle x \cdot y \rangle_{(0,0)} + \langle x \cdot y \rangle_{(0,1)} + \langle x \cdot y \rangle_{(1,0)} - \langle x \cdot y \rangle_{(1,1)}\,, \tag{1.5}$$

with

$$\langle x \cdot y \rangle_{(a,b)} := \sum_{\lambda} \sum_{x\in\{-1,+1\}} \sum_{y\in\{-1,+1\}} (xy)p(x, y|a, b, \lambda)p(\lambda|a, b). \tag{1.6}$$

Using assumption (3), we have:

$$p(\lambda|a, b) = p(\lambda). \tag{1.7}$$

Combining equations (1.4) - (1.7) we find the CHSH form of Bell's inequality[12,19,20]:

$$-2 \leq S \leq 2 \tag{1.8}$$

for any theory T that satisfies local causality. Dropping any of the assumptions (1)-(3), does not lead to the bound (1.8).

Considering quantum theory, suppose we take the electron spins from equation (1.1), and embed one each in the boxes A and B. Suppose the spin in box A is then measured along direction Z (for input bit $a = 0$) or X (for $a = 1$) and the spin in box B is measured along $(-\mathrm{Z} - \mathrm{X})/\sqrt{2}$ (for $b = 0$) or $(-\mathrm{Z} + \mathrm{X})/\sqrt{2}$ (for $b = 1$). If the measurement outcomes are used as outputs of the boxes, quantum theory predicts a value of

$$S = 2\sqrt{2}. \tag{1.9}$$

This shows that under assumptions (1)-(3), quantum theory cannot be embedded in a locally causal theory.

1.2.3 Experimental Bell test

The theoretical Bell test naturally extends to an experimental setting. In this case we conduct a finite number n sequential trials of the test described above, noting down all the inputs and outcomes. The goal is to bound the probability that the observed data

$y|A = a, B = b, \{\Lambda_i\} = \{\lambda_i\})$ and A, B and X, Y are discrete binary random variables describing the inputs and outputs respectively, and Λ_i is a set of additional random variables. For a rigorous derivation see for instance Brunner *et al.*[13], or for a specific analysis of the experiment described in Chapter 5, refer to the online Supplementary Information of Hensen *et al.*[18].

from the boxes can be explained by assuming some locally causal theory T. Strictly speaking, under the minimal set of assumptions (1-3), a theory can be experimentally tested using the Bell test if and only if it specifies at least:

(1b) where and when the output of each box can be accessed/recorded;

(3b) where and when the free choices for the input of each box can be accessed/recorded.

Only if such a specification is made can we bound the boxes A and B in space and time, so that we can situate them such that the input setting from one side cannot be communicated to the other side before the output is recorded.

We are especially interested in testing a subset of locally causal theories that we consider to be in agreement with our classical understanding of the world outside boxes A and B. For example, theories that predict two independently operating random number generators produce free choices for the inputs, and that recordings made in, for example, a desktop computer memory are fixed and real. Such theories are in agreement with our everyday understanding of the world, yet at the same time, by embedding the above described electron spins (or other entangled quantum systems) in boxes A and B, we can hope to falsify the hypothesis that these theories describe the inner workings of the boxes.

If we require additional assumptions about the inner workings of the boxes, or the way they might be connected to each other, this results in experimental *loopholes*, allowing violation of the Bell inequality, Eq. (1.8), without a violation of local causality or one of the assumptions (1)-(3). An experiment that needs no further assumptions to test such classical theories is commonly referred to as a *loophole-free* Bell test[21–23]. Two examples of common loopholes in experimental Bell tests are the *locality loophole*[13,24] and the *fair-sampling* or *detection loophole*[21,25]. The first does not ensure a separation of A and B far enough to exclude communication of the input settings before the outputs are recorded. The second allows a third outcome corresponding to a 'no-outcome' event. If trials with a no-outcome events are discarded, to obtain the correlators $\langle x \cdot y \rangle_{(a,b)}$, one effectively allows the boxes to select trials based on the input setting, allowing a local explanation of any observed violation. An experiment that closes both these loopholes is challenging, because fragile entangled quantum systems have to be separated far enough to close the locality loophole, while both the process of separation and the subsequent detection has to be done with high efficiency to close the detection loophole.

The first reported Bell test experiment was performed in 1972 by Friedman and Clauser[26], using entangled photons from an atomic cascade. They found a violation of the CHSH Bell inequality by 6 standard deviations. This experiment was open to both above loopholes, as many photons got lost and the polarisation analyser settings had to be manually rotated, thus measuring the four correlator terms in

successive runs. In 1982, Alain Aspect[27] used a photonic setup with fast time-varying polarisation analysers, allowing settings changes while the photons were already flying. The change of analyser setting on one side was space-like separated from the detection on the other side, thus convincingly addressing the locality loophole. Although the settings were chosen by an in principle quasi-periodic process, it seems natural to assume their functioning is uncorrelated. Subsequent photonic experiments improved by further restricting locality conditions[28–30]. The detection loophole was closed first using non-photonic systems, due to their more efficient detection[31–35]. Recently, improvements in entangled photon source and detector technology allowed a Bell violation free of the detection loophole with photons[36,37]. These experiments however could not address the locality loophole.

1.2.4 Device independence

An intuitive link between the Bell test and applications in quantum communication is provided by Ekert's protocol for quantum key distribution[8]: Suppose Alice and Bob want to establish a shared private key. They respectively operate boxes A and B, as described in Section 1.2.2. We now add a third possible input setting for box A, such that we have $a \in \{0, 1, 2\}$. Using again the entangled spins from equation (1.1) with the same measurement angles for $\{a, b\} \in \{0, 1\}$, Alice now chooses to measure along the $(-\mathrm{Z} - \mathrm{X})/\sqrt{2}$-axis for $a = 2$, parallel to the measurement done by Bob for $b = 0$. Then, using the subset of inputs and outputs corresponding to $\{a, b\} \in \{0, 1\}$ to check the Bell inequality Eq. (1.8), we can use the remaining subset $(a, b) = (2, 0)$ to generate a shared key that is perfectly correlated between A and B, but uncorrelated to the rest of the world[38]. Here the violation of the Bell inequality functions to limit the amount of correlation of the outcomes x, y with observations made by a potential eavesdropper, given, for instance, the validity of quantum theory.

The power of this idea is that in the above protocol outline, in particular for the violation of the Bell inequality, we did not need any specific knowledge of the way the boxes A,B are implemented. Indeed this idea led to the development of quantum key distribution that does not even need the assumption that quantum theory is universally correct[38], as long as superluminal signalling is impossible.

In this cryptographic perspective of certifying nonlocality, experimental loopholes in a Bell experiment take on a much more practical form: Any loophole could be exploited by an adversary to 'fake' the Bell test inequality violation[39], thereby letting Alice and Bob believe they share private randomness when in fact they do not.

In absence of experimental loopholes, no assumptions about the 'cryptographic devices' (the boxes A and B in Fig. 1.3) or the powers of an adversary are necessary, except that they are limited by the impossibility of superluminal signalling. This idea is called 'device independence' and various protocols in quantum communication have gained a device independent variant[40–42].

1.3 The nitrogen-vacancy centre for quantum technologies and fundamental tests

All experiments in this thesis are performed with single spins that are associated with the nitrogen-vacancy (NV) colour defect in diamond. The NV centre has attracted a lot of interest in experimental quantum physics since the first observation of a single NV centre in 1997[43]: the defect behaves much like a single ion or small molecule, but comes "pre-packaged" in a robust solid-state environment that protects the spin states, while it does not strongly interact with them.

Much pioneering work has been done to uncover the various features of the NV centre, both on the theory and on the experimental side, for a recent review, see Gao *et al.*[44], for a more theoretical background see for instance Doherty *et al.*[45]. The NV centre shows photoluminescence under excitation with visible light and is a stable single photon emitter[46]. It has an electronic spin that can be initialized and read out optically, and manipulated with standard magnetic resonance techniques[47]. Remarkably, these properties are available even at room temperature. As a result, the NV centre has been used for experiments in various aspects of quantum science, from sensitive metrology[48–51], studies of single-spin decoherence[52,53], to fundamental tests of quantum mechanics[54–56], to name only a few.

Recent critical advances show the potential for NV centres in quantum information processing: It has been shown that nuclear spins interacting with the NV electronic spin can be used as qubits[57–61], while at the same time the electronic spin's optical interface can be used for projective measurements[62] and allows spin-photon entanglement[63] at cryogenic temperatures. This opens up the possibility for building local multi-qubit quantum registers, that can be linked together using photons to form macroscopic networks for quantum communication[64] or even computation[65]. A cartoon of the architecture we envision is shown in Fig. 1.1 on page 2.

1.4 Thesis overview

Chapter 2 of this thesis provides a detailed description of the NV centre as well as the experimental methods used in this thesis. **Chapter 3** presents a key experiment where two electron spins in different diamonds, separated by 3 meters are entangled using a heralded protocol. This experiment enabled two further experiments, both the first of its kind, which are presented in the next chapters: In **Chapter 4** we present the first demonstration of unconditional quantum teleportation over human scale distances, from a nuclear spin qubit in one diamond to the electron spin of the other. This first demonstration of remote unconditional teleportation establishes the NV centre as a prime candidate for building quantum networks. Then in **Chapter 5**, we scale our setup from 3 meters to 1.3 kilometres, to enable the first loophole-free Bell test experiment. Such a loophole-free Bell test forms the basis for various proposed

device-independent quantum communication protocols.

1.5 Bibliography

[1] A. Janiak. *Isaac Newton: Philosophical Writings*. Cambridge University Press, Cambridge, UK (2004).

[2] W. Pfaff, R. Hanson and L. P. Kouwenhoven. *Quantum measurement and entanglement of spin quantum bits in diamond*. Ph.D. thesis, Delft University of Technology, Applied Sciences: Quantum Nanoscience (2013).

[3] M. A. Nielsen and I. L. Chuang. *Quantum Computation and Quantum Information*. Cambridge University Press, 1 edition (2004).

[4] R. Feynman. Simulating physics with computers. *International Journal of Theoretical Physics* **21**, 467 (1982).

[5] S. Lloyd. Universal quantum simulators. *Science* **273**, 1073 (1996).

[6] E. Dennis, A. Kitaev, A. Landahl and J. Preskill. Topological quantum memory. *Journal of Mathematical Physics* **43**, 4452 (2002).

[7] C. H. Bennett and G. Brassard. Quantum cryptography: Public key distribution and coin tossing. *Proceedings of IEEE International Conference on Computers, Systems and Signal Processing* **175**, 8 (1984).

[8] A. K. Ekert. Quantum cryptography based on bell's theorem. *Physical Review Letters* **67**, 661 (1991).

[9] A. Einstein, B. Podolsky and N. Rosen. Can quantum-mechanical description of physical reality be considered complete? *Physical Review* **47**, 777 (1935).

[10] D. Bohm and Y. Aharonov. Discussion of experimental proof for the paradox of einstein, rosen, and podolsky. *Physical Review* **108**, 1070 (1957).

[11] J. Bell. On the einstein-podolsky-rosen paradox. *Physics* **1**, 195 (1964).

[12] J. S. Bell. On the einstein-podolsky-rosen paradox. *Speakable and Unspeakable in Quantum Mechanics: Collected Papers on Quantum Philosophy*. Cambridge University Press (2004), 14–21.

[13] N. Brunner, D. Cavalcanti, S. Pironio, V. Scarani and S. Wehner. Bell nonlocality. *Reviews of Modern Physics* **86**, 419 (2014).

[14] H. M. Wiseman and E. G. Cavalcanti. Causarum investigatio and the two bell's theorems of john bell. *arXiv:1503.06413 [physics, physics:quant-ph]* (2015).

[15] N. Brunner, O. Gühne and M. Huber. Fifty years of bell's theorem. *Journal of Physics A: Mathematical and Theoretical* **47**, 420301 (2014).

[16] J. S. Bell. *Speakable and Unspeakable in Quantum Mechanics: Collected Papers on Quantum Philosophy*. Cambridge University Press, 2 edition (2004).

[17] J. S. Bell. La nouvelle cuisine. *Speakable and Unspeakable in Quantum Mechanics: Collected Papers on Quantum Philosophy*. Cambridge University Press (2004), 232–248.

[18] B. Hensen *et al.* Loophole-free bell inequality violation using electron spins separated by 1.3 kilometres. *Nature* **526**, 682 (2015).

[19] J. F. Clauser, M. A. Horne, A. Shimony and R. A. Holt. Proposed experiment to test local hidden-variable theories. *Physical Review Letters* **23**, 880 (1969).

[20] J. S. Bell. Bertlmann's socks and the nature of reality. *Speakable and Unspeakable in Quantum Mechanics: Collected Papers on Quantum Philosophy*. Cambridge University Press (2004), 139–158.

[21] P. H. Eberhard. Background level and counter efficiencies required for a loophole-free einstein-podolsky-rosen experiment. *Physical Review A* **47**, R747 (1993).

[22] C. Simon and W. T. M. Irvine. Robust long-distance entanglement and a loophole-free bell test with ions and photons. *Physical Review Letters* **91**, 110405 (2003).

[23] P. G. Kwiat, P. H. Eberhard, A. M. Steinberg and R. Y. Chiao. Proposal for a loophole-free bell inequality experiment. *Physical Review A* **49**, 3209 (1994).

[24] J. S. Bell. Atomic-cascade photons and quantum-mechanical nonlocality. *Speakable and Unspeakable in Quantum Mechanics: Collected Papers on Quantum Philosophy*. Cambridge University Press (2004), 105–110.

[25] P. M. Pearle. Hidden-variable example based upon data rejection. *Physical Review D* **2**, 1418 (1970).

[26] S. J. Freedman and J. F. Clauser. Experimental test of local hidden-variable theories. *Physical Review Letters* **28**, 938 (1972).

[27] A. Aspect, P. Grangier and G. Roger. *Physical Review Letters* 91–94.

[28] W. Tittel, J. Brendel, H. Zbinden and N. Gisin. Violation of bell inequalities by photons more than 10 km apart. *Physical Review Letters* **81**, 3563 (1998).

[29] G. Weihs, T. Jennewein, C. Simon, H. Weinfurter and A. Zeilinger. Violation of bell's inequality under strict einstein locality conditions. *Physical Review Letters* **81**, 5039 (1998).

[30] T. Scheidl *et al.* Violation of local realism with freedom of choice. *Proceedings of the National Academy of Sciences* **107**, 19708 (2010).

[31] M. A. Rowe *et al.* Experimental violation of a bell's inequality with efficient detection. *Nature* **409**, 791 (2001).

[32] D. N. Matsukevich, P. Maunz, D. L. Moehring, S. Olmschenk and C. Monroe. Bell inequality violation with two remote atomic qubits. *Physical Review Letters* **100**, 150404 (2008).

[33] M. Ansmann *et al.* Violation of bell's inequality in josephson phase qubits. *Nature* **461**, 504 (2009).

[34] J. Hofmann *et al.* Heralded entanglement between widely separated atoms. *Science* **337**, 72 (2012).

[35] W. Pfaff *et al.* Demonstration of entanglement-by-measurement of solid-state qubits. *Nature Physics* **9**, 29 (2013).

[36] M. Giustina *et al.* Bell violation using entangled photons without the fair-sampling assumption. *Nature* **497**, 227 (2013).

[37] B. G. Christensen *et al.* Detection-loophole-free test of quantum nonlocality, and applications. *Physical Review Letters* **111**, 130406 (2013).

[38] J. Barrett, L. Hardy and A. Kent. No signaling and quantum key distribution. *Physical Review Letters* **95**, 010503 (2005).

[39] I. Gerhardt *et al.* Experimentally faking the violation of bell's inequalities. *Physical Review Letters* **107**, 170404 (2011).

[40] A. Acín *et al.* Device-independent security of quantum cryptography against collective attacks. *Physical Review Letters* **98**, 230501 (2007).

[41] R. Colbeck. *Quantum and Relativistic Protocols for Secure Multi-Party Computation.* Ph.D. thesis, University of Cambridge (2007).

[42] S. Pironio *et al.* Random numbers certified by bell's theorem. *Nature* **464**, 1021 (2010).

[43] A. Gruber *et al.* Scanning confocal optical microscopy and magnetic resonance on single defect centers. *Science* **276**, 2012 (1997).

[44] W. B. Gao, A. Imamoglu, H. Bernien and R. Hanson. Coherent manipulation, measurement and entanglement of individual solid-state spins using optical fields. *Nature Photonics* **9**, 363 (2015).

[45] M. W. Doherty *et al.* The nitrogen-vacancy colour centre in diamond. *Physics Reports* **528**, 1 (2013).

[46] C. Kurtsiefer, S. Mayer, P. Zarda and H. Weinfurter. Stable solid-state source of single photons. *Physical Review Letters* **85**, 290 (2000).

[47] F. Jelezko *et al.* Observation of coherent oscillation of a single nuclear spin and realization of a two-qubit conditional quantum gate. *Physical Review Letters* **93**, 130501 (2004).

[48] J. R. Maze *et al.* Nanoscale magnetic sensing with an individual electronic spin in diamond. *Nature* **455**, 644 (2008).

[49] G. Balasubramanian *et al.* Nanoscale imaging magnetometry with diamond spins under ambient conditions. *Nature* **455**, 648 (2008).

[50] F. Dolde *et al.* Electric-field sensing using single diamond spins. *Nat Phys* **7**, 459 (2011).

[51] G. Kucsko *et al.* Nanometre-scale thermometry in a living cell. *Nature* **500**, 54 (2013).

[52] G. de Lange, Z. H. Wang, D. Ristè, V. V. Dobrovitski and R. Hanson. Universal dynamical decoupling of a single solid-state spin from a spin bath. *Science* **330**, 60 (2010).

[53] C. A. Ryan, J. S. Hodges and D. G. Cory. Robust decoupling techniques to extend quantum coherence in diamond. *Physical Review Letters* **105**, 200402 (2010).

[54] V. Jacques *et al.* Experimental realization of wheeler's delayed-choice gedanken experiment. *Science* **315**, 966 (2007).

[55] G. Waldherr, P. Neumann, S. F. Huelga, F. Jelezko and J. Wrachtrup. Violation of a temporal bell inequality for single spins in a diamond defect center. *Physical Review Letters* **107**, 090401 (2011).

[56] R. E. George *et al.* Opening up three quantum boxes causes classically undetectable wavefunction collapse. *Proceedings of the National Academy of Sciences* **110**, 3777 (2013).

[57] F. Jelezko, T. Gaebel, I. Popa, A. Gruber and J. Wrachtrup. Observation of coherent oscillations in a single electron spin. *Physical Review Letters* **92**, 076401 (2004).

[58] L. Childress *et al.* Coherent dynamics of coupled electron and nuclear spin qubits in diamond. *Science* **314**, 281 (2006).

[59] P. Neumann *et al.* Multipartite entanglement among single spins in diamond. *Science* **320**, 1326 (2008).

[60] P. Neumann *et al.* Single-shot readout of a single nuclear spin. *Science* **329**, 542 (2010).

[61] T. H. Taminiau, J. Cramer, T. v. d. Sar, V. V. Dobrovitski and R. Hanson. Universal control and error correction in multi-qubit spin registers in diamond. *Nature Nanotechnology* **9**, 171 (2014).

[62] L. Robledo *et al.* High-fidelity projective read-out of a solid-state spin quantum register. *Nature* **477**, 574 (2011).

[63] E. Togan *et al.* Quantum entanglement between an optical photon and a solid-state spin qubit. *Nature* **466**, 730 (2010).

[64] L. Childress, J. M. Taylor, A. S. Sørensen and M. D. Lukin. Fault-tolerant quantum communication based on solid-state photon emitters. *Physical Review Letters* **96**, 070504 (2006).

[65] H. J. Kimble. The quantum internet. *Nature* **453**, 1023 (2008).

Chapter 2

Methods

B.J. Hensen

In this chapter we will introduce nature's own trapped ion system, the Nitrogen-Vacancy (NV) defect in diamond. We will first present the basic electronic structure and the defect's spin and optical properties (Sec. 2.1). In Sec. 2.2 and 2.3 we will highlight the most important experimental aspects of NV centre control. The toolbox to initialize, control and read out the NV-spin register quantum state will be introduced in Sec. 2.4, where we also discuss the challenges to attain short and long term stability of the setup. Finally, in Sec. 2.5 we summarize the remote entanglement protocol as the main workhorse in the subsequent chapters of this thesis.

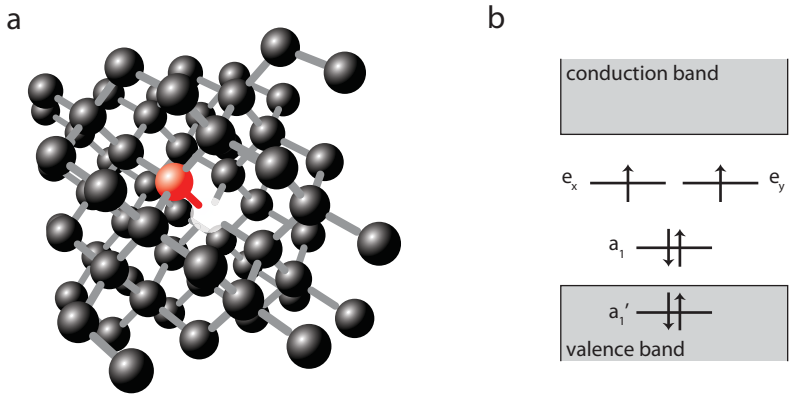

Figure 2.1 — Crystal and electronic structure of the NV centre (a) The Nitrogen-Vacancy center defect is formed by a substitutional nitrogen atom (N) and a missing atom (vacancy, V) at an adjacant position in the diamond lattice. **(b)** The electron occupation of the molecular orbitals in the electronic ground state of NV^-, following Pauli's exclusion principle.

2.1 The NV centre in diamond

2.1.1 Defect structure

The Nitrogen Vacancy centre is a point defect in the diamond crystal. It consists of a substitutional nitrogen atom and a neighbouring vacancy (Fig. 2.1a). In its neutral charge state, denoted NV^0, the 5 unbound valence electrons of the surrounding nuclei (3 from the carbons, 2 from the nitrogen), occupy a localized wave-function around the vacancy. An additional electron can be trapped from the environment, supplied by for instance nearby charge traps in the crystal, resulting in the negatively charged state NV^-. Here, we work almost exclusively with NV^-, re-initializing the charge state whenever an electron is dynamically lost to the environment.

The electronic wave-function is well approximated by a linear combination of the available atomic orbitals around the vacancy, for the largest part the hybridized sp^3 orbitals of the 3 neighboring carbons and the nitrogen, with small contributions from next-nearest neighbours (see Doherty *et al.*[1] and references therein). Many properties of the spin-orbital eigenstates and optical and vibronic transitions can be deduced from the C_{3v} symmetry of the defect[1–4]. By constructing linear combinations of the available atomic orbitals, that transform according to the C_{3v} symmetry, appropriate single particle molecular orbitals can be found, whose configuration is depicted in Fig. 2.1b. Given the six-electron occupation of the orbitals, both the ground state and first excited orbital states (promoting an electron from the a_1 orbital to one of the $e_{x,y}$ orbitals in Fig. 2.1b) have an energy well within the electronic band-gap of diamond,

resulting in the trapped-ion like properties of the electronic structure. By filling the available orbitals with six electrons and a similar symmetrization of the 6 particle wave-function, a good approximation is obtained of the eigenstates of the Hamiltonian including the nuclear, coulomb, spin-spin and spin-orbit potentials. This results in the electronic structure shown in Fig. 2.2: the orbital ground state is a spin-triplet, that couples optically to the first excited orbital doublet, spin-triplet states. A meta-stable singlet state can be populated from the excited triplet state.

2.1.2 Orbital ground state manifold and hyperfine interactions

In the orbital ground state, with $S = 1$, the $m_s = 0$ and $m_s = \pm 1$ states are separated by the zero-field splitting $D \approx 2.88$ GHz, due to spin-spin interactions, while an external magnetic field lifts the degeneracy between $m_s = +1$ and $m_s = -1$ via the Zeeman splitting (Fig. 2.2, bottom right). The effective spin Hamiltonian, neglecting second order spin-orbit interactions, is given by [5]

$$H_{GS,e} = DS_z^2 + \gamma_e \mathbf{B} \cdot \mathbf{S} \tag{2.1}$$

with $\mathbf{S} = [S_x, S_y, S_z]$, S_i the spin matrices for a spin-1 system and $\gamma_e = 2.8$ MHz/G the gyromagnetic ratio of the electron spin. We define our qubit in the $m_s = 0$ ($|0\rangle$) and $m_s = -1$ ($|1\rangle$) states (alternatively the $m_s = +1$ state can be used to encode $|1\rangle$). For the experiments in this thesis we work with a typical splitting between the $m_s = \pm 1$ states around 100 MHz.

All NV centres have an intrinsic nuclear spin associated with the nitrogen atom of the defect. The most common isotope is ^{14}N (99.3% abundance) which carries a spin $I = 1$. As the quantization axis of the nitrogen spin is aligned with the electron spin, the combined electron-nuclear spin system is described by the following Hamiltonian:

$$H_{e,N} = H_{GS,e} - QI_{N_z}^2 + \gamma_N \mathbf{B} \cdot \mathbf{I_N} - A_\parallel S_z I_{N_z} - A_\perp (S_x I_{N_x} + S_y I_{N_y}), \tag{2.2}$$

with I_{N_i} the nitrogen spin matrices, $\gamma_N = 0.3077$ kHz/G the gyromagnetic ratio of the nitrogen spin, $Q = 4.98$ MHz the quadrupole splitting and the hyperfine parameters $A_\parallel = 2.19$ MHz and $A_\perp \approx 2.1$ MHz[5]. The experiments reported in this thesis are performed at magnetic fields where the separation between electron spin levels is large compared to the energy scale of the flip-flop terms ($S_x I_{N_x}$ and $S_y I_{N_y}$). We therefore take the secular approximation and neglect these terms such that the Hamiltonian becomes

$$H_{e,N} = H_{GS,e} - QI_{N_z}^2 + \gamma_N \mathbf{B} \cdot \mathbf{I_N} - A_\parallel S_z I_{N_z}, \tag{2.3}$$

for a magnetic field aligned along the z-axis of the defect.

The parallel component of the hyperfine interaction introduces a splitting of the electron spin transitions that can be observed in a pulsed electron spin resonance measurement (Fig. 2.11 on page 32a). The three resonances correspond to the nuclear spin eigenstates labelled $m_I = +1, 0, -1$. To encode a qubit we define the logical states as $|0\rangle_N : m_I = -1$ and $|1\rangle_N : m_I = 0$.

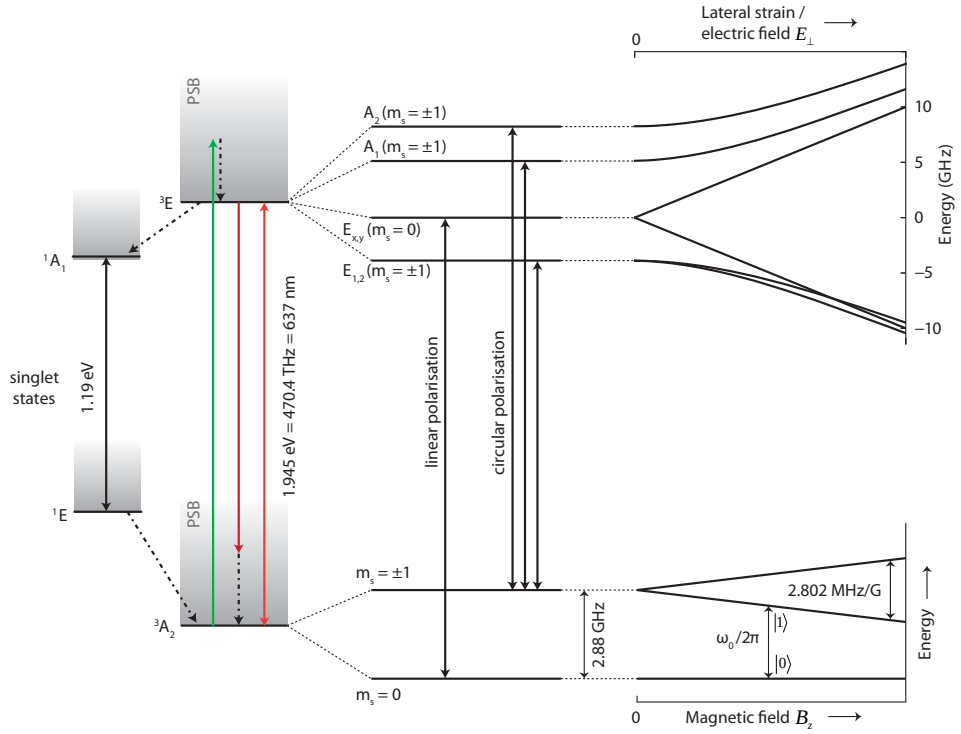

Figure 2.2 — Electronic level structure and optical excitation of NV$^-$. (Left): The ground state of the NV^- centre is the spin-triplet with orbital A_2 symmetry. It can be optically excited to one of the six excited orbital-doublet spin-triplet states, either resonantly, or off-resonantly through the phonon-sideband (PSB). Relaxation can similarly occur resonantly (into the zero-phonon-line, ZPL), into the PSB, or via the spin-singlet states. The singlet states mix with the triplet states through a spin-orbit coupling term. **(Centre)**: Spin-spin and spin-orbit interactions result in the fine structure of the ground an excited states. The ground state splits into one $m_\mathrm{s} = 0$ state and two degenerate $m_\mathrm{s} = \pm 1$ states. The excited state splits into four levels, two of which ($\mathrm{E}_{\mathrm{x,y}}$ and $\mathrm{E}_{1,2}$) are doubly degenerate. The excited state $m_\mathrm{s} = \pm 1$ levels are equal mixtures of $m_\mathrm{s} = +1$ and $m_\mathrm{s} = -1$. The $\mathrm{E}_{\mathrm{x,y}}$ states are almost completely of $m_\mathrm{s} = 0$ character, except for a small spin-spin mixing term that mix them with the $\mathrm{E}_{1,2}$ states. Optical selection rules allow spin-conserving transitions from the $m_\mathrm{s} = 0$ state to the $\mathrm{E}_{\mathrm{x,y}}$ states, with linearly polarised light, and transitions from the $m_\mathrm{s} = +1$ or $m_\mathrm{s} = -1$ ground states to the $\mathrm{E}_{1,2}$ and $\mathrm{A}_{1,2}$ states, with circularly polarized light. **(Top right)**: To first order, crystal strain affects the electronic structure in the same manner as an external electric field: the projection along the NV axis shifts the energy of the whole excited state structure, while the projection along the perpendicular axis splits the excited states as shown. The ground state is unaffected by off-axis strain to first order. **(Bottom right)**: The Zeeman splitting induced by a magnetic field along the NV axis is used to separate the degenerate $m_\mathrm{s} = \pm 1$ levels. For the work in this thesis, a qubit is defined in the $m_\mathrm{s} = 0$ and $m_\mathrm{s} = -1$ levels, with a typical magnetic field of 20-40 Gauss.

2.1.3 Transitions, rates and temperature effects

At low temperature, low strain splitting, the excited state lifetime of the $E_{x,y}$ excited states is found to be 12.1 ± 0.2 ns (see e.g. Fig. 5.10 on page 119). Due to the strong cyclic nature of the $m_s = 0 \Leftrightarrow E_{x,y}$ transitions, this lifetime is expected to be close to the bare excited state lifetime[3,6]. Relaxation through the singlet states occurs predominantly from the excited state $m_s = \pm 1$ levels[6,7]. The upper singlet level $^1A_1$ has a short lifetime of about 1 ns[8], while the lower levels ^1E relax non-radiatively to the ground state triplet with a lifetime of about 400 ns[7,8], with an expected equal contribution to the $m_s = 0$ and $m_s = \pm 1$ levels[7].

Phonons cannot couple to the electronic spin degree of freedom directly, so require spin-orbit coupling to cause a spin-flipping mechanism[4]. Below 4 kelvin, the dominant role of phonons and local vibronic modes regarding the NV centre's spin dynamics is to assist in the non-radiative decay to and from the singlet states[9–11]. From 4 – 30 kelvin, at low strain, a two-phonon process mixes excited triplet states with the same spin projection, with a strong T^4 temperature dependence[6,9]. At higher temperatures, the excited state orbital doublet ^3E interacts with the lattice vibrations much stronger, and at room temperature the individual excited states are no longer resonantly addressable[10]. At low temperature, emission into the ZPL accounts for about 4% of the emission, at room temperature the relative phonon-sideband contribution is increased (panel c of Fig. 2.5 on page 26 shows a typical room-temperature spectrum).

2.1.4 The neutral charge state

The NV centre can dynamically switch between the NV^0 and NV^- charge states, through a two-photon absorption process[12,13]. Much less is known about the electronic structure of the neutrally charged NV^0. It possess a 575 nm zero-phonon line transition, but the exact electronic orbital structure of NV^0 is still debated[14]. In this thesis the NV^0 optical transitions are used to re-initialize the NV^- charge state[12,13]. In order to gain some understanding of the NV^0 optical transitions, we perform photoluminescence excitation spectra of both charge states of a single NV. We compare the spectra obtained from NV^- (which allows extraction of the strain/electric field components experienced by the NV^-) to the ones obtained from NV^0.

In Fig. 2.3, spectra are taken of a single NV as a function of externally applied electric field. Electric field is applied through a voltage applied to the surface gate electrodes (see Fig. 2.6 on page 27). Fig. 2.4 shows a quantitative analysis of the observed transition frequencies from this measurement, as well as measurements performed without external gate voltages on various other NV's.

The data in Fig. 2.4b is consistent with a nonzero splitting of about 9 GHz for the NV^0 optical transitions, for cases where the NV^- splitting goes to zero. This splitting would be surprising for the proposed[14] model of a single excited state coupled to two ground states for NV^0, as the absence of an off-axis electric-field component for NV^-

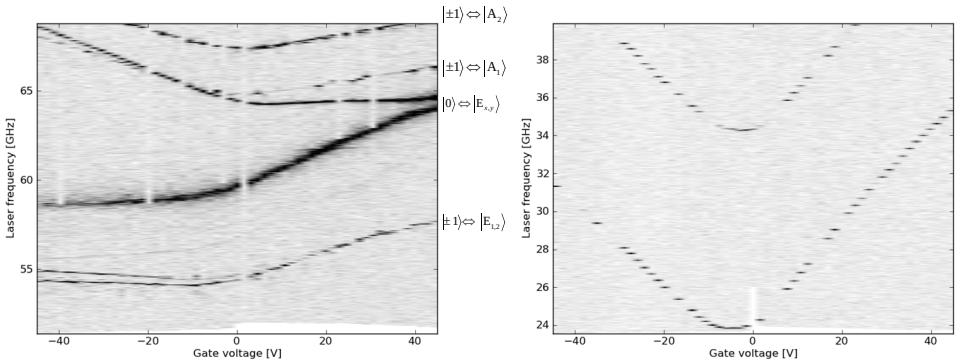

Figure 2.3 — Photo-luminescence excitation spectra of NV^- and NV^0 as a function of d.c. Stark tuning gate voltage. For each step in gate voltage the following procedure is followed: **(a)** the NV^- is laser frequency is scanned first, at low power (5 nW, approximately saturation power). A continuous microwave tone at the $m_s = 0 \leftrightarrow m_s = -1$ transition is applied during the scan. NV^- is then ionised to NV^0 by doing the same scan in reverse with high power red (30 nW, data not shown). **(b)** Then the NV^0 spectrum is recorded, with an excitation power of 0.5 nW. Finally, NV^0 is similarly de-ionised to NV^-, by the same scan in reverse (50 nW, data not shown). Laser frequencies shown are with respect to 470.4 THz (a) and 521.22 THz (b).

(corresponding to zero splitting) is expected to translate to the NV^0 case (as it has the same symmetry axis)[14]. We note however that the electric field at the location of the NV might be different for NV^0 and NV^-. Firstly, for the data presented in Fig. 2.3, it is known that for constant gate voltage the electric field at the NV drifts over time, likely due to (surface) charge trap population dynamics and screening effects. Although the laser excitation spectra are recorded subsequently for NV^0 and NV^-, they cannot be taken simultaneously. Secondly, the ionized electron from NV^- might be trapped in the vicinity of the NV, thus causing a different electric field.

The clear difference in slope in Fig. 2.4a between the data obtained for different NV's without gate tuning, and those obtained by electric field tuning, could indicate a different relative NV^-/NV^0 sensitivity for electric field compared to crystal strain.

Given an initial NV^- strain splitting, one NV^- $E_{x/y}$ and one NV^0 transition frequency, the slope obtained from gate-voltage scans like in Fig. 2.3 can be used to recalculate the strain splitting of NV^-, for changed NV^- and NV^0 frequencies. This is used for the automated laser frequency tuning described in Sec. 2.4.6.

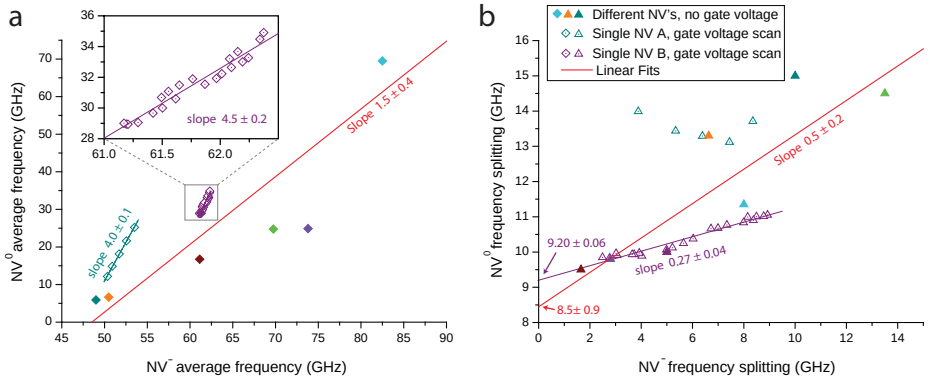

Figure 2.4 — Relation of the NV^- optical frequencies to NV^0. Solid datapoints are obtained from photo-luminescence excitation spectra without any external gate voltage applied, for 9 different NV's in 4 different diamond samples. Purple open data points of NV A, including the inset, are obtained from the measurement presented in Fig. 2.3. Turquoise open datapoints are obtained by an identical measurement procedure on another NV. **(a)** Shown are the average transition frequencies of NV^- versus NV^0. For NV^-, we take the average of the E_x and E_y related transitions, for NV^0 the average of the two observed transitions. Frequencies are with respect to 470.4 THz (NV^-) and 521.22 THz (NV^0). **(b)** shows instead the splitting between the mentioned transitions. Red solid lines are linear fits to the solid datapoints, with indicated 1 SE fit errors.

2.2 Device fabrication

Fig. 2.5a shows the typical measurement configuration to detect single NV centres. By scanning the position of the sample with respect to a confocal microscope setup, we observe single spots of fluorescence (Fig. 2.5b). Identification as a single NV can be done by checking its emission spectrum (Fig. 2.5c) using a spectrometer, anti-bunching of its emission (Fig. 2.5d), and by optically detected electron spin resonance (Fig. 2.10 on page 31).

The experiments in this thesis are all performed on individual NV centres that are naturally present in high purity type IIa chemical-vapor deposition diamond samples grown by Element Six Innovation, with a $\langle 111 \rangle$ crystal orientation. When a new diamond sample is obtained, it goes through a number of fabrication steps:

First, a gold strip-line and marker field for navigation is fabricated on the surface by electron-beam lithography. About 10-30 single NVs are searched for, in the setup described in Fig. 2.5. These NV's are preselected to have a 111 orientation by checking excitation polarisation dependence. Additionally, for the work in this thesis, NV's with a strongly (> 1 MHz coupling) coupled ^{13}C (1% natural abundance) are unwanted, and are excluded in this step by checking the optically detected electron spin resonance

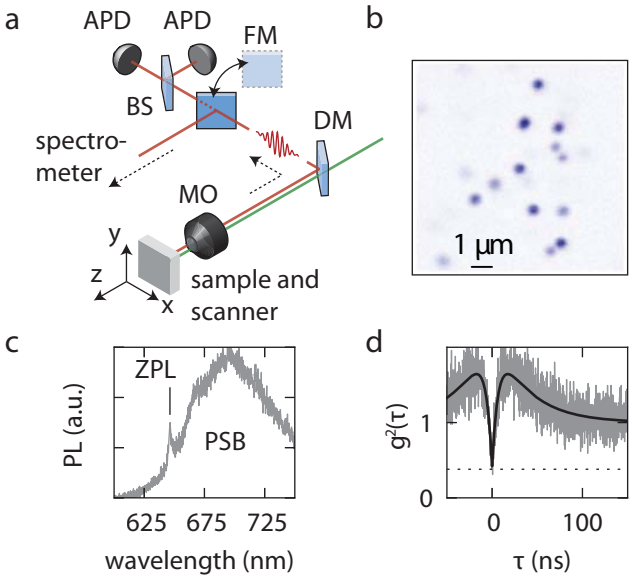

Figure 2.5 — Detection of single NV centres Figure from Bernien[15]. **(a)** Confocal microscope setup. The NV centres are excited by focussing a green (532 nm) excitation laser onto the sample using a microscope objective (MO). The sample is mounted on a piezo-stage allowing three-dimensional scans. The emission is spectrally filtered using a dicroic mirror (DM) and via a mechanically switchable mirror (FM) sent either to a spectrometer or to a beamsplitter (BS) followed by two APDs in a HBT-configuration. **(b)** Confocal scan of a bulk diamond sample. The intensity is plotted as a function of the stage position in x and y. Blue is higher intensity. **(c)** Emission spectrum of a single NV centre with the zero phonon line at 637 nm and the phonon-sideband at higher wavelengths. **(d)** Second-order autocorrelation function, with τ the delay between detection events of different detectors. The solid-line is a fit using a three-level model, including dark counts. The slow decay is associated with the decay from the singlet levels.

spectrum.

Next, a hemispherical Solid Immersion Lens (SIL) is fabricated around the NV locations found in the previous step. The SILs are fabricated by milling away diamond in a focussed ion beam. The hemispherical domes allow efficient extraction of the NV's fluorescence out of the high index of refraction diamond material, by minimizing total internal reflection[15,16]: ideally the NV sits at the centre of the hemisphere, resulting in light exiting the diamond perpendicular to the surface for the entire collection numerical aperture. The collection efficiency from each of these structures is characterized by a count-rate saturation measurement, and the best 5-10 are selected for further fabrication. Fig. 2.6 shows the typical surface structure of a finished device and the effect of the SIL.

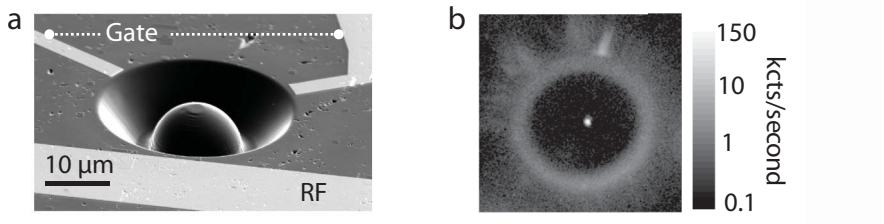

Figure 2.6 — Figure from Bernien[15]. **(a)** Electron microscope image of a device. A solid immersion lens (SIL) is fabricated into the diamond surface (grey) by ion beam milling. Below the SIL a gold strip line (light grey, RF) is fabricated for magnetic resonance pulses. A DC voltage can be applied to the gold gate-electrodes on the top, d.c. Stark tuning. **(b)** Confocal scan of the SIL with green excitation and detection in the PSB. The enhanced emission of the NV centre is visible in the middle.

In a final electron beam lithography step, a gold strip is fabricated across the surface of the diamond, through which we can apply the AC current to drive electron/nuclear spin oscillations (Sec. 2.4.3). Gold gate-electrodes to apply static electric fields are also fabricated, allowing tuning of the NV's optical resonances through the d.c. Stark effect[17].

For the samples used in Chapter 4 and 5, a single layer anti-reflection coating (aluminium oxide) is additionally fabricated as a top layer to further reduce unwanted reflections.

2.3 Experimental control setup

Fig. 2.7 shows a schematic representation of the typical hardware setup used for a single setup. The experimental protocols discussed in this thesis involve conditional logic, for instance for probabilistic charge and resonance preparation, probabilistic preparation of nuclear spin states by projective measurement, and feedback in the teleportation protocol. We therefore implement the experiment control loops on a fast, programmable controller with DAC- and counter-modules (*ADwin Gold II* or *ADwin Pro*) that is able to trigger experiment sequences on other hardware.

2.4 Initialization, control and readout

The electronic spin can be initialised and read out optically using the standard tools from atomic physics. In this thesis, we use optical light fields at two different frequencies for this: a readout (RO) laser, that excites one of the two $m_s = 0 \Leftrightarrow E_{x,y}$ transitions, and a spin-pumping (SP) laser that excites both $m_s = \pm 1$ ground states

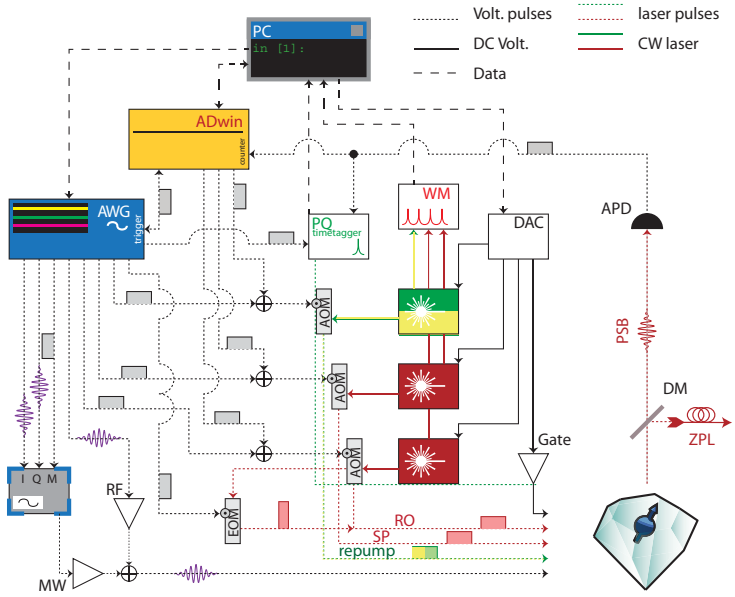

Figure 2.7 — Figure adapted from Pfaff[18]. **Typical measurement control setup schematic.** A PC programs the control loop on a integrated micro-controller (*ADwin*) and pulse sequences on an arbitrary waveform generator (AWG; *Tektronix AWG 5014*). Sequences on the AWG are triggered from the ADwin, and the AWG notifies the ADwin when sequences are completed. Both ADwin and AWG generate laser pulses for charge re-pumping (repump), electron spin pumping (SP), and electron spin readout (RO) via acousto-optical modulators. The AWG also generates fast optical excitation pulses for coherent optical control on the readout transition via an electro-optical modulator. Laser frequencies are monitored with a wave meter (*Highfinesse WS6* or *WSU*), and controlled using DAC modules on the frequency modulation inputs of the lasers. Microwave pulses are generated by a vector source (*Rohde & Schwarz SMB100A*). The AWG controls frequency and timing of these pulses via IQ- and pulse modulation. RF pulses are synthesised directly in the AWG. Spin manipulation signals are amplified (*Amplifier Research 20S1G4* or *40S1G4* for MW, and *AR 30W 1000B* or *Electronic & Innovation 240L* for RF) and combined (*Minicircuits*) before feeding to the sample. Gate voltages to the sample are controlled via a home-built DAC module and DC amplifier. Phonon-sideband (PSB) fluorescence is split off from the zero-phonon line (ZPL) emission using a dichroic mirror (DM) and detected with an avalanche photodiode (APD). Detection events are registered by both the counting module of the ADwin and a fast time-tagging module (PicoQuant; *TimeHarp 260N* or *HydraHarp 400*).

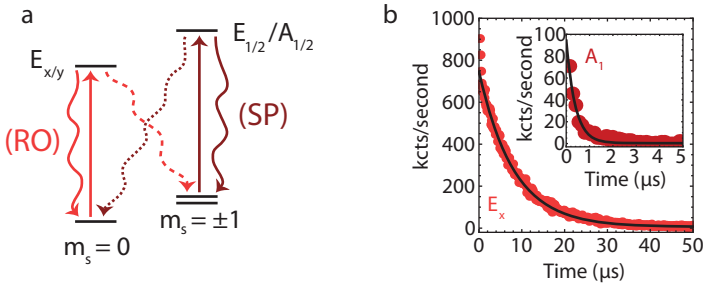

Figure 2.8 — Figure adapted from Robledo *et al.*[19] **Initialization by spin pumping. (a)** Optical transitions used to initialize (and readout) the electron spin. We excite transitions with a well-defined spin character of either $m_s = 0$ (bright red arrows) or $m_s = \pm 1$ (dark red arrows), resulting in spin-conserving optical cycling (indicated by bended solid arrows). Dashed arrows indicate the spin non-conserving decay paths. **(b)** Observed fluorescence when exciting to the E_x (A_1) states with the spin initially prepared in $m_s = \pm 1$ ($m_s = 0$). From the exponential fit we find a lower limit for the initialization fidelities: $(99.7 \pm 0.1)\%$ for $m_s = 0$ and $(99.2 \pm 0.1)\%$ for $m_s = \pm 1$.

to one of the excited states with $m_s = \pm 1$ character*, see Fig. 2.8a.

Spin rotations are performed using pulsed electron and nuclear resonance techniques, by supplying AC current though a gold stripline on the surface of the diamond.

2.4.1 Electron spin initialisation

Spin initialisation is done by simply turning on the SP-laser: if the system starts in either of the $m_s = -1$ or $m_s = +1$ states, it will be optically excited, until probabilistically a spin-flip occurs to the $m_s = 0$ ground state. As the SP-laser is not resonant with any $m_s = 0$ transition, the system will get stuck in this state. Fig. 2.8b shows an example fluorescence curve for this process, from which we can estimate an initialisation fidelity. Initialisation into either $m_s = +1$, or $m_s = -1$ is best attained by a microwave spin rotation from an initialized $m_s = 0$ state, however a mixture of $m_s = \pm 1$ can be achieved by spin-pumping with the RO-laser on the $m_s = 0$ transition until it goes dark (Fig. 2.8b).

*For small magnetic fields, the excited state line-width is broad enough such that both transitions from $m_s = -1$ and $m_s = +1$ ground states to a single excited state can be excited with one laser frequency. At higher magnetic fields, the $E_{1,2}$ states split with the same magnetic field-factor as the $m_s = \pm 1$ ground states, thus allowing a resonance condition with one frequency.

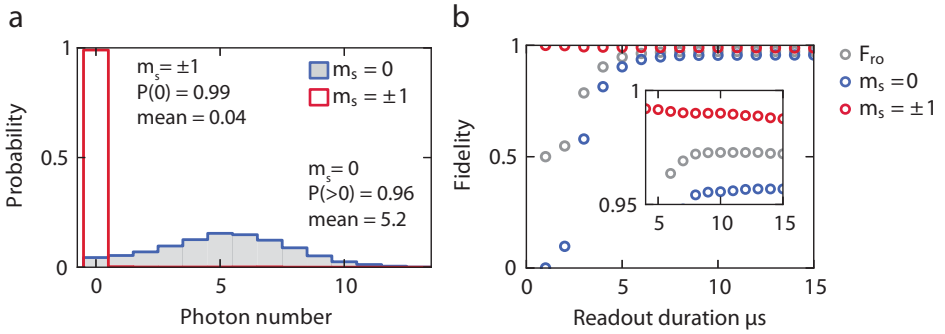

Figure 2.9 — Figure from Blok[20]. **Single shot readout. (a)** Histograms of the number of detected photons in the PSB for initial state $m_s = 0$ (blue) and $m_s = \pm 1$ (red) during a 10 μs readout on the $m_s = 0 \Leftrightarrow E_x$ transition, for a strain splitting of 1.9 GHz. **(b)** Fidelities for reading out the electron spin state initially prepared in $m_s = 0$ (blue) and $m_s = \pm 1$ (red) as a function of readout duration. The mean readout fidelity is plotted in grey. The inset is a zoom of the region where the optimal mean readout fidelity is reached.

2.4.2 Electron spin readout

Electron spin readout is obtained by collecting photons emitted into the phonon-sideband, while exciting the cycling $m_s = 0 \Leftrightarrow E_{x,y}$ transitions. Detection of 1 or more photons then indicates the spin state was in the bright $m_s = 0$ state, while if the system remains dark, we conclude it was not in the $m_s = 0$ state. For a protocol where we only populate the $m_s = 0$ and $m_s = -1$ states, this is sufficient to read out the state of the spin-qubit. Fig 2.9a shows the distribution of photon detections for an initialized spin state. The readout fidelity for the $m_s = 0$ state is limited by the finite collection efficiency and the (small $< 1\%$) spin-flip probability per optical cycle, that depends on the NV strain splitting[19]. The readout fidelity for the $m_s = \pm 1$ states is limited by detector dark counts and off-resonant excitation of one of the $m_s = \pm 1$ transitions. Fig. 2.9b shows the readout fidelities obtained for a low-strain-split NV embedded in a SIL structure (see Sec. 2.2).

2.4.3 Spin control

The electron spin in the ground state can be manipulated with electron spin resonance techniques. We send an AC current to the stripline on the diamond surface, generating an oscillating magnetic field at the location of the NV centre. When the resonance condition is met between the $m_s = 0$ and $m_s = -1$ ground states, we can drive coherent Rabi- oscillations as shown in Fig. 2.10. Arbitrary rotations can be obtained by adjusting the length or amplitude of a microwave-pulse. The hyperfine interaction causes a different electron spin resonance frequency depending on the nitrogen nuclear spin state, as shown in Fig. 2.11a. This allows for rotation of the

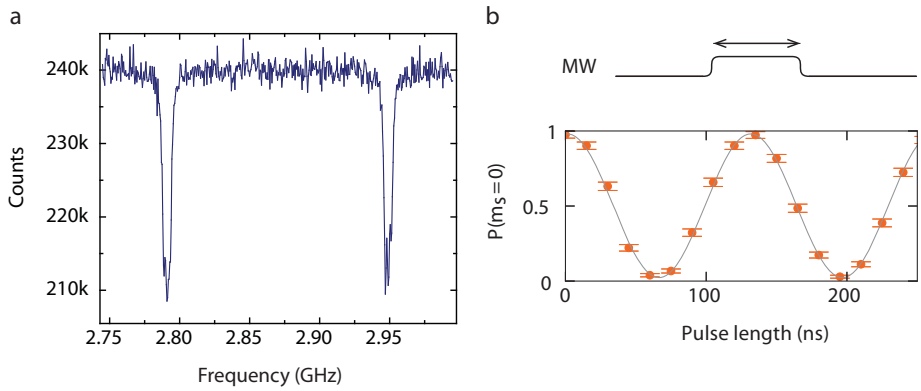

Figure 2.10 — Figure adapted from De Lange, Blok[20,21]. **Electron spin manipulation. (a)** Optically detected continuous wave (CW) electron spin resonance measurement. Integrated counts obtained from CW green excitation, for varying CW microwave frequency. The two observed dips correspond to the $m_s = 0$ to $m_s = -1$ transition (left) and $m_s = 0$ to $m_s = +1$ transition (right), for a typical axial magnetic field of 29 Gauss. **(b)** Coherent qubit rotations of the electron spin are performed by varying the length of a MW pulse resonant with the $m_s = 0$ to $m_s = -1$ transition. Solid line is a sinusoidal fit from which we determine a Rabi frequency of (7.67 ± 0.02) MHz.

electron spin conditional on the state of the nitrogen spin, by driving the electron spin sufficiently weakly such that only one of the three lines is addressed. Conversely, for an unconditional rotation of the electron spin, the Rabi frequency must be large enough to rotate all three lines.

When the electron spin is in either $m_s = \pm 1$, the nitrogen nuclear spin qubit can be manipulated via magnetic resonance techniques, similar to the electron spin, see Fig 2.11b. Here, there are two transitions with energy spitting $Q + A_\parallel$ and $Q - A_\parallel$ for the $m_I = 0 \Leftrightarrow m_I = -1$ and $m_I = 0 \Leftrightarrow m_I = +1$ respectively. An unconditional rotation of the nitrogen spin can be obtained by embedding the nuclear rotation in a electron spin echo sequence[22].

The time-scale of the manipulation scales inversely with the gyromagnetic ratios, resulting in a typical Rabi frequency of 1-10 MHz for the electron spin rotations, and a Rabi frequency 5-20 kHz for the nitrogen spin rotation.

2.4.4 Nuclear spin initialisation and readout

By combining rotations of the electron spin conditional on the state of the nuclear spin (Fig. 2.11a) with electron spin readout, we can read out the state of the nuclear spin via the electron spin. If the electron readout is non-destructive of the nuclear

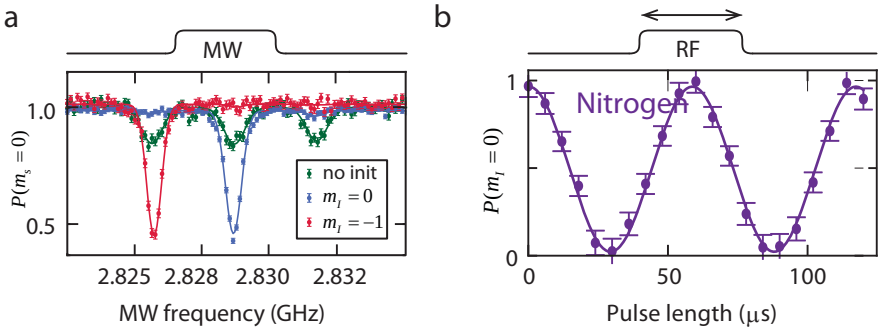

Figure 2.11 — Figure adapted from Blok[20]. **Manipulation of the nitrogen spin. (a)** Pulsed electron spin resonance measurement of the electron spin $m_s = 0$ to $m_s = -1$ transition. The three resonances (grey) arise from the hyperfine interaction with the uninitialised nitrogen spin. By driving the electron sufficiently weakly on one of the three resonance lines ($m_I = 0, -1$ blue,red respectively), the electron spin is rotated conditional on the nitrogen spin state. When followed by a projective measurement of the electron spin, the nuclear spin can be read out or initialised by measurement. **(b)** Coherent qubit rotations of the nitrogen spin are performed by varying the length of an RF pulse at 7.1 MHz. Solid line is a sinusoidal fit from which we determine the Rabi frequency (17.07 ± 0.01) kHz.

spin state populations, this can be done repetitively, which yields a higher readout fidelity.

To initialize the nuclear spin state, one can swap an initialized electron spin state to the nitrogen spin state, or, as we do in this thesis, initialize the nuclear spin by measurement. We use the antisymmetric nature of the electron spin readout, where if we detect a photon, the electron spin state is projected in the $m_s = 0$ state with very high fidelity. Combining this with a weak, selective rotation of the electron from the $m_s = -1$ state conditional on the nuclear spin state, we can in turn probabilistically initialize the nuclear spin with high fidelity (Fig. 2.11a).

2.4.5 Charge state initialization and spectral diffusion

The NV centre can dynamically switch between the NV^0 and NV^- charge states, through a two-photon absorption process[12,13]. In this thesis we are only interested in the NV^- charge state due to its ground state spin properties and consider the NV^0 state undesirable. Additionally, the NV centre optical transition frequencies fluctuate on various time-scales due to changes in the effective strain/electric field that influence the excited state energy levels. Such fluctuations can arise from (de-)population of charge traps in the vicinity of the NV centre or on the diamond surface, or drifting of the d.c. Stark tuning voltage applied to the surface electrodes. Fluctuations on a short time-scale ($<\approx 1$ ms) effectively broaden observed transition linewidths (usually

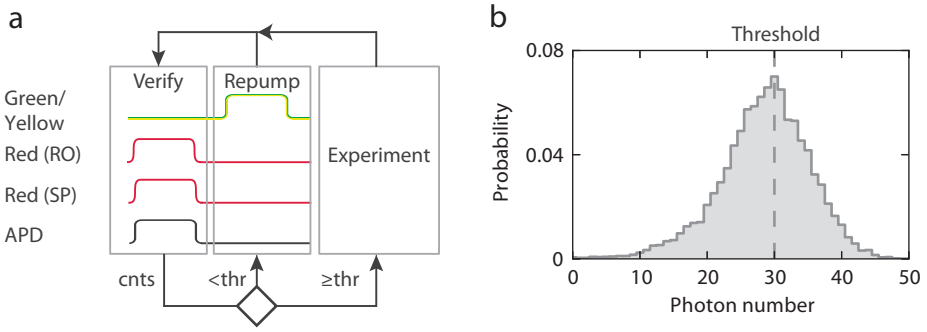

Figure 2.12 — Verifying the charge state and laser resonances. **(a)** Schematic of the experimental sequence to verify the charge state of the NV centre and the laser resonances, as used in Chapters 3 and 4. The $m_s = 0$ and $m_s = \pm 1$ ground states are simultaneously excited, using the RO and SP lasers, while an Avalanche Photo-diode (APD) counts photons emitted into the PSB. Only when the number of detected counts in a fixed integration time is exceeded do we proceed to do the experiment. When the number of detected photons is below the threshold a green laser is applied to prepare the NV^- state (repump stage), otherwise the experimental sequence is initiated. **(b)** Photon number distribution during the verification stage, conditioned on the previous CR check being successful.

referred to as spectral diffusion).

We mitigate both the broadening and charge state effects by using a charge and resonance (CR) check[19,23] (Fig. 2.12): we simultaneously excite with the RO-laser ($m_s = 0$ transition) and SP-laser ($m_s = \pm 1$ transition). The lasers have a linewidth much narrower than the life-time limited linewidth of the NV transitions, and powers are chosen below saturation power. By only starting an experimental run when the number of photons detected in a short (≈ 50 μs) excitation period exceeds a fixed threshold value, we can reduce the effective NV^- transition linewidth to its life-time limited value (see panel b of Fig. 3.3 on page 48). Additionally, when little or no detections occur, we assume the NV to be ionized to NV^0. We then apply a charge repump pulse to re-initialize the NV^- charge state by exciting the NV^0 optical transition[24].

The charge repump can be done either off-resonantly using a strong (≈ 10 μW, as opposed to typical resonant saturation powers of a few nW), short (10 μs) 532 nm laser pulse, or resonantly using a much weaker ($\approx$ saturation power), longer (500 μs) 575 nm laser pulse. A disadvantage of using the off-resonant green repump pulse lies in its effect on the NV centre's charge environment. Depending on the presence of nearby charge traps, using a strong repump can result in environmental charge dynamics on various time-scales, affecting the NV centre's optical transition stability and causing additional spectral diffusion, as seen in Fig. 2.13.

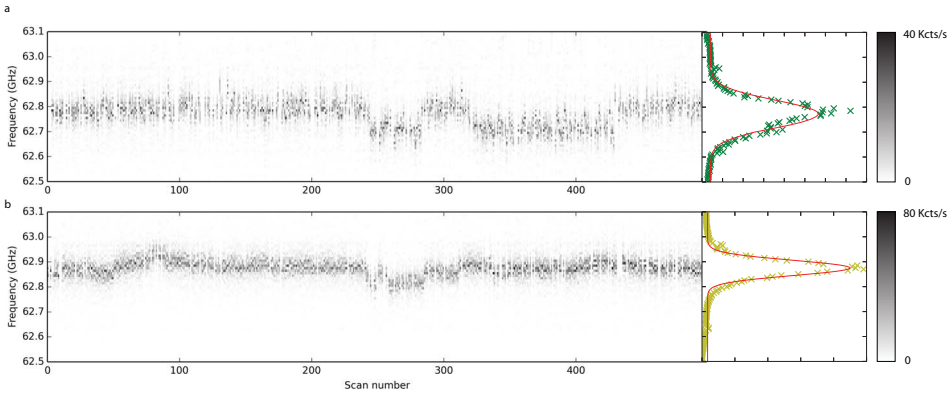

Figure 2.13 — Spectral diffusion effects for resonant and non-resonant charge repumping. Shown are 500 subsequent photo-luminescence excitation spectra of the $m_s = 0 \Leftrightarrow E_x$ of NV^-, with a Gaussian fit to the averaged spectrum to the right. In **(a)**, between each scan a strong non-resonant repump pulse was applied (532 nm, 150 μW, 0.5 s). The fit yields a linewidth of (130 ± 4) MHz FWHM. In **(b)**, between each scan a resonant repump was applied by sweeping over the NV^0 resonance (575 nm, 300 MHz sweep over resonance during 2 s, 50 nW). The fit yields a linewidth of 71 ± 1 MHz FWHM. For the non-resonant case (a), in 25 % of the scans no resonance was observed, for the resonant case (b), 12 %.

Additionally, it is found that the d.c. electric field used for Stark tuning the NV's optical frequency, applied using the surface gate electrodes, is altered by strong optical illumination. The electric field strength along the optical illumination axis can be enhanced initially, but on the order of seconds, the electric field at the location of the NV becomes effectively screened. It is speculated that the strong optical illumination allows nearby charge traps to redistribute their charges according to the applied electric field. In chapter 3, this effect is mitigated by reversing the d.c.-voltage on a 20 millisecond time-scale. On this time-scale the charges might not have enough time to redistribute fully, so that by only running the experiment in one of the two electric field "phases", we can still use sufficient Stark tuning over long time-scales (however reducing the start-rate by a factor two).

If no d.c.-Stark tuning is required, the two repump methods can also be compared on their efficiency of passing the CR-check. The resonant yellow repump pulse can (in principle) deterministically initialize the charge state, whereas for the non-resonant case the NV centre only ends up in the NV^- state in about 70% of the cases (again depending on its environment). However, the non-resonant pulse is much shorter, such that including the charge check duration, it still initializes the charge state much faster. Nonetheless, the spectral diffusion will cause the resonance check to fail more often, resulting in a lower CR success rate. Finally, the use of the resonant repump method

requires additional laser frequency stabilisation as described in Sec. 2.4.6 below: not only the repump laser itself has to be kept on resonance now, but the absence of the increased spectral diffusion due to the off-resonant repumping actually requires much more precise tuning of the two red lasers, to efficiently pass the CR-check.

Finally, for longer, millisecond-length pulse sequences, the time since the last CR-check increases. In that case charge dynamics on a millisecond time-scale could affect the fidelity of the performed NV operations. This effect is expected to be enhanced for the high power off-resonant repump.

2.4.6 Laser stabilization and feedback

Although the CR-check described in the precious section effectively removes spectral diffusion, slower, second time-scale drifts occur, of either the NV transition frequencies or the reference to which the lasers are locked (typically a wave-meter). These drifts exceed the typical spectral diffusion, and can therefore reduce the CR check success rate, the experimental start-rate and the conditional probability of actually being on resonance after the CR check passes.

For the experiments in Chapters 3 and 4, these drifts were compensated 'by hand': looking at the average number of counts during the CR check, the frequencies of the excitation lasers and/or the applied gate voltage would be adjusted every few seconds to minutes. Although sufficient, this solution is very labour-intensive and potentially error-prone, considering the typical rates of the experiments involved (one event every 10 minutes to one event every hour for the experiment in Chapter 5), and the typical hours of experimental operation (day and night).

Feedback control was implemented to automatically counteract the slow drifts. In the typical two-setup entanglement scenario, we use the RO-laser as the common reference for both NV's. The d.c. Stark gate voltage is adapted to match the resonance condition for the chosen $m_s = 0$ transition. The SP-laser and yellow repump-laser (for resonant repumping) frequencies must then be changed accordingly. To obtain an error-signal for the feedback control of the gate voltage, the pre-experiment stage was altered as shown in Fig. 2.14a. By superimposing a small (≈ 0.1 V) fast (50 μs) modulation on the static gate voltage, we can correlate the amount of counts obtained during resonant illumination with the phase of this modulation. By averaging over about 5 seconds, an error-signal could be obtained to adjust the static gate voltage, using a standard PID-feedback loop. In this manner we can 'lock' the NV to a fixed laser frequency. A similar method was used to lock the yellow repump-laser to the NV resonance. In this case the driving frequency of the acousto-optical modulator (used for amplitude-modulation) the laser was frequency-modulated as well.

Finally, to adapt the SP-laser frequency accordingly, the change of the yellow repump-laser frequency and the fixed RO-laser frequency was used to calculate the change in parallel and perpendicular components of the effective electric field (see

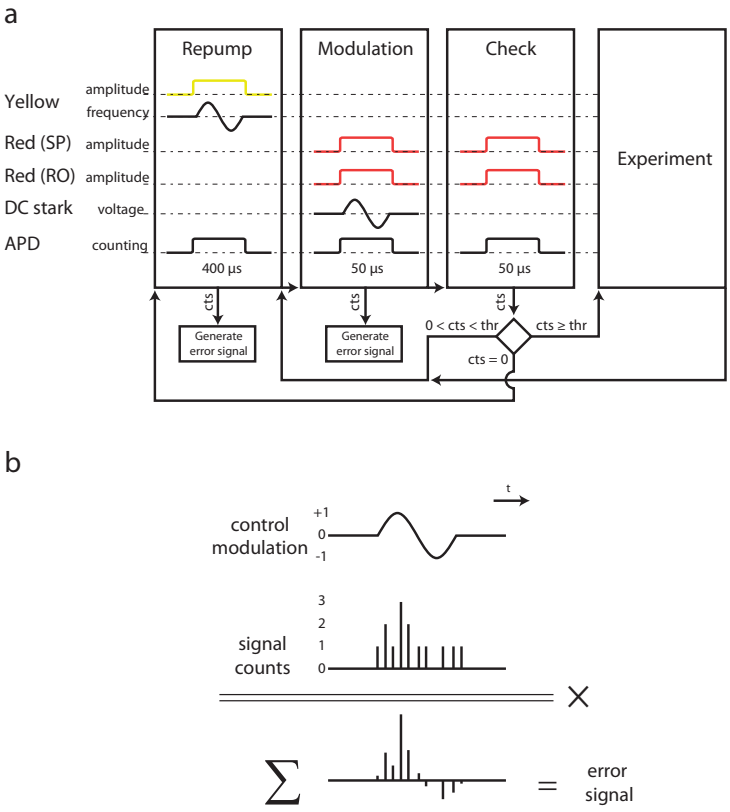

Figure 2.14 — Stabilising d.c.-Stark voltage and laser frequencies by feedback control (a) Extended version of the CR check shown in Fig. 2.12: During the resonant NV^0 repump phase (1st block), the yellow laser frequency is modulated and correlated with the emission countrate, to obtain an error signal for laser frequency stabilisation. Similarly, the gate-electrode voltage is modulated on top of its static offset voltage, to obtain an error signal (2nd block). After this we proceed with the standard CR check as described in Sec. 2.4.5. **(b)** Method used to obtain an error signal: the modulated signal is correlated with the arrival time of photon detections in the PSB.

Sec. 2.1.4), from which in turn we can calculate the expected frequency of the chosen $m_s = \pm 1$ transition.

2.5 Remote entanglement generation

To generate an entangled state between the electronic spin states of two NV centres in different diamond samples, we use photons as the mediating qubits, with a method known as entanglement swapping[25–29]. First, the electron spin state of each NV is entangled with a single photon, emitted by the NV's. Different protocols allow entanglement with various degrees of freedom of the photonic state, such as polarisation, wavelength, spatial or temporal mode. Next, the photons are overlapped on a non-polarizing beamsplitter. The detection of two photons in the same (different) output port(s) of the beam-splitter projects the spins on a symmetric (anti-symmetric) joint state, which in general can be maximally entangled. Such a process is probabilistic, but the heralding allows in principle unit fidelity overlap with the target state. The heralding also makes the process insensitive to photon loss, until the photon detection probability from either side drops to the level of the dark count probability.

2.5.1 Barret and Kok scheme

The particular protocol for entanglement swapping used in Chapters 3, 4 and 5 was developed by Barret and Kok[30]. It relies on photonic time-bin encoding for the spin-photon entanglement, and requires a single optically excited state, with a spin-selective cycling transition to one of the ground states. The protocol proceeds as follows:

1. Both NV's, labelled A and B, are prepared in an equal superposition of the ground state spin-qubit:

$$\frac{1}{\sqrt{2}}(|\uparrow\rangle_A + |\downarrow\rangle_A) \otimes \frac{1}{\sqrt{2}}(|\uparrow\rangle_B + |\downarrow\rangle_B), \tag{2.4}$$

   where $|\uparrow\rangle, |\downarrow\rangle$ corresponds to the $m_s = 0$ and $m_s = -1$ ground states, respectively.

2. A single spin-selective optical excitation pulse, affecting only one of the two ground state spin levels, say $|\uparrow\rangle$, followed by a resonant photon emission, entangles the spin state of each NV with the presence of a photon. For A:

$$\frac{1}{\sqrt{2}}(|\uparrow\rangle_A |1\rangle_A + |\downarrow\rangle_A |0\rangle_A), \tag{2.5}$$

   and similar for B, where $|0\rangle$ denotes the vacuum mode of the electromagnetic field, and $|1\rangle$ a single photon Fock state.

3. Both NV's ground state spin is flipped using a coherent spin-inversion (microwave-π-pulse):

$$\frac{1}{\sqrt{2}}(|\downarrow\rangle_A |1\rangle_A + |\uparrow\rangle_A |0\rangle_A), \tag{2.6}$$

4. A second identical excitation pulse and photon emission now entangles the spin state of each NV with the temporal mode of a photon:

$$\frac{1}{\sqrt{2}}(|\downarrow\rangle_A |L\rangle_A + |\uparrow\rangle_A |E\rangle_A), \tag{2.7}$$

   where $|E\rangle$ denotes an early single photon emitted in the first round of excitation, and $|L\rangle$ a late photon, emitted in the second round.

5. The photons from each NV are overlapped on a beam-splitter, and if the photons are otherwise indistinguishable, the detection of one early and one late photon in the output ports of the beam splitter results in the Bell state

$$\frac{1}{\sqrt{2}}(|\uparrow\rangle_A |\downarrow\rangle_B \pm |\downarrow\rangle_A |\uparrow\rangle_B) \tag{2.8}$$

   with a +-sign for two photon detections in the same output port of the beam-splitter, and the −-sing for detection in different output ports.

The protocol has a success probability of $\frac{1}{2}\eta^2$, with η the overall detection probability of a single photon from each side. It is insensitive to path length variations that fluctuate slower than the time-separation of the first and second excitation.

2.6 Bibliography

[1] M. W. Doherty, N. B. Manson, P. Delaney and L. C. L. Hollenberg. The negatively charged nitrogen-vacancy centre in diamond: the electronic solution. *New Journal of Physics* **13**, 025019 (2011).

[2] J. R. Maze *et al.* Properties of nitrogen-vacancy centers in diamond: the group theoretic approach. *New Journal of Physics* **13**, 025025 (2011).

[3] B. Hensen. *Measurement-based Quantum Computation with the Nitrogen-Vacancy centre in Diamond*. M.sc. thesis, Delft University of Technology (2011).

[4] N. Manson, L. Rogers, M. Doherty and L. Hollenberg. Optically induced spin polarisation of the nv- centre in diamond: role of electron-vibration interaction. *1011.2840* (2010).

[5] M. W. Doherty *et al.* Theory of the ground-state spin of the nv extasciicircum{−} center in diamond. *Physical Review B* **85**, 205203 (2012).

[6] M. L. Goldman *et al.* Phonon-induced population dynamics and intersystem crossing in nitrogen-vacancy centers. *Physical Review Letters* **114**, 145502 (2015).

[7] L. Robledo, H. Bernien, T. v. d. Sar and R. Hanson. Spin dynamics in the optical cycle of single nitrogen-vacancy centres in diamond. *New Journal of Physics* **13**, 025013 (2011).

[8] V. M. Acosta, A. Jarmola, E. Bauch and D. Budker. Optical properties of the nitrogen-vacancy singlet levels in diamond. *Physical Review B* **82**, 201202 (2010).

[9] K.-M. C. Fu *et al.* Observation of the dynamic jahn-teller effect in the excited states of nitrogen-vacancy centers in diamond. *Physical Review Letters* **103**, 256404 (2009).

[10] M. W. Doherty *et al.* The nitrogen-vacancy colour centre in diamond. *Physics Reports* **528**, 1 (2013).

[11] M. L. Goldman *et al.* State-selective intersystem crossing in nitrogen-vacancy centers. *Physical Review B* **91**, 165201 (2015).

[12] P. Siyushev, H. Pinto, A. Gali, F. Jelezko and J. Wrachtrup. Low temperature studies of charge dynamics of nitrogen-vacancy defect in diamond. *arXiv:1204.4898* (2012).

[13] N. Aslam, G. Waldherr, P. Neumann, F. Jelezko and J. Wrachtrup. Photo-induced ionization dynamics of the nitrogen vacancy defect in diamond investigated by single-shot charge state detection. *New Journal of Physics* **15**, 013064 (2013).

[14] N. B. Manson *et al.* Assignment of the nv0 575 nm zero-phonon line in diamond to a 2e-2a2 transition. *arXiv:1301.3542* (2013).

[15] H. Bernien. *Control, measurement and entanglement of remote quantum spin registers in diamond*. Ph.d. dissertation, Delft University of Technology (2014).

[16] J. P. Hadden *et al.* Strongly enhanced photon collection from diamond defect centers under microfabricated integrated solid immersion lenses. *Applied Physics Letters* **97**, 241901 (2010).

[17] P. Tamarat *et al.* Stark shift control of single optical centers in diamond. *Physical Review Letters* **97**, 083002 (2006).

[18] W. Pfaff, R. Hanson and L. P. Kouwenhoven. *Quantum measurement and entanglement of spin quantum bits in diamond*. Ph.D. thesis, Delft University of Technology, Applied Sciences: Quantum Nanoscience (2013).

[19] L. Robledo *et al.* High-fidelity projective read-out of a solid-state spin quantum register. *Nature* **477**, 574 (2011).

[20] M. Blok. *Quantum measuremnt and real-time feedback with a spin register in diamond*. Ph.d. dissertation, Delft University of Technology (2015).

[21] G. De Lange, L. P. Kouwenhoven, R. Hanson, T. D. A. S. K. I. of Nanoscience Delft and D. U. o. T. TU Delft. *Quantum control and coherence of interacting spins in diamond*. Ph.D. thesis (2012).

[22] T. van der Sar *et al.* Decoherence-protected quantum gates for a hybrid solid-state spin register. *Nature* **484**, 82 (2012).

[23] L. Robledo, H. Bernien, I. van Weperen and R. Hanson. Control and coherence of the optical transition of single nitrogen vacancy centers in diamond. *Physical Review Letters* **105**, 177403 (2010).

[24] P. Siyushev *et al.* Optically controlled switching of the charge state of a single nitrogen-vacancy center in diamond at cryogenic temperatures. *Physical Review Letters* **110**, 167402 (2013).

[25] M. Żukowski, A. Zeilinger, M. A. Horne and A. K. Ekert. Event-ready-detectors" bell experiment via entanglement swapping. *Physical Review Letters* **71**, 4287 (1993).

[26] B. B. Blinov, D. L. Moehring, L.-M. Duan and C. Monroe. Observation of entanglement between a single trapped atom and a single photon. *Nature* **428**, 153 (2004).

[27] D. L. Moehring *et al.* Entanglement of single-atom quantum bits at a distance. *Nature* **449**, 68 (2007).

[28] J. Hofmann *et al.* Heralded entanglement between widely separated atoms. *Science* **337**, 72 (2012).

[29] H. Bernien *et al.* Heralded entanglement between solid-state qubits separated by three metres. *Nature* **497**, 86 (2013).

[30] S. D. Barrett and P. Kok. Efficient high-fidelity quantum computation using matter qubits and linear optics. *Physical Review A* **71**, 060310 (2005).

Chapter 3

Heralded entanglement between solid-state qubits separated by three metres

H. Bernien, B. Hensen, W. Pfaff, G. Koolstra, M.S. Blok, L. Robledo, T.H. Taminiau, M. Markham, D.J. Twitchen, L. Childress and R. Hanson

Quantum entanglement between spatially separated objects is a unique resource for quantum information processing and communication. Entangled qubits can be used to establish private information or implement quantum logical gates[1,2]. Such capabilities are particularly useful when the entangled qubits are spatially separated[3–5], opening the opportunity to create highly connected quantum networks[6] or extend quantum cryptography to long distances[7,8]. Here we present two key experiments towards the realisation of long-distance quantum networks with solid-state quantum registers. Firstly, we have entangled two electron spin qubits in diamond that are separated by a three-metre distance. Our robust entangling protocol is based on local creation of spin-photon entanglement and a subsequent joint measurement of the photons to herald spin-spin entanglement. The resulting shared Bell-pair between the two nodes then enables the unconditional teleportation of a single nuclear spin state by combining a deterministic Bell-state measurement with real-time feed-forward. These results establish diamond spin qubits as a prime candidate for the realization of quantum networks for quantum communication and network-based quantum computing[1]

The results in this chapter have been published in *Nature* **497**, 86 (2013).

3.1 Introduction

A quantum network can be constructed by using entanglement to connect local processing nodes, each containing a register of well-controlled and long-lived qubits[6]. Solids are an attractive platform for such registers, as the use of nano-fabrication and material design may enable well-controlled and scalable qubit systems[9]. The potential impact of quantum networks on science and technology has recently spurred research efforts towards generating entangled states of distant solid-state qubits[10–16].

A prime candidate for a solid-state quantum register is the nitrogen-vacancy (NV) defect centre in diamond. The NV centre combines a long-lived electronic spin (S=1) with a robust optical interface, enabling measurement and high-fidelity control of the spin qubit[10,17–19]. Furthermore, the NV electron spin can be used to access and manipulate nearby nuclear spins[20–24], thereby forming a multi-qubit register. To use such registers in a quantum network requires a mechanism to coherently connect remote NV centres.

Here we demonstrate the generation of entanglement between NV centre spin qubits in distant setups. We achieve this by combining recently established spin initialisation and single-shot readout techniques[20] with efficient resonant optical detection and feedback-based control over the optical transitions, all in a single experiment and executed with high fidelity. These results put solid-state qubits on par with trapped atomic qubits[3–5] as highly promising candidates for implementing quantum networks.

Our experiment makes use of two NV spin qubits located in independent low-temperature setups separated by 3 metres (Fig. 3.1). We encode the qubit basis states $|\uparrow\rangle$ and $|\downarrow\rangle$ in the NV spin sub-levels $m_s = 0$ and $m_s = -1$, respectively. Each qubit can be independently read out by detecting spin-dependent fluorescence in the NV phonon side band (non-resonant detection)[20]. The qubits are individually controlled with microwave pulses applied to on-chip strip-lines[18]. Quantum states encoded in the qubits are extremely long-lived: using dynamical decoupling techniques[18] we obtain a coherence time exceeding 10 ms.

3.2 Heralded entanglement

We generate and herald entanglement between these distant qubits by detecting the resonance fluorescence of the NV centres. The specific entanglement protocol we employ is based on the proposal of S. Barrett and P. Kok[25], and is schematically drawn in figure 3.2. Both centres NV A and NV B are initially prepared in a superposition $1/\sqrt{2}(|\uparrow\rangle + |\downarrow\rangle)$. Next, each NV centre is excited by a short laser pulse that is resonant with the $|\uparrow\rangle$ to $|e\rangle$ transition, where $|e\rangle$ is an optically excited state with the same spin projection as $|\uparrow\rangle$. Spontaneous emission locally entangles the qubit and photon number, leaving each setup in the state $1/\sqrt{2}(|\uparrow 1\rangle + |\downarrow 0\rangle)$, where 1 (0) denotes the presence (absence) of an emitted photon; the joint qubit-photon state of both setups is

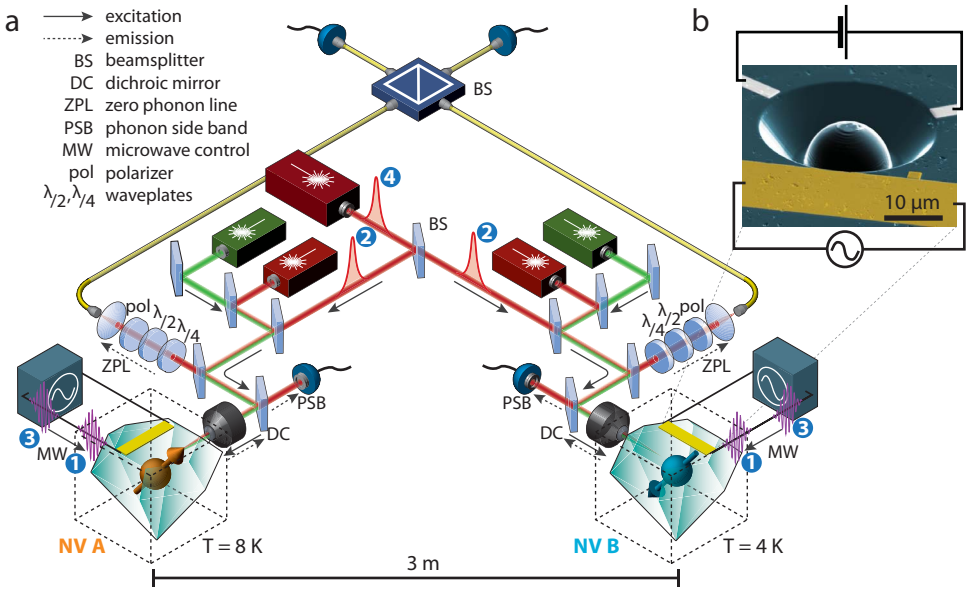

Figure 3.1 — Experimental setup. **(a)** Each nitrogen vacancy (NV) centre resides in a synthetic ultra-pure diamond oriented in the $\langle 111 \rangle$ direction. The two diamonds are located in two independent low-temperature confocal microscope setups separated by 3 metres. The NV centres can be individually excited resonantly by a red laser and off-resonantly by a green laser. The emission (dashed arrows) is spectrally separated into an off-resonant part (phonon side band, PSB) and a resonant part (zero-phonon line, ZPL). The PSB emission is used for independent single-shot readout of the spin qubits[20]. The ZPL photons from the two NV centres are overlapped on a fiber-coupled beamsplitter. Microwave pulses for spin control are applied via on-chip microwave strip-lines. An applied magnetic field of 17.5 G splits the $m_s = \pm 1$ levels in energy. The optical frequencies of NV B are tuned by a d.c. electric field applied to the gate electrodes (**(b)** scanning electron microscope image of a similar device). To enhance the collection efficiency, solid immersion lenses have been milled around the two NV centres[20].

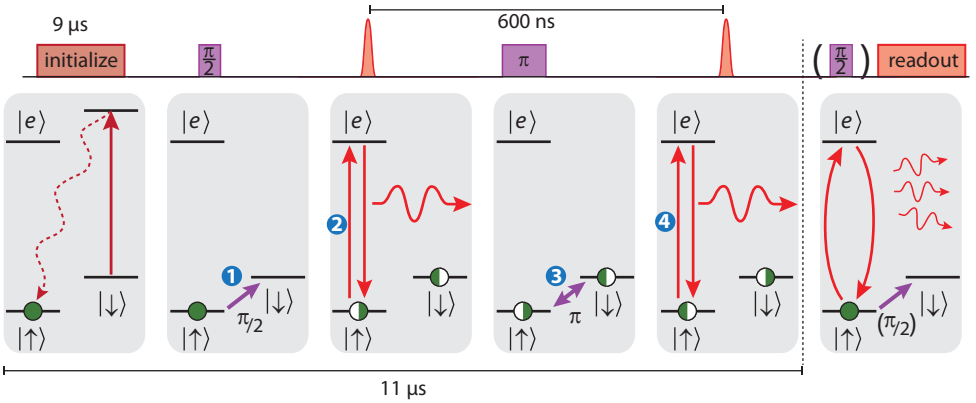

Figure 3.2 — Entanglement protocol (details in main text), illustrating the pulse sequence applied simultaneously to both NV centres. Both NV centres are initially prepared in a superposition $1/\sqrt{2}(|\uparrow\rangle + |\downarrow\rangle)$. A short 2 ns spin-selective resonant laser pulse creates spin-photon entanglement $1/\sqrt{2}(|\uparrow 1\rangle + |\downarrow 0\rangle)$. The photons are overlapped on the beamsplitter and detected in the two output ports. Both spins are then flipped, and the NV centres are excited a second time. The detection of one photon in each excitation round heralds the entanglement and triggers individual spin readout.

then described by $1/2(|\uparrow_A\uparrow_B\rangle\,|1_A1_B\rangle + |\downarrow_A\downarrow_B\rangle\,|0_A0_B\rangle + |\uparrow_A\downarrow_B\rangle\,|1_A0_B\rangle + |\downarrow_A\uparrow_B\rangle\,|0_A1_B\rangle)$. The two photon modes, A and B, are directed to the input ports of a beamsplitter (see Fig. 3.1a), so that fluorescence observed in an output port could have originated from either NV centre. If the photons emitted by the two NV centres are indistinguishable, detection of precisely one photon on an output port would correspond to measuring the photon state $|1_A0_B\rangle \pm e^{-i\varphi}\,|0_A1_B\rangle$ (where φ is a phase that depends on the optical path length). Such a detection event would thereby project the qubits onto a maximally entangled state $|\psi\rangle = 1/\sqrt{2}(|\uparrow_A\downarrow_B\rangle \pm e^{-i\varphi}\,|\downarrow_A\uparrow_B\rangle)$.

Any realistic experiment, however, suffers from photon loss and imperfect detector efficiency; detection of a single photon is thus also consistent with creation of the state $|\uparrow\uparrow\rangle$. To eliminate this possibility, both qubits are flipped and optically excited for a second time. Since $|\uparrow\uparrow\rangle$ is flipped to $|\downarrow\downarrow\rangle$, no photons are emitted in the second round for this state. In contrast, the states $|\psi\rangle$ will again yield a single photon. Detection of a photon in both rounds thus heralds the generation of an entangled state. The second round not only renders the protocol robust against photon loss, but it also changes φ into a global phase, making the protocol insensitive to the optical path length difference[26] (see Supporting Material). Furthermore, flipping the qubits provides a refocusing mechanism that counteracts spin dephasing during entanglement generation. The final state is one of two Bell states $|\psi^{\pm}\rangle = 1/\sqrt{2}(|\uparrow_A\downarrow_B\rangle \pm |\downarrow_A\uparrow_B\rangle)$, with the sign depending on whether the same detector (+), or different detectors (−)

clicked in the two rounds.

3.3 Implementation

A key challenge for generating remote entanglement with solid-state qubits is obtaining a large flux of indistinguishable photons, in part because local strain in the host lattice can induce large variations in photon frequency. The optical excitation spectra of the NV centres (Fig. 3.3a) display sharp spin-selective transitions. Here we use the E_y transition (spin projection $m_s = 0$) in the entangling protocol and for qubit readout; we use the A_1 transition for fast optical pumping into $|\uparrow\rangle$ [20]. Due to different strain in the two diamonds, the frequencies of the E_y transitions differ by 3.5 GHz, more than 100 line-widths. By applying a voltage to an on-chip electrode (Fig. 3.1b) we tune the optical transition frequencies of one centre (NV B) through the d.c. Stark effect [13,27] and bring the E_y transitions of the two NV centres into resonance (Fig. 3.3a bottom).

Charge fluctuations near the NV centre also affect the optical frequencies. To counteract photo-ionisation we need to regularly apply a green laser pulse to re-pump the NV centre into the desired charge state. This re-pump pulse changes the local electrostatic environment, leading to jumps of several line-widths in the optical transition frequencies [28]. To overcome these effects, we only initiate an experiment if the number of photons collected during a two-laser probe stage (Fig. 3.3b) exceeds a threshold, thereby ensuring that the NV centre optical transitions are on resonance with the lasers (see Sec. 2.4.5, Fig. 2.12). The preparation procedure markedly improves the observed optical coherence: as the probe threshold is increased, optical Rabi oscillations persist for longer times (see Fig. 3.3b). For high thresholds, the optical damping time saturates around the value expected for a lifetime-limited linewidth [28], indicating that the effect of spectral jumps induced by the re-pump laser is strongly mitigated.

Besides photon indistinguishability, successful execution of the protocol also requires that the detection probability of resonantly emitted photons exceeds that of scattered laser photons and of detector dark counts. This is particularly demanding for NV centres since only about 3% of their emission is in the zero-phonon line and useful for the protocol. To minimise detection of laser photons, we use both a cross-polarised excitation-detection scheme (Fig. 3.3c inset) and a detection time filter that exploits the difference between the length of the laser pulse (2 ns) and the NV centre's excited state lifetime (12 ns) (Fig. 3.3c). For a typical detection window used, this reduces the contribution of scattered laser photons to about 1%. Combined with micro-fabricated solid-immersion lenses for enhanced collection efficiency (Fig. 3.1b) and spectral filtering for suppressing non-resonant NV emission, we obtain a detection probability of a resonant NV photon of about 4×10^{-4} per pulse — about 70 times higher than the sum of background contributions.

The degree of photon indistinguishability and background suppression can be

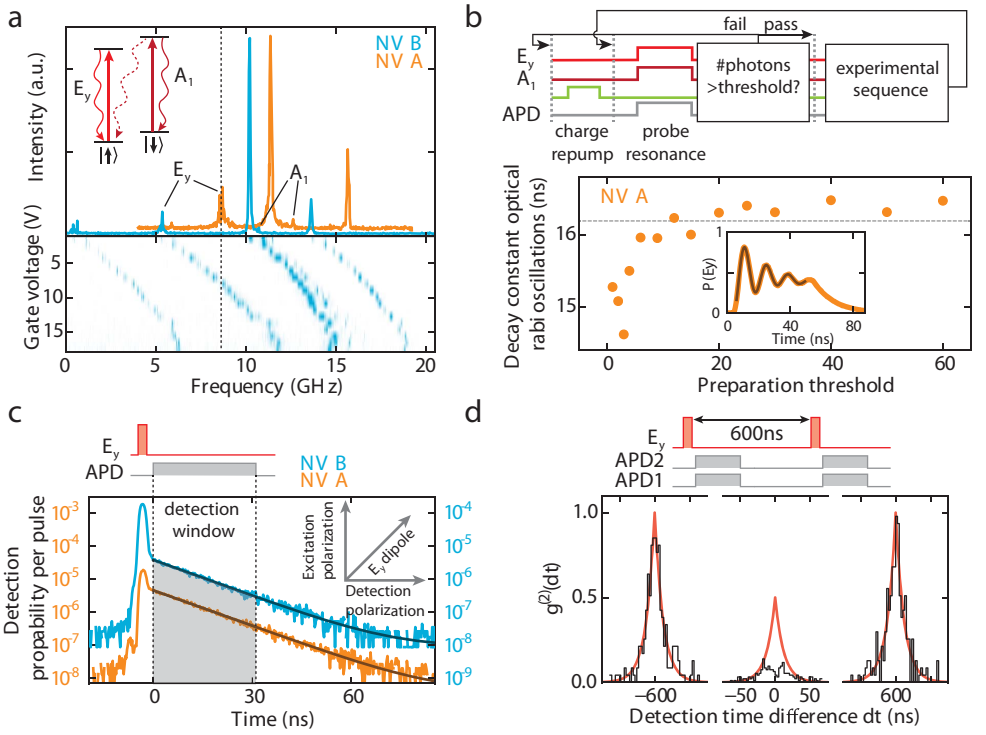

Figure 3.3 — Generating and detecting indistinguishable photons. (a) Excitation spectra; frequency relative to 470.4515 THz. By applying a voltage to the gates of NV B the E_y transitions are tuned into resonance. **(b)** Dynamical preparation of charge and optical resonance. Top: Preparation protocol. A 10 μs green laser pulse pumps the NV into its negative charge state[20]. The transition frequencies are probed by exciting the E_y and A_1 transitions for 60 μs. Conditional on surpassing a certain number of photons detected the experiment is started (pass) or preparation is repeated (fail). APD, avalanche photodiode. Bottom: Line-narrowing effect of the preparation shown by the dependence of the decay time of optical Rabi oscillations on preparation threshold. Dashed line indicates lifetime-limited damping[28]. **(c)** Resonant optical excitation and detection. The polarisation axis of the detection path is aligned perpendicular to the excitation axis. The dipole axis of the E_y transition is oriented in between these two axes (inset). Remaining laser light reflection is time-filtered by defining a photon detection window that starts after the laser pulse. **(d)** Two-photon quantum interference using resonant excitation and detection. The $g^{(2)}$ correlation function is obtained from all coincidence detection events of APD 1 and APD 2 during the entanglement experiment (see Supporting Material). The side-peaks are fit to an exponential decay; from the fit values, we obtain the expected central peak shape $g_{\perp}^{(2)}$ (red line) for non-interfering photons. The visibility of the interference is given by $(g_{\perp}^{(2)} - g^{(2)})/g_{\perp}^{(2)}$.

obtained directly from the second-order autocorrelation function $g^{(2)}$, which we extract from our entanglement experiment (see Supporting Material). For fully distinguishable photons, the value of $g^{(2)}$ would reach 0.5 at zero arrival time difference. A strong deviation from this behaviour is observed (Fig. 3.3d) due to two-photon quantum interference[29] that, for perfectly indistinguishable photons, would make the central peak fully vanish. The remaining coincidences are likely caused by (temperature-dependent) phonon-induced transitions between optically excited states[30] in NV A. The visibility of the two-photon interference observed here — $(80\pm5)\%$ for $|dt| < 2.56\,\mathrm{ns}$ — is a significant improvement over previously measured values[13,14] and key to the success of the entangling scheme.

To experimentally generate and detect remote entanglement, we run the following sequence: First, both NV centres are independently prepared into the correct charge state and brought into optical resonance according to the scheme in figure 3.3b. Then we apply the entangling protocol shown in figure 3.2 using a 600 ns delay between the two optical excitation rounds. We repeat the protocol 300 times before we return to the resonance preparation step; this number is a compromise between maximising the attempt rate and minimising the probability of NV centre ionisation. A fast logic circuit monitors the photon counts in real time and triggers single-shot qubit readout on each setup whenever entanglement is heralded, i.e. whenever a single photon is detected in each round of the protocol. The readout projects each qubit onto the $\{|\uparrow\rangle, |\downarrow\rangle\}$ states (Z-basis), or on the $\{|\uparrow\rangle \pm |\downarrow\rangle, |\uparrow\rangle \mp |\downarrow\rangle\}$ states (X or $-$X basis). The latter two are achieved by first rotating the qubit by $\pi/2$ using a microwave pulse before readout. By correlating the resulting single-qubit readout outcomes we can verify the generation of the desired entangled states. To obtain reliable estimates of the two-qubit state probabilities, we correct the raw data with a maximum-likelihood method for local readout infidelities. These readout errors are known accurately from regular calibrations performed during the experiment (see Supporting Material).

3.4 Demonstration of remote entanglement

Fig. 3.4 shows the obtained correlations. When both qubits are measured along Z (readout basis {Z,Z}), the states ψ^+ and ψ^- (as identified by their different photon signatures) display strongly anti-correlated readout results (odd parity). The coherence of the joint qubit state is revealed by measurements performed in rotated bases ({X,X}, {$-$X,X}), which also exhibit significant correlations. Furthermore, these measurements allow us to distinguish between states ψ^+ and ψ^-. For ψ^+ the {X,X} ({$-$X,X}), outcomes exhibit even (odd) parity, whereas the ψ^- state displays the opposite behaviour, as expected. The observed parities demonstrate that the experiment yields the two desired entangled states.

We calculate a strict lower bound on the state fidelity by combining the measurement

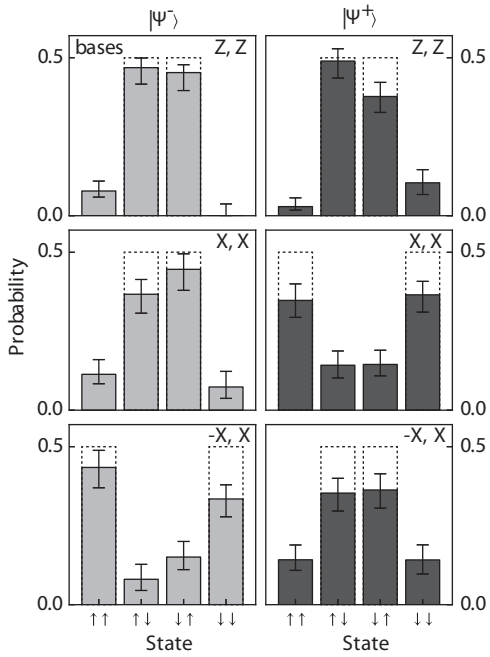

Figure 3.4 — Verification of entanglement by spin-spin correlations. Each time that entanglement is heralded the spin qubits are individually read out and their results correlated. The readout bases for NV A and NV B can be rotated by individual microwave control (see text). The state probabilities are obtained by a maximum-likelihood estimation on the raw readout results (see 3.6.8). Error bars depict 68% confidence intervals; dashed lines indicate expected results for perfect state fidelity. Data is obtained from 739 heralding events. For ψ^-, the detection window in each round is set to 38.4 ns, and the maximum absolute detection time difference $|\delta\tau|$ between the two photons relative to their laser pulses is restricted to 25.6 ns. $\delta\tau = \tau_2 - \tau_1$, where τ_1 is the arrival time of the first photon relative to the first laser pulse and τ_2 the arrival time of the second photon relative to the second laser pulse. For ψ^+ the second detection window is set to 19.2 ns with $|\delta\tau| < 12.8$ ns, in order to reduce the effect of photo-detector after-pulsing.

results from different bases (Sec. 3.6.5):

$$F = \langle \psi^{\pm} | \rho | \psi^{\pm} \rangle \geq \ 1/2(P_{\uparrow\downarrow} + P_{\downarrow\uparrow} + C) - \sqrt{P_{\uparrow\uparrow} P_{\downarrow\downarrow}}, \tag{3.1}$$

where P_{ij} is the probability for the measurement outcome ij in the {Z,Z} basis (i.e. the diagonal elements of the density matrix ρ) and C is the contrast between odd and even outcomes in the rotated bases. We find a lower bound of $(69 \pm 5)\%$ for ψ^- and $(58 \pm 6)\%$ for ψ^+, and probabilities of 99.98% and 91.8%, respectively, that the state fidelity is above the classical limit of 0.5. These values firmly establish that we have created remote entanglement.

The lower bound on the state fidelity given above takes into account the possible presence of coherence within the even-parity subspace $\{|\uparrow\uparrow\rangle, |\downarrow\downarrow\rangle\}$. However, the protocol selects out states with odd parity and therefore this coherence is expected to be absent. To compare the results to the expected value and to account for sources of error, we set the related (square-root) term in Eq. 1 to zero and obtain for the data in figure 3.4 as best estimate $F = (73 \pm 4)\%$ for ψ^- and $F = (64 \pm 5)\%$ for ψ^+.

Several known error sources contribute to the observed fidelity. Most importantly, imperfect photon indistinguishability reduces the coherence of the state. The fidelity is further decreased by errors in the microwave pulses (estimated at 3.5%), spin initialisation (2%), spin decoherence ($< 1\%$) and spin flips during the optical excitation (1%) (see 3.6.9). Moreover, ψ^+ is affected by after-pulsing, whereby detection of a photon in the first round triggers a fake detector click in the second round. Such after-pulsing leads to a distortion of the correlations (see for example the increased probability for $|\downarrow\downarrow\rangle$ in figure 3.4) and thereby a reduction in fidelity for ψ^+ (see 3.6.9). Besides these errors that reduce the actual state fidelity, the measured value is also slightly lowered by a conservative estimation for readout infidelities and by errors in the final microwave $\pi/2$ pulse used for reading out in a rotated basis.

The success probability of the protocol is given by $P_\psi = 1/2\eta_A\eta_B$. η_i is the overall detection efficiency of resonant photons from NV i and the factor $1/2$ takes into account cases where the two spins are projected into $|\downarrow\downarrow\rangle$ or $|\uparrow\uparrow\rangle$, which are filtered out by their different photon signature. In the current experiment we estimate $P_\psi \approx 1.610^{-7}$. The entanglement attempt rate is about 20 kHz, yielding one entanglement event per 10 minutes. This is in good agreement with the 739 entanglement events obtained over a time of 158 hours.

3.5 Conclusion

Creation of entanglement between distant spin qubits in diamond, as reported here, opens the door to extending the remarkable properties of NV-based quantum registers towards applications in quantum information science. A natural path forward is the incorporation of auxiliary nuclear spin qubits at the local nodes. In the following we discuss a second experiment where the nitrogen spin initialization and decoherence

protected gates are combined with an improved entanglement protocol to realize a deterministic Bell-state measurement which enables teleportation between a single nuclear spin and a distant electron spin.

3.6 Supplementary Information

3.6.1 Setup

We perform the experiments with two home-built low-temperature confocal microscopes. Each setup features lasers for off-resonant and resonant excitation, cryogenic piezoelectric positioners and high-efficiency/low background fluorescence detection paths. The zero-phonon line (ZPL) detection paths of both setups lead to the common beam splitter and photon detectors used for the entanglement generation. Each setup has an independent microwave (MW) source (Rohde & Schwarz SMB100A) and MW amplifier (Amplifier Research 20S1G4 and AR 40S1G4 for setups A and B, respectively) to drive the NV centre electron spins.

Sample A is mounted on a XYZ stepper/scanner piezo stack (Attocube) in a Janis ST-500 flow cryostat and kept at $T \approx 8\,\mathrm{K}$. Sample B is mounted on a XYZ stepper (Attocube) inside a custom-built Cryovac bath cryostat with optical access and kept at a temperature of $T \approx 4\,\mathrm{K}$.

Off resonant green excitation is provided for each of the setups by 532 nm lasers (Spectra Physics Millenia Pro and Laser 2000 Cobalt Samba for setups A and B, respectively). Two tuneable 637 nm lasers (New Focus Velocity) for independent resonant excitation are used for optical spin-pumping. For the resonant excitation pulses used to generate the entanglement both setups share a tuneable continuous wave 637 nm laser (Sirah Matisse DS). Its output is sequentially fed through an acousto-optic modulator (AOM; Crystal Technologies) and an electro-optic modulator (EOM; Jenoptik). After passing through the AOM & EOM, the beam is split using a 50/50 beam splitter, and a 30 cm adjustable delay line is inserted in one arm for fine-tuning the temporal overlap of the excitation.

The photon emission of each NV is split into a ZPL part and an off-resonant phonon sideband (PSB) part by a dichroic long-pass filter (Semrock LPD01-633RS). The PSB emission is independently detected for each setup by avalanche photo-diodes (APDs; Perkin-Elmer SPCM). The ZPL emission is further filtered by a second dichroic filter (to remove green excitation light) and a tuneable band pass filter (Semrock TBP-700B). After filtering resonant excitation light by cross-polarisation rejection the ZPL emission of NVs A and B is coupled into the input ports of a fibre-coupled beam splitter (Evanescent Optics) by polarisation-maintaining fibres. The photons leaving the output ports of the beam splitter are detected by fibre-coupled avalanche photo-diodes (Picoquant Tau-SPAD) and time-tagged by a Picoquant Hydraharp 400 system.

3.6.2 Rejection of resonant excitation light

The experimental protocol requires the resonant excitation of a single optical transition and the detection of indistinguishable resonant photons from spontaneous emission of this transition. We use polarisation rejection and time-filtering to filter residual resonant excitation light — stemming from reflections from optical elements and the sample surface — from the signal.

The excitation laser is linearly polarised and rotated using a half-wave-plate (HWP) to a non-zero angle φ with respect to the (linear) dipole of the $|\uparrow\rangle \leftrightarrow |E_y\rangle$ transition it excites (Fig. 3.5). In the detection path, the combination of a half-wave plate and polariser sets a detection axis with an angle θ in the opposite direction with respect to the NV transition dipole. A further quarter-wave-plate (QWP) corrects for circular polarisation components of the signal that are induced by optical elements in the detection path. We find the optimum in laser-rejection, NV excitation efficiency and NV collection efficiency by varying the angles φ, θ while keeping $\varphi + \theta = 90°$.

As can be seen in Fig. 3.12, reflections of the two-nanosecond excitation pulse can be clearly distinguished from the exponentially decaying NV centre emission. In this manner laser reflections that are not removed by the polarisation rejection can be removed by time-filtering.

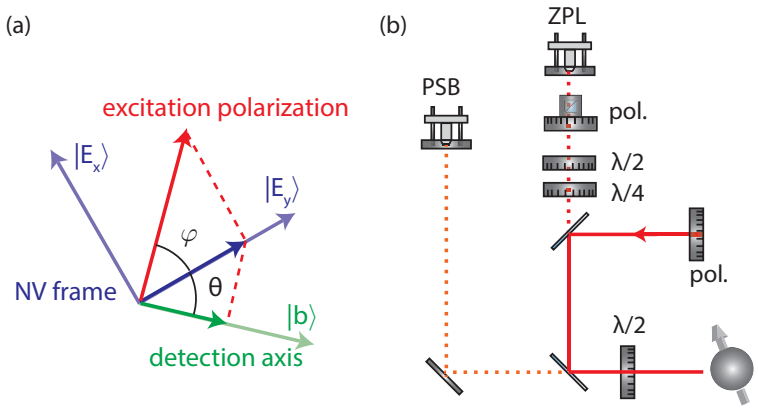

Figure 3.5 —Resonant detection and excitation. **a**, Working principle of cross-polarisation rejection. **b**, Optical setup. See text for details.

3.6.3 Experimental control

For the experiment to be feasible, a high repetition rate of the entanglement generation sequence is crucial, because the success probability per shot is small, $P_s = 1/2 \times \eta_A \eta_B \approx 10^{-7}$. We achieve a reasonable repetition rate by employing a conditional protocol as

follows (Fig. 3.6): We first ensure that both NV centres are in the negative charge state and on resonance. To this end we independently re-set the charge and resonance state of the two NVs with green laser pulses until the resonant excitation lasers are on resonance[31,32]. After this preparation we run the spin-preparation and entanglement generation sequence. In case of successful generation of entanglement we read out both spins in a single shot and return to the charge and resonance (CR) check. Otherwise, we repeat spin-preparation and entanglement generation. After 300 unsuccessful entanglement attempts we start over with the CR check. The success probabilities for passing the CR check, $P_{\mathrm{CR}} \approx 2\%$, and for successfully generating entanglement let us predict an entanglement generation rate of $\sim 1/10$ minutes. For comparison, an unconditional protocol in which charge/resonance and entanglement generation are only verified in post-processing would yield an entanglement rate of only $\sim 1/50$ hours.

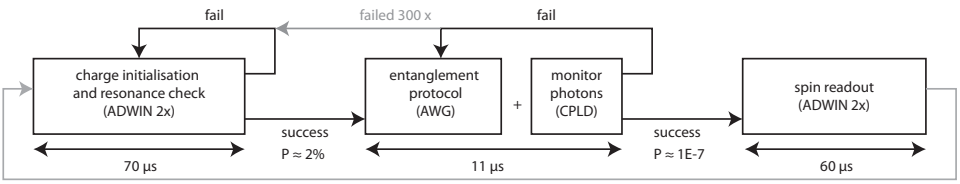

Figure 3.6 —The conditional sequence to implement the entanglement protocol. Two programmable micro-controllers with integrated DAC- and counter modules (*ADwin 2x*) independently initialise each NV centre and perform the charge-resonance check described in the main text. If both checks pass, a trigger is sent to the Arbitrary Waveform Generator (*AWG*) that executes the entanglement protocol. The protocol is run up to 300 times until it is successful. A successful attempt is recognised by a logic device (*CPLD*) that looks for a success-signature in the stream of photon clicks produced, and sends a halt trigger to the AWG when it does. The readout is then performed by the ADwins, after which the sequence starts over.

Conditional operation is implemented in the following manner: The CR check and readout is done independently for the two setups by two programmable micro-controllers with DAC- and counter modules (Adwin Gold II and Adwin Pro II for setup A and B, respectively). Once both CR checks pass, a start trigger is sent to the Arbitrary Waveform Generator (Tektronix AWG 5014C) that sequentially executes the entanglement protocol up to 300 times. For each round, the photon clicks are recorded and time-tagged by a Picoquant Hydraharp 400 system. In addition, the photon clicks are also monitored in real time by a programmable logic device (CPLD; Altera Max V development kit) that time-filters the signal and recognises a successful entanglement event; if a success occurs, a stop trigger is sent to the AWG within 50 ns to prevent it from running the next entanglement cycle. Furthermore, the logic device triggers both ADwin micro controllers to start their readout sequence. Further (more selective) time filtering is done in post-processing for the successful events, by combining the time-tagged data and spin readout data.

3.6.4 Optical Rabi oscillations

On resonance (i.e. in the absence of quasi-static spectral diffusion), the exponential damping time τ_{rabi} of the Rabi oscillations is determined by the pure optical dephasing time $T_2^{*,\mathrm{opt}}$ via[33]

$$\frac{1}{\tau_{\mathrm{rabi}}} = \frac{3}{4T_1} + \frac{1}{2T_2^{*,\mathrm{opt}}}, \tag{3.2}$$

where T_1 is the NV centre optical lifetime (about 12 ns).

As can be seen in Fig. 2b in the main text, and Fig. 3.7, τ_{rabi} saturates to the lifetime-limited value for high thresholds. Similar saturation behaviour is observed for different optical Rabi frequencies.

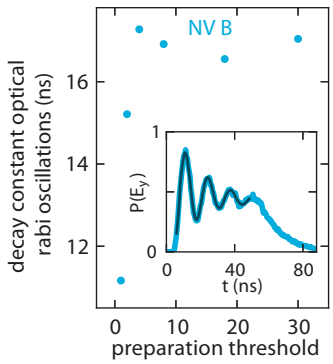

Figure 3.7 —Line-narrowing effect of the dynamical initialization of charge and resonance for NV B, exemplified by the dependence of the decay time of optical Rabi oscillations on preparation threshold. See Fig. 2b in the main text for details of the pulse sequence used.

3.6.5 Fidelity measure

We want to estimate the fidelity of the generated two-spin state $|\psi\rangle$ with respect to the ideal Bell state. We take the example of the Bell state Ψ^+:

$$\left|\Psi^+\right\rangle = (|\uparrow\rangle_{\mathrm{A}}|\downarrow\rangle_{\mathrm{B}} + |\downarrow\rangle_{\mathrm{A}}|\uparrow\rangle_{\mathrm{B}})/\sqrt{2} \equiv (|\uparrow\downarrow\rangle + |\downarrow\uparrow\rangle)/\sqrt{2}, \tag{3.3}$$

where $|\uparrow\rangle$ and $|\downarrow\rangle$ denote the $m_{\mathrm{s}} = 0$ and $m_{\mathrm{s}} = -1$ spin sub-levels of the NV centre ground state and subscripts A, B indicate the two NV centres used. The density matrix for this state is

$$\rho_{\Psi^+} = \left|\Psi^+\right\rangle\left\langle\Psi^+\right| = \frac{1}{2}\begin{pmatrix} 0 & 0 & 0 & 0 \\ 0 & 1 & 1 & 0 \\ 0 & 1 & 1 & 0 \\ 0 & 0 & 0 & 0 \end{pmatrix}. \tag{3.4}$$

The fidelity of the state $|\Psi^+\rangle$ with density matrix ρ, for both spins in the z-basis, is therefore

$$\mathcal{F} = \langle \Psi^+ | \rho | \Psi^+ \rangle = \frac{1}{2}(\rho_{22} + \rho_{33} + \Re(\rho_{23}) + \Re(\rho_{32})) = \frac{1}{2}(\rho_{22} + \rho_{33} + 2\Re(\rho_{23})). \quad (3.5)$$

The term coming from the diagonal elements, $\rho_{22} + \rho_{33}$, is given by the fraction of spin-readouts in which the outcomes from NVs A and B are anti-correlated. To estimate the off-diagonal terms we measure both spins in the X-basis by applying $\pi/2$-rotations around $\mathbf{y}$, yielding the density matrix

$$\tilde{\rho} = \left(\sqrt{Y} \otimes \sqrt{Y}\right) \rho \left(\sqrt{Y}^\dagger \otimes \sqrt{Y}^\dagger\right), \quad (3.6)$$

where the operator Y describes a π-rotation around the y-axis,

$$\sqrt{Y} = \mathrm{e}^{-\frac{\mathrm{i}}{\hbar} S_\mathrm{y} \pi/2}, \quad (3.7)$$

where S_y is the y-component of the spin-$\frac{1}{2}$ operator. The contrast between measured correlations and anti-correlations in this basis is

$$\tilde{\rho}_{11} + \tilde{\rho}_{44} - \tilde{\rho}_{22} - \tilde{\rho}_{33} = 2\Re(\rho_{23}) + 2\Re(\rho_{14}). \quad (3.8)$$

It follows from the definition of the density matrix that the absolute of $\Re(\rho_{14})$ is bounded by

$$|\ \Re(\rho_{14})\ | \leq \sqrt{\rho_{11}\rho_{44}}, \quad (3.9)$$

and therefore

$$2\Re(\rho_{23}) \geq \tilde{\rho}_{11} + \tilde{\rho}_{44} - \tilde{\rho}_{22} - \tilde{\rho}_{33} - 2\sqrt{\rho_{11}\rho_{44}}. \quad (3.10)$$

In terms of measured quantities in two bases, the fidelity has thus a strict lower bound of[34]

$$\mathcal{F} \geq \frac{1}{2}\left(\rho_{22} + \rho_{33} + \tilde{\rho}_{11} + \tilde{\rho}_{44} - \tilde{\rho}_{22} - \tilde{\rho}_{33} - 2\sqrt{\rho_{11}\rho_{44}}\right). \quad (3.11)$$

The treatment for the Bell state $|\Psi^-\rangle = (|\uparrow\downarrow\rangle - |\downarrow\uparrow\rangle)/\sqrt{2}$ and for rotations around other axes is analogous. For the best estimate of the fidelity as mentioned in the main text, the term $\sqrt{\rho_{11}\rho_{44}}$ is set to zero in the inequality above. To obtain coherence within the even-parity subspace, several errors are required to occur within the same entanglement attempt (such as two dark counts of the detector while not exciting the NV centres with the laser). The probability of such a string of events happening is negligible.

3.6.6 Spin readout

We perform single shot readout (SSRO) of the NV spin states by spin-resolved optical excitation[31]. The fidelity for reading out $|\uparrow\rangle$ correctly is given by the probability with which at least one photon is detected when $|\uparrow\rangle$ is prepared:

$$\mathcal{F}_\uparrow = p(\geq 1 | \uparrow). \quad (3.12)$$

Conversely,

$$\mathcal{F}_{\downarrow} = p(0|\downarrow), \tag{3.13}$$

after preparation of $|\downarrow\rangle$. The mean fidelity for readout of an unknown spin-state is therefore $\mathcal{F}_{\mathrm{SSRO}} = (\mathcal{F}_{\uparrow} + \mathcal{F}_{\downarrow})/2$.

Infidelities are due to photon losses and 'incorrectly' obtained photons (e.g., due to off-resonant excitation or detector dark counts), leading to wrong assignment of the spin-state. The readout result of the two-spin-state

$$|\psi\rangle = c_{\uparrow\uparrow}|\uparrow\uparrow\rangle + c_{\uparrow\downarrow}|\uparrow\downarrow\rangle + c_{\downarrow\uparrow}|\downarrow\uparrow\rangle + c_{\downarrow\downarrow}|\downarrow\downarrow\rangle \tag{3.14}$$

is therefore

$$\mathcal{R} = \begin{pmatrix} p_{\uparrow\uparrow} \\ p_{\uparrow\downarrow} \\ p_{\downarrow\uparrow} \\ p_{\downarrow\downarrow} \end{pmatrix} = E \begin{pmatrix} |c_{\uparrow\uparrow}|^2 \\ |c_{\uparrow\downarrow}|^2 \\ |c_{\downarrow\uparrow}|^2 \\ |c_{\downarrow\downarrow}|^2 \end{pmatrix}, \tag{3.15}$$

where p_{ij} is the probability for measurement outcome $i, j \in \{\uparrow, \downarrow\}$, and the induced error is described by $E = E^A \otimes E^B$, where $E^{A,B}$ describe descirbe the independent readout errors on both NV's.

3.6.7 Single-shot readout characterisation

To obtain a characterisation of the electron SSRO we perform a calibration[31] every three hours during the entanglement measurements (Fig. 3.8). We use the statistical mean and standard deviation of the fidelities from all calibration measurements as values and uncertainties for $\mathcal{F}_{\uparrow}^{\mathrm{A}}$, $\mathcal{F}_{\downarrow}^{\mathrm{A}}$, $\mathcal{F}_{\downarrow}^{\mathrm{B}}$ and $\mathcal{F}_{\uparrow}^{\mathrm{B}}$ as required for state estimation.

For the calibration measurements we take into account imperfect spin-initialisation due to incomplete optical spin pumping[31]. Measuring the probability $p_{\uparrow}^{\mathrm{init}}$ ($p_{\downarrow}^{\mathrm{init}}$) that the initialisation into $|\uparrow\rangle$ ($|\downarrow\rangle$) is successful, the readout fidelities then become

$$\mathcal{F}_{\uparrow} = \frac{1 - p_{\uparrow}^{\mathrm{init}} - p(0|\uparrow_{\mathrm{init}}) + p_{\uparrow}^{\mathrm{init}} p(0|\uparrow_{\mathrm{init}}) - p_{\downarrow}^{\mathrm{init}} p(\geq 1|\downarrow_{\mathrm{init}})}{p(0|\uparrow_{\mathrm{init}}) + p(\geq 1|\downarrow_{\mathrm{init}}) - 1}, \tag{3.16}$$

$$\mathcal{F}_{\downarrow} = \frac{1 - p_{\downarrow}^{\mathrm{init}} - p(\geq 1|\downarrow_{\mathrm{init}}) - p_{\uparrow}^{\mathrm{init}} p(0|\uparrow_{\mathrm{init}}) + p_{\downarrow}^{\mathrm{init}} p(\geq 1|\downarrow_{\mathrm{init}})}{p(0|\uparrow_{\mathrm{init}}) + p(\geq 1|\downarrow_{\mathrm{init}}) - 1}. \tag{3.17}$$

$p(0|\uparrow_{\mathrm{init}})$ ($p(\geq 1|\downarrow_{\mathrm{init}})$) are the probabilities to measure 0 (≥ 1) photons during the calibration after imperfect initialisation into $|\uparrow\rangle$ ($|\downarrow\rangle$). From independent initialisation measurements presented in Fig. 3.11 above, we estimate $p_{\uparrow}^{\mathrm{init,A}} = (99.5 \pm 0.1)\%$, $p_{\uparrow}^{\mathrm{init,B}} = (98.3 \pm 0.6)\%$, $p_{\downarrow}^{\mathrm{init,A}} = (99.7 \pm 0.2)\%$, and $p_{\downarrow}^{\mathrm{init,B}} = (99.6 \pm 0.3)\%$. The results of the calibration measurements, shown in Fig. 3.8, include this analysis.

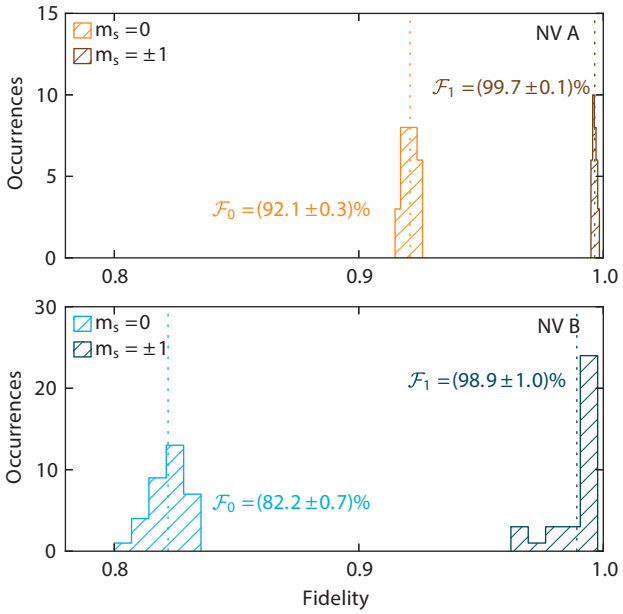

Figure 3.8 —Readout characterisation for both NVs. Imperfect spin-preparation before calibration measurements are taken into account. Histograms and means (red) of the SSRO fidelities, for both NVs, A and B, and both spin states, $m_s = 0$ and $m_s = \pm 1$, measured during all entanglement measurements.

3.6.8 Maximum likelihood estimate of the state probabilities

To estimate the eigenstate measurement populations $|c_{ij}|^2$ from a number of raw events n_{ij} in which outcome i has been obtained for NV A and outcome j for NV B, we perform a maximum likelihood estimation.

The raw events are distributed according to a multinomial distribution $f(n_{ij})$ with parameters $p_{\uparrow\uparrow}$, $p_{\uparrow\downarrow}$, $p_{\downarrow\uparrow}$, and $p_{\downarrow\downarrow} = 1 - p_{\uparrow\uparrow} - p_{\uparrow\downarrow} - p_{\downarrow\uparrow}$, the probabilities for each possible outcome, that are in turn a function of the state probabilities $|c_{ij}|^2$, as defined from Eq. (3.15) above.

The likelihood function for the probabilities, parametrized by the measurement outcomes $n_{\uparrow\uparrow}$, $n_{\uparrow\downarrow}$, $n_{\downarrow\uparrow}, n_{\downarrow\downarrow}$, and $n = n_{\uparrow\uparrow} + n_{\uparrow\downarrow} + n_{\downarrow\uparrow} + n_{\downarrow\downarrow}$, is therefore

$$\mathcal{L}\left[p_{ij}(E, |c_{ij}|^2)\right] = \frac{n!}{n_{\uparrow\uparrow}! n_{\uparrow\downarrow}! n_{\downarrow\uparrow}! n_{\downarrow\downarrow}!} p_{\uparrow\uparrow}^{n_{\uparrow\uparrow}} p_{\uparrow\downarrow}^{n_{\uparrow\downarrow}} p_{\downarrow\uparrow}^{n_{\downarrow\uparrow}} p_{\downarrow\downarrow}^{n_{\downarrow\downarrow}}. \tag{3.18}$$

The values $|c_{ij}|^2$ that maximise the likelihood are the desired populations. We verify that the found maxima are also global maxima by sampling through the parameter

space numerically.

From the Likelihood function we also obtain Bayesian confidence intervals[35] (or credible intervals) by integration. We assume a uniform prior on the intervals $p_{ij} \in (0, 1)$. The error bars in Fig. 3.9 and Fig. 3 in the main text correspond to 68% confidence intervals of the marginal probability distributions obtained from integrating over the two other probabilities. We note that the uncertainty originating form the uncertainty in the SSRO fidelities $\mathcal{F}^{\mathrm{A,B}}_{\uparrow,\downarrow}$ is negligible compared to the statistical uncertainty.

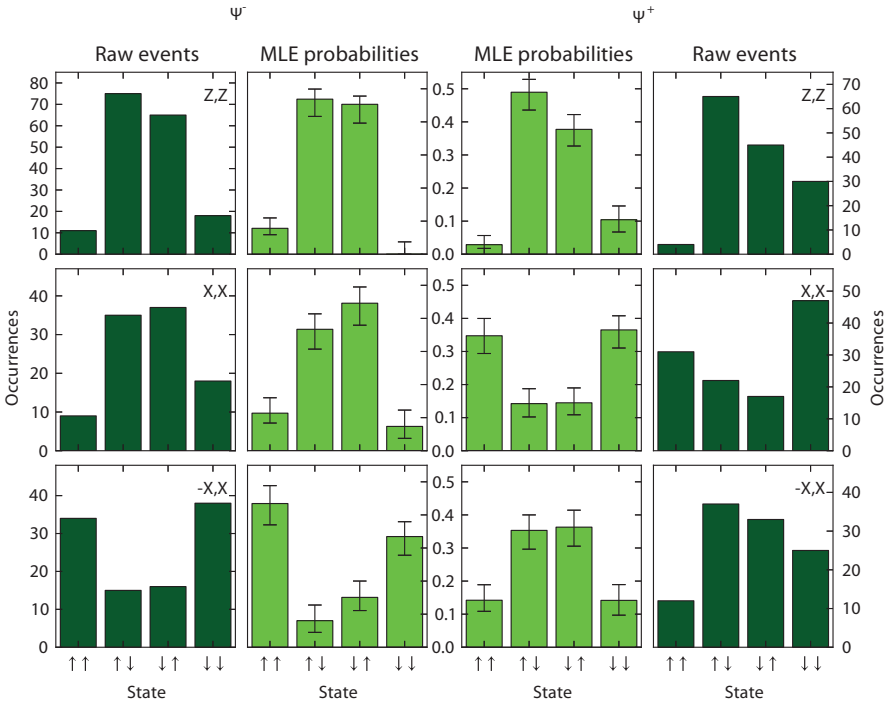

Figure 3.9 —Raw events and MLE of the state populations $|c_{ij}|^2$, for both prepared states Ψ^-,Ψ^+, and all three measurement bases Z,Z; X,X; and -X,X as described in the main text. Each of the six subplots represents an independent MLE. We note that the MLE for the ZZ-basis measurement of Ψ^- lies on the boundary of the physical space.

Maximum likelihood estimate of the fidelity

From the likelihood for a set of probabilities $p^{\mathrm{Z,Z}}_{ij}$ (for both spins measured in the Z-basis), $p^{\mathrm{X,X}}_{ij}$ (both spins measured in the X-basis) and $p^{-\mathrm{X,X}}_{ij}$ (spins measured in the

X and −X-basis, respectively), the likelihood for any value of $\mathcal{F}$ can be obtained,

$$\mathcal{L}(\mathcal{F}) = \int_{\mathcal{F}} \left(\prod_{i,j} \mathrm{d}p_{ij}^{\mathrm{Z,Z}} \mathrm{d}p_{ij}^{\mathrm{X,X}} \mathrm{d}p_{ij}^{-\mathrm{X,X}} \right) \mathcal{L}(p_{ij}^{\mathrm{Z,Z}}) \mathcal{L}(p_{ij}^{\mathrm{X,X}}) \mathcal{L}(p_{ij}^{-\mathrm{X,X}}), \tag{3.19}$$

where the integration is taken over a constant value of $\mathcal{F}_{\mathrm{LB}}$ or $\mathcal{F}$. The expression for $\mathcal{F}_{\mathrm{LB}}$ is given in Eq. (3.11); for our best estimate for the fidelity, $\mathcal{F}$, we set the square-root term in this expression to zero.

We perform this integration numerically (Fig. 3.10) for a set of values for $\mathcal{F}_{\mathrm{LB}}$ and $\mathcal{F}$. Because of the finite resolution of the numerical calculations, we fit the resulting distribution with a normalised Gaussian (free parameters are only the mean and the standard deviation) to obtain the best value and the 68% confidence interval, from the standard deviation of the Gaussian fit. Fig. 3.10 shows that this procedure is justified for our results.

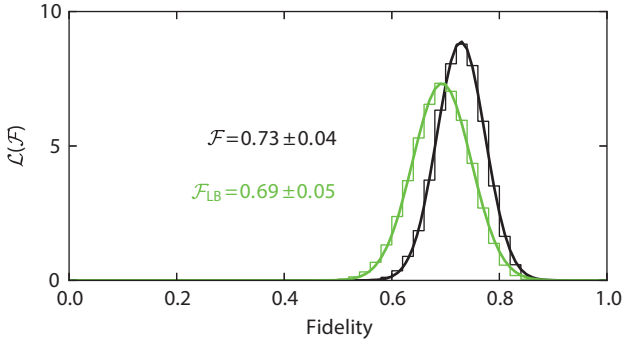

Figure 3.10 —Maximum likelihood estimation for the state fidelity. We plot the likelihood density for resulting fidelities $\mathcal{F}$ and $\mathcal{F}_{\mathrm{LB}}$ for values spaced by 0.02. Thick lines are gaussian fits from which the means and standard deviations are obtained. Here we show the resulting distribution for Ψ^-, with a length of both detection windows of 38.4 ns, and a maximal window for $|\delta\tau|$ of 25.6 ns.

3.6.9 Error estimates

Spin state initialization

We initialise the electron spin of each NV in the $m_{\mathrm{s}} = 0$ ground state by optical spin pumping on the $|m_{\mathrm{s}} = \pm 1\rangle \leftrightarrow |A_1\rangle$ transitions. The residual population in the $m_{\mathrm{s}} = \pm 1$ states can be estimated from the fluorescence time-trace obtained during the pumping (Fig. 3.11). With the initial fluorescence amplitude A and the residual

fluorescence level y_0, an upper bound for the remaining population in $m_s = \pm 1$ is given by $(y_0 - y_{bg})/(A + y_0 - y_{bg})$, where y_{bg} is the calibrated background level[31].

The fluorescence time-trace shows a clear double exponential behaviour with a fast component, on the order of a hundred nanoseconds, and a slower component on the order of microseconds. The fast timescale indicates a fast transition to a dark state that we attribute to the meta-stable singlet state.

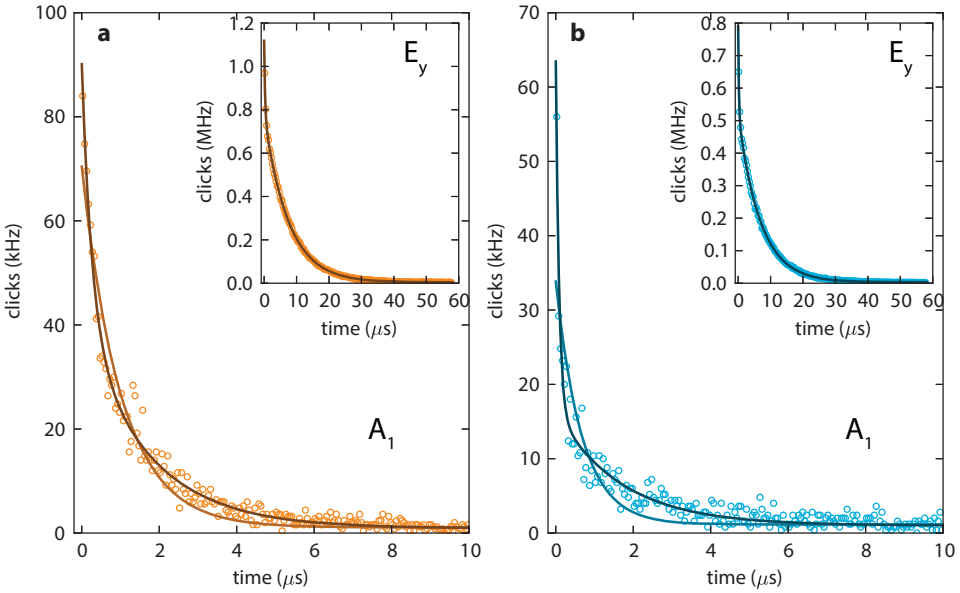

Figure 3.11 —Fluorescence time-traces during spin pumping on the $|m_s = \pm 1\rangle \leftrightarrow |A_1\rangle$ transitions for **a**, NV A and **b**, NV B. The laser power is the same as in the entanglement protocol and corresponds to near saturated driving. Insets show the curve for the $|m_s = 0\rangle \leftrightarrow |E_y\rangle$ transition (used for single-shot readout characterisation). The curves are fitted with a single-(light line) and double-(dark line) exponential decay with vertical offset. As can be seen the single exponential decay does not accurately describe the fluorescence for short time scales. From the double-exponential fits we obtain a total initial amplitude A of (89 ± 2) kHz and a offset y_0 of (0.90 ± 0.03) kHz for NV A, and for NV B an amplitude (62 ± 1) kHz and offset (1.00 ± 0.02) kHz. Background y_{bg} for NV A,B is 350 Hz and 80 Hz respectively. From this we calculate an initialisation error of (0.61 ± 0.05)% for NV A and (1.46 ± 0.05)% for NV B.

Spin-flips in the excited state manifold

During the two optical excitations in the entanglement protocol, a spin flip can occur due to spin-spin interactions in the excited state manifold. We can obtain an estimate of the probability of a spin-flip in the excited state, from the fluorescence time-trace

of the used E_y transition, given in the insets of Fig. 3.11. Since this time-trace corresponds to driving near saturation, we can extract both the average number of photons detected $\langle n_{\text{detected}} \rangle = A_1 t_1 + A_2 t_2$, and the detection efficiency $\eta = 2\frac{A_1+A_2}{\Gamma}$. Here, A_1, t_1, A_1, t_2 are the fit parameters obtained from the double exponential fit of the data and Γ is the NV optical lifetime. From this we can calculate the average number of optical cycles $\langle n \rangle$ before a spin-flip occurs:

$$\langle n \rangle = \frac{\langle n_{\text{detected}} \rangle}{\eta}, \tag{3.20}$$

and finally, an estimate for the spin-flip probability per cycle $p_{\text{flip}} = \frac{1}{\langle n \rangle}$ of $0.46\% \pm 0.01\%$ ($0.53\% \pm 0.01\%$) for NV A (NV B). We note that p_{flip} corresponds to a crude estimate for the combined probability of a direct spin-flip due to spin mixing and a transition into the meta-stable single state.

Microwave Pulse Errors

The fidelity of the microwave (MW) π and $\pi/2$ pulses is limited by the static magnetic field applied and the hyperfine interaction with the NV host nitrogen nuclear spin. Because the nitrogen spin is not initialized, the MW pulses are randomly either on resonance or detuned by the hyperfine splitting of the ^{14}N(2.2 MHz), depending on the state of the nitrogen spin. The error due to this detuning decreases with higher Rabi frequency. In the applied static magnetic field of 17.5 G, the $m_s = +1$ transition is 98 MHz detuned from the $m_s = -1$ transition. Therefore pulses with too high Rabi frequency will populate the $m_s = +1$ level. We drive Rabi oscillations for NV A of 10 MHz, and 8.6 MHz for NV B. For NV B we apply CORPSE pulses[36] to reduce the effects of the detuning and to limit the population of the $m_s = +1$ level. For NV A we apply conventional pulses to avoid heating of the sample. We simulate the effect of the two errors on the combined state of the two NVs by numerically solving a three level driven system for the pulses used for each NV and calculating the 9×9 density matrix of the joint state. From this simulation we expect to reduce the fidelity of our final Bell State to 96.5% due to pulse errors. From the same simulation we find that the population of the $m_s = +1$ state is less than 0.4% at the end of the protocol. The pulse simulations agree with independently measured π pulse contrasts for both NVs.

Spin Coherence and Dynamical Decoupling

The main source of decoherence of the NV electron spins is the interaction with a spin bath of ^{13}C nuclear spins ($S = 1/2$). We measure a free induction decay time T_2^* of (3.07 ± 0.06) μs for NV A and (0.96 ± 0.03) μs for NV B. The spin echo of the electron spins periodically collapses and revives due to entanglement and disentanglement with the surrounding ^{13}C spins precessing in the external field[37]. The revival amplitudes decay with a coherence time $T_2 = 687\,\mu$s (NV B).

For the dynamical decoupling we use a XY16 sequence[38] and choose the inter pulse delay to be twice the Larmor period of the ^{13}C spins, thus measuring always the amplitude of the revivals. When applying more than 16 pulses, the pulse errors due to off-resonant driving of the $m_s = +1$ level become significant. To circumvent this limitation we initialize the ^{14}N nuclear spin by a projective measurement[31]. This allows for a lower Rabi frequency (1.6 MHz) and therefore suppresses off-resonant driving of the $m_s = +1$ level.

Residual laser photons

After polarization rejection and time-filtering of the reflected laser photons there is still a finite probability of detecting a laser photon. Fig. 3.12 shows the combined count histogram during the first detection window on one APD, as well as the histogram counting only laser reflections, measured under similar conditions. With the chosen detection window settings there remains a $\sim 1\%$ probability that a detected photon comes from the laser instead of from either NV. Counting the possible two click events (NV+NV, NV+laser, laser+NV, laser+laser), this yields a 2% probability for a fake heralding event. Assuming that fake heralding events actually correspond to totally mixed states in the $m_s = 0$, $m_s = -1$ subspace with $\mathcal{F} = 1/4$, this yields a state infidelity of 1.5%.

Detector dark counts

Our detectors have been selected for low dark counts, with an average dark count rate of less than 25 Hz. Taking into account the two detection windows and the probability of detecting a NV photon, we estimate a relative probability of 1.3% for detecting a dark count. This yields a state infidelity of 2%.

Off-resonant excitation

The 2 ns optical π pulses applied, have a small probability of exciting an off-resonant excited state transition. From Fig. 2a in the main text it can be seen that the nearest transition corresponding to a $m_s = -1$ spin is detuned by ~ 5 GHz. We estimate the off-resonant excitation by simulating a 4-level driven system master equation in the Born-Markov approximation. Starting with an initial superposition of two ground states corresponding to the $m_s = 0$ $m_s = -1$ levels, and two excited states corresponding to the resonantly driven $m_s = 0$ excited state level and the nearest off resonant $m_s = \pm 1$ level, we find a $\sim 1\%$ probability to excite the $m_s = -1$ state.

APD After-pulsing

With the APDs used in the experiment we observe after-pulsing, fake events that are triggered some time after the actual registration of a photon. In our entanglement scheme this can lead to fake heralding events: if a photon is detected in the detection

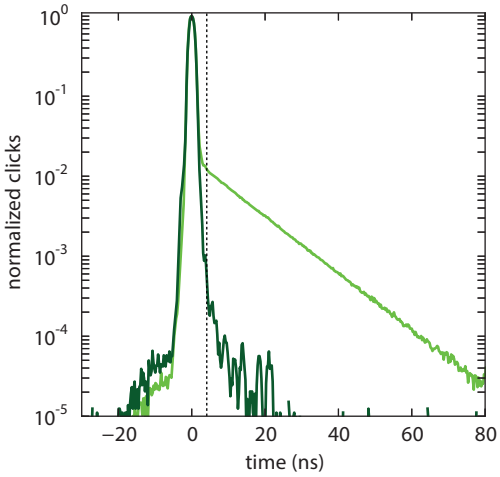

Figure 3.12 —To estimate the remaining laser photons in the time filtered signal we compare a time trace of the combined laser reflections and NV emission (light), and a time-trace showing only the laser pulse and reflections (dark). The NV data shown corresponds to the summed histogram of a single detector of the first excitation pulse of the whole entanglement dataset. The laser-only data was taken overnight under identical conditions, but with the excitation laser far detuned from the NV resonances. For both traces background is subtracted. The dashed line marks the start of the chosen detection window.

window following the first laser pulse, there is a finite chance of obtaining a click on the same detector during the second detection not coming from a photon. Such events lower the fidelity of the produced entanglement.

We perform a control experiment to estimate the chance to detect such fake heralding events (Fig. 3.13). With the excitation laser strongly detuned from resonance we run the entanglement sequence, ideally (i.e., for no after-pulsing occurring) only expecting clicks from the laser reflection and background/dark counts. Identified after-pulsing events triggered by laser pulses are shown in Fig. 3.13a. To identify these events we assume that a click preceded by a click during a laser pulse is due to after-pulsing, neglecting the possibility of accidental double-events due to background/dark counts. This analysis implicitly includes erroneous entanglement heralding due to background/dark counts.

We obtain an estimate for the ratio of probabilities for real and fake heralding of Ψ^+ generation as follows. We compare the probability for detecting an NV photon after excitation by the second laser pulse in the entanglement measurement and the probability for registering during the same window an after-pulsing event triggered by the first laser pulse (Fig. 3.13b). For fake heralding events the after-pulsing event is

triggered by an NV photon. Therefore, after-pulsing events are expected later than those triggered by the laser. We neglect this time-difference because the probability for an after-pulsing event during the detection window is almost constant.

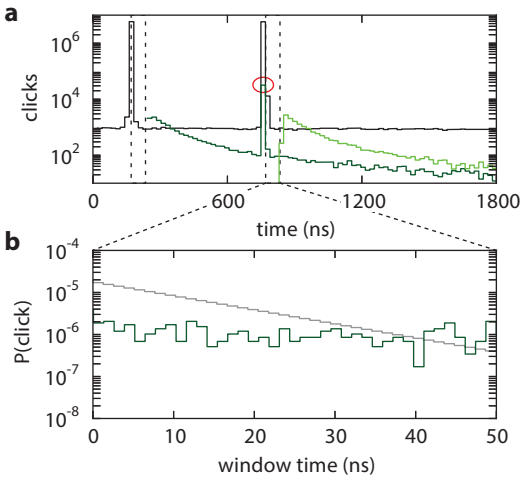

Figure 3.13 —After-pulsing. **a**, After-pulsing events following laser pulses, measured on one APD after the beam splitter. We identify detection events (green histogram curves) that are registered after a laser photon from the first and second laser pulse, respectively. The black curve shows events that are not preceded by another detection event (laser photons and dark/background counts). Dashed lines mark the range used to identify entanglement events. The high probability for a click obtained during the second laser pulse after obtaining a click during the second (data point encircled red) is not due to after-pulsing but due to the comparatively high probability of detecting a photon from both pulses in the same run. **b**, Detection probabilities for NV photons and after-pulsing events. The green curve shows the probability to detect in the second detection window an after-pulsing event triggered by the first laser pulse. The grey curve shows for comparison the typical probability to detect an NV photon.

For the chosen detection window of 19.2 ns after the second excitation we find an 8.8% relative probability to measure an afterpulsing event instead of an NV photon. Assuming that fake heralding events actually correspond to totally mixed states in the $m_s = 0$, $m_s = -1$ subspace with $\mathcal{F} = 1/4$, this leads to an infidelity of 6.5%. Note that this error only applies for the Ψ^+ state.

Dephasing

The largest contribution to the state infidelity is dephasing of the produced Bell state due to distinguishability of the photons emitted by the NV centres. An estimate for the distinguishability of the photons can be gained from the two-photon interference

presented in figure 2d of the main text. The interference shows a reduced visibility due to distinguishability of the photons. As explained in more detail in the section on phase evolution below, the visibility V gives an upper bound for the Bell state fidelity: $\mathcal{F} \leq 1/2 + 1/2V$.

The photon distinguishability is likely caused by phonon-induced transitions between optically excited states, mainly in NV A, which is operated at a higher temperature. Another contribution is the resonance check performed before the entanglement protocol to ensure both NV's are on resonance: to minimize the time necessary for the resonance check, the NV's are excited with a laser power near saturation. This can however decrease the frequency-selectivity of the resonance check, as the lines will be power broadened.

3.6.10 TPQI signature

As a measure of the indistinguishability of the photons from NV A and B we evaluate the difference between the measured $g^{(2)}(dt)$ function and the expected function $g_{\perp}^{(2)}(dt)$ that would be obtained in the case of perfectly distinguishable photons. We define the visibility as

$$V(dt) = \frac{g_{\perp}^{(2)}(dt) - g^{(2)}(dt)}{g_{\perp}^{(2)}(dt)}. \tag{3.21}$$

$g^{(2)}(dt)$ is proportional to the histogram of all coincidences obtained between photons detected on the two APDs after the beam splitter, where $dt = t_1 - t_2$, and t_1 (t_2) is the arrival time of the photon detected by APD 1 (2). We only take into account photons obtained during the same entanglement attempt. Because our pulse scheme consists of two optical π pulses, coincidence peaks only occur around $dt = 0\,\text{ns}$ (two photons detected after the same excitation pulse) and $dt = \pm 600\,\text{ns}$ (one photon detected after each excitation pulse).

To determine $g_{\perp}^{(2)}(dt)$ from our measurement we can use the coincidence count-rates of the side peaks around $dt = \pm 600\,\text{ns}$. The shape of $g_{\perp}^{(2)}(dt)$ for two single emitters in our pulse scheme is given by

$$g_{\perp}^{(2)}(dt) = \sum_{i=-1,0,1} A_i \exp(-\Gamma |dt - i \times 600\,\text{ns}|), \tag{3.22}$$

where the relative amplitudes A_i are determined by the spin-dependent excitation probabilities: The full state of the system after the first excitation round has the form (see main text)

$$|\psi\rangle = \frac{1}{2}\left(|\uparrow\uparrow\rangle\,|11\rangle + |\downarrow\downarrow\rangle\,|00\rangle + |\uparrow\downarrow\rangle\,|10\rangle + |\downarrow\uparrow\rangle\,|01\rangle\right). \tag{3.23}$$

Neglecting initialisation and microwave errors, the $|00\rangle$, $|11\rangle$ states both contribute to the A_0 peak only, and the $|01\rangle$, $|10\rangle$ states contribute to the $A_{\pm1}$ peaks only. Because all states occur with equal probability (1/4) and collection efficiency factor ($\eta_A\eta_B$), we have

$$A_0 = A_{-1} + A_{+1}, \text{ and } A_{-1} = A_{+1}. \tag{3.24}$$

The amplitudes $A_{\pm1}$ can be extracted from the measurement of $g^{(2)}(dt)$, because for the side peaks, $g^{(2)}(dt) = g_{\perp}^{(2)}(dt)$.

We note that in Fig. 3 of the main text we have renormalised the central peak such that $g_{\perp}^{(2)}(0\,\text{ns}) = 1/2$, the expected result for a conventional pulsed TPQI experiment, with an infinite pulse sequence and two single emitters, for clarity. As the same normalisation factor is applied to the measured central peak of $g^{(2)}(dt)$, this does not change the visibility.

3.6.11 Phase of the entangled state

Considering all relevant phases, the quantum state of the system after the first excitation before the beam splitter is

$$\begin{aligned}\frac{1}{2}\Big[&(e^{-i\omega_{\downarrow}^{A}t}\,|\downarrow\rangle_A\,|0\rangle_A + e^{-i\omega_{\uparrow}^{A}t}\,|\uparrow\rangle_A\,e^{ik_Ax_A-i\omega_A\tau}\,|1\rangle_A)\\ &\otimes(e^{-i\omega_{\downarrow}^{B}t}\,|\downarrow\rangle_B\,|0\rangle_B - e^{-i\omega_{\uparrow}^{B}t}\,|\uparrow\rangle_B\,e^{ik_Bx_B-i\omega_B\tau}\,|1\rangle_B)\Big],\end{aligned} \tag{3.25}$$

where $\omega_{\downarrow_i}$ and $\omega_{\uparrow_i}$ correspond to the energy levels for the two ground states $\{|\downarrow\rangle, |\uparrow\rangle\}$. ω is the transition frequency from the excited state $|e\rangle$ to the corresponding ground state and k the corresponding wavenumbers $k = \omega/c$. x is the photon path length from the NV centre to the beam splitter, the time t corresponds to the time after the first MW $\pi/2$ pulse and time τ to the time after the excitation pulse. The labels $\{A, B\}$ denote the two NV centres. See also Fig. 3.14.

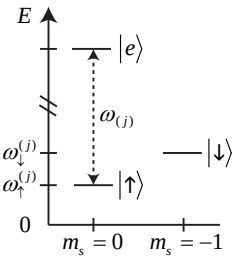

Figure 3.14 —Schematic showing the energy levels involved in the protocol, and the definitions for the various frequencies ω involved, where j labels the NV centre $j \in \{\text{A,B}\}$

.

After a single click in one of the output ports of the beam-splitter at a time $\tau_1 > k_A x_A, k_B x_B$ after the excitation (caused by one or two photons in that port), the two NV spins are projected onto the mixed state

$$|\alpha|^2 \left|\psi^{\pm}\right\rangle_{AB} \left\langle\psi^{\pm}\right|_{AB} + |\beta|^2 \left|\uparrow\right\rangle_A \left|\uparrow\right\rangle_B \left\langle\uparrow\right|_A \left\langle\uparrow\right|_B , \tag{3.26}$$

with the $(-)$-sign if we detect a click on the detector on output port 1 and a $(+)$ for a click on 2, and amplitudes α, β depending on the collection efficiencies for NV A and B, respectively. $\left|\psi^{\pm}\right\rangle_{AB}$ is an entangled state, with, at time t_{MW} after the first MW $\pi/2$-pulse, the following phase relations:

$$\begin{aligned}\left|\psi^{\pm}\right\rangle_{AB} = \frac{1}{\sqrt{2}} \Big[& e^{-i\omega_{\downarrow}^{A} t_{MW}} \left|\downarrow\right\rangle_A e^{-i\omega_{\uparrow}^{B} t_{MW}} \left|\uparrow\right\rangle_B \cdot e^{ik_B x_B - i\omega_B \tau_1} \\ & \pm \quad e^{-i\omega_{\uparrow}^{A} t_{MW}} \left|\uparrow\right\rangle_A e^{-i\omega_{\downarrow}^{B} t_{MW}} \left|\downarrow\right\rangle_B \cdot e^{ik_A x_A - i\omega_A \tau_1} \Big] . \end{aligned} \tag{3.27}$$

Here we have assumed identical NV-optical lifetimes Γ^{-1} and identical path-lengths from the beam splitter to the two different detectors, for simplicity.

At this time, the MW π-pulse is applied, flipping all $|\downarrow\rangle \longleftrightarrow |\uparrow\rangle$ in Eqns. (3.26), (3.27). Then the second excitation round proceeds, and after again detecting a single click in one of the output ports of the beam-splitter at a time $\tau_2 > k'_A x'_A, k'_B x'_B$, the two NV spins are projected onto the pure state:

$$\begin{aligned}\frac{1}{\sqrt{2}} \Big[& e^{-i\omega_{\downarrow}^{A} t_{MW}} e^{-i\omega_{\uparrow}^{\prime A} t_{MW}} \left|\uparrow\right\rangle_A e^{-i\omega_{\uparrow}^{B} t_{MW}} e^{-i\omega_{\downarrow}^{\prime B} t_{MW}} \left|\downarrow\right\rangle_B \\ & \quad \times \quad e^{ik_B x_B - i\omega_B \tau_1} e^{ik'_A x'_A - i\omega'_A \tau_2} \\ & \pm \quad e^{-i\omega_{\uparrow}^{A} t_{MW}} e^{-i\omega_{\downarrow}^{\prime A} t_{MW}} \left|\downarrow\right\rangle_A e^{-i\omega_{\downarrow}^{B} t_{MW}} e^{-i\omega_{\uparrow}^{\prime B} t_{MW}} \left|\uparrow\right\rangle_B \\ & \quad \times \quad e^{ik_A x_A - i\omega_A \tau_1} e^{ik'_B x'_B - i\omega'_B \tau_2} \Big] , \end{aligned} \tag{3.28}$$

at the spin-echo time $t = 2 \times t_{MW}$ after the first MW $\pi/2$-pulse. Here we have denoted variables corresponding to physical quantities during the second round with a prime ('). The $(+)$-sign corresponds to a click in the same detectors, the $(-)$-sign to different detectors.

The phase of the final entangled in Eq. (3.28) contains terms that oscillate with the photon frequency. To produce useful entanglement, a stable phase is required, suggesting that spatial interferometric stability of the setup and prohibitively small detector time jitter are needed.

However, the time T between the two excitation rounds is short ($T = 600\,\text{ns}$) compared to many environmental drifts of e.g. the optical path lengths and electric and magnetic fields. This suggests we should consider certain assumptions about the relation between the physical quantities in the first and second excitation rounds. In particular, possible assumptions are:

1. $\omega_\uparrow = \omega'_\uparrow$ and $\omega_\downarrow = \omega'_\downarrow$, requiring stability of the magnetic field as felt by the NV centre on the time-scale T. From independent spin-echo measurements in e.g. figure 1b in the main text we know that this assumption satisfied.
2. $x = x'$ requiring stability of the setup on the order of a wavelength (637 nm) on the time-scale T. With T being only 600ns, the setup is expected to be stable.
3. $\omega = \omega'$ (and therefore also $k = k'$). This assumption is harder to justify by independent measurement, and in fact would not be satisfied if phonon-induced transitions occur in the excited state.

If all three assumptions are satisfied, the phase relation in Eq. (3.28) simplifies:

$$\frac{1}{\sqrt{2}}\left(|{\downarrow\uparrow}\rangle_{AB} \pm e^{i\varphi}\,|{\uparrow\downarrow}\rangle_{AB}\right), \tag{3.29}$$

with

$$\varphi(\tau_1, \tau_2) = (\tau_2 - \tau_1)(\omega_A - \omega_B), \tag{3.30}$$

so that the overlap with the wanted Bell states is:

$$F(\varphi) = \frac{1}{2} + \frac{1}{2}\cos(\varphi). \tag{3.31}$$

This analysis shows that whenever the two NV centres are on resonance, perfect state fidelity could be obtained independent of the photon arrival times. Also, if the photon arrival times are identical, no dephasing is present independent of the detuning between the NV centres' optical frequencies.

3.6.12 Relation to TPQI visibility

Following Legero *et al.*[39], we have for the two-photon correlation function $g^{(2)}(t_1, t_2)$ of two photons with identical polarisation exiting from the beam-splitter:

$$g^{(2)}(t_1, t_2) = \frac{1}{4}\left|\xi_A(t_1)\xi_B(t_2) - \xi_B(t_1)\xi_A(t_2)\right|, \tag{3.32}$$

where $\xi(t)$ describes the spatio-temporal mode of the state of a single-photon light field, at time t. When these modes are written as the product of a real amplitude and a complex phase, $\xi_i(t) = \epsilon_i(t)\exp[-i\phi_i(t)]$, the correlation above function can be rewritten:

$$g^{(2)}(t_1, t_2) = g^{(2)}_\perp(t_1, t_2) - K(t_1, t_2). \tag{3.33}$$

Here, $g^{(2)}_\perp(t_1, t_2)$ is the correlation function for two fully distinguishable (perpendicularly polarised) single photons,

$$g^{(2)}_\perp(t_1, t_2) = \frac{1}{4}\left((\epsilon_A(t_1)\epsilon_B(t_2))^2 + (\epsilon_A(t_2)\epsilon_B(t_1))^2\right), \tag{3.34}$$

which is independent of the phases ϕ. $K(t_1, t_2)$, however, does depend on the phase:

$$K(t_1, t_2) = \frac{1}{2}(\epsilon_A(t_1)\epsilon_B(t_2)\epsilon_A(t_2)\epsilon_B(t_1)) \cos(\phi_A(t_1) - \phi_A(t_2) + \phi_B(t_2) - \phi_B(t_1)). \tag{3.35}$$

Finally, the visibility of the two photon interference in Eq. (3.21) is given by

$$V(t_1, t_2) = \frac{g_\perp^{(2)} - g^{(2)}}{g_\perp^{(2)}} = K/g_\perp^{(2)}. \tag{3.36}$$

Relating the above to photons emitted by our two NV centres in the situation in our experiment, and assuming the excitation time t_0, we have

$$\epsilon_i(t) = \Gamma \exp[\Gamma(t - t_0 - x_i/c)], \tag{3.37}$$

where we have assumed as before identical optical lifetime Γ^{-1} for the both NV's. Furthermore:

$$\phi_i(t) = (t - t_0)\omega_i - k_i x_i. \tag{3.38}$$

In this case, $V(t_1, t_2)$ above reduces to

$$V(t_1, t_2) = \cos[(t_2 - t_1)(\omega_A - \omega_B)]. \tag{3.39}$$

Comparing this result with Eqns. (3.30),(3.31) above, we have $\frac{1}{2} + \frac{1}{2}V(dt) = F(\varphi(\delta\tau))$, with - as before - $dt = t_2 - t_1$ and $\delta\tau = \tau_2 - \tau_1$. Since rejecting any of the assumptions (1-3) made in the previous section to arrive at the simplified expression for F will in general decrease the fidelity, V sets an upper limit for the fidelity overlap with the Bell states.

3.7 Bibliography

[1] M. A. Nielsen and I. L. Chuang. *Quantum Computation and Quantum Information.* Cambridge University Press (2000).

[2] R. Raussendorf and H. J. Briegel. A one-way quantum computer. *Physical Review Letters* **86**, 5188 (2001).

[3] D. L. Moehring *et al.* Entanglement of single-atom quantum bits at a distance. *Nature* **449**, 68 (2007).

[4] S. Ritter *et al.* An elementary quantum network of single atoms in optical cavities. *Nature* **484**, 195 (2012).

[5] J. Hofmann *et al.* Heralded entanglement between widely separated atoms. *Science* **337**, 72 (2012).

[6] H. J. Kimble. The quantum internet. *Nature* **453**, 1023 (2008).

[7] L.-M. Duan, M. D. Lukin, J. I. Cirac and P. Zoller. Long-distance quantum communication with atomic ensembles and linear optics. *Nature* **414**, 413 (2001).

[8] L. Childress, J. M. Taylor, A. S. Sørensen and M. D. Lukin. Fault-tolerant quantum communication based on solid-state photon emitters. *Physical Review Letters* **96**, 070504 (2006).

[9] T. D. Ladd *et al.* Quantum computers. *Nature* **464**, 45 (2010).

[10] E. Togan *et al.* Quantum entanglement between an optical photon and a solid-state spin qubit. *Nature* **466**, 730 (2010).

[11] W. B. Gao, P. Fallahi, E. Togan, J. Miguel-Sanchez and A. Imamoglu. Observation of entanglement between a quantum dot spin and a single photon. *Nature* **491**, 426 (2012).

[12] K. De Greve *et al.* Quantum-dot spin-photon entanglement via frequency down-conversion to telecom wavelength. *Nature* **491**, 421 (2012).

[13] H. Bernien *et al.* Two-photon quantum interference from separate nitrogen vacancy centers in diamond. *Physical Review Letters* **108**, 043604 (2012).

[14] A. Sipahigil *et al.* Quantum interference of single photons from remote nitrogen-vacancy centers in diamond. *Physical Review Letters* **108**, 143601 (2012).

[15] R. B. Patel *et al.* Two-photon interference of the emission from electrically tunable remote quantum dots. *Nature Photonics* **4**, 632 (2010).

[16] E. B. Flagg *et al.* Interference of single photons from two separate semiconductor quantum dots. *Physical Review Letters* **104**, 137401 (2010).

[17] G. D. Fuchs, V. V. Dobrovitski, D. M. Toyli, F. J. Heremans and D. D. Awschalom. Gigahertz dynamics of a strongly driven single quantum spin. *Science* **326**, 1520 (2009).

[18] G. d. Lange, Z. H. Wang, D. Ristè, V. V. Dobrovitski and R. Hanson. Universal dynamical decoupling of a single solid-state spin from a spin bath. *Science* **330**, 60 (2010).

[19] T. van der Sar *et al.* Decoherence-protected quantum gates for a hybrid solid-state spin register. *Nature* **484**, 82 (2012).

[20] L. Robledo *et al.* High-fidelity projective read-out of a solid-state spin quantum register. *Nature* **477**, 574 (2011).

[21] P. Neumann *et al.* Single-shot readout of a single nuclear spin. *Science* **329**, 542 (2010).

[22] P. Neumann *et al.* Multipartite entanglement among single spins in diamond. *Science* **320**, 1326 (2008).

[23] P. C. Maurer *et al.* Room-temperature quantum bit memory exceeding one second. *Science* **336**, 1283 (2012).

[24] W. Pfaff *et al.* Demonstration of entanglement-by-measurement of solid-state qubits. *Nature Physics* **9**, 29 (2013).

[25] M. D. Barrett *et al.* Deterministic quantum teleportation of atomic qubits. *Nature* **429**, 737 (2004).

[26] S. D. Barrett and P. Kok. Efficient high-fidelity quantum computation using matter qubits and linear optics. *Physical Review A* **71**, 060310 (2005).

[27] L. C. Bassett, F. J. Heremans, C. G. Yale, B. B. Buckley and D. D. Awschalom. Electrical tuning of single nitrogen-vacancy center optical transitions enhanced by photoinduced fields. *Physical Review Letters* **107**, 266403 (2011).

[28] L. Robledo, H. Bernien, I. van Weperen and R. Hanson. Control and coherence of the optical transition of single nitrogen vacancy centers in diamond. *Physical Review Letters* **105**, 177403 (2010).

[29] C. K. Hong, Z. Y. Ou and L. Mandel. Measurement of subpicosecond time intervals between two photons by interference. *Physical Review Letters* **59**, 2044 (1987).

[30] K.-M. C. Fu *et al.* Observation of the dynamic jahn-teller effect in the excited states of nitrogen-vacancy centers in diamond. *Physical Review Letters* **103**, 256404 (2009).

[31] L. Robledo *et al.* High-fidelity projective read-out of a solid-state spin quantum register. *Nature* **477**, 574 (2011).

[32] W. Pfaff *et al.* Demonstration of entanglement-by-measurement of solid-state qubits. *Nature Phys.* (2012).

[33] L. Robledo, H. Bernien, I. van Weperen and R. Hanson. Control and Coherence of the Optical Transition of Single Nitrogen Vacancy Centers in Diamond. *Phys. Rev. Lett.* **105**, 177403 (2010).

[34] B. B. Blinov, D. L. Moehring, L.-M. Duan and C. Monroe. Observation of entanglement between a single trapped atom and a single photon. *Nature* **428**, 153 (2004).

[35] J. K. Lindsey. *Parametric Statistical Inference*. Clarendon Press, Oxford, UK (1996).

[36] H. K. Cummins, G. Llewellyn and J. A. Jones. Tackling systematic errors in quantum logic gates with composite rotations. *Phys. Rev. A* **67**, 42308 (2003).

[37] L. Childress *et al.* Coherent dynamics of coupled electron and nuclear spin qubits in diamond. *Science* **314**, 281 (2006).

[38] T. Gullion, D. B. Baker and M. S. Conradi. New, compensated carr-purcell sequences. *J. Magn. Reson.* **89**, 479 (1990).

[39] T. Legero, T. Wilk, A. Kuhn and G. Rempe. Characterization of Single Photons Using Two-Photon Interference. M. O. Scully and G. Rempe (editors), *Advances In Atomic, Molecular, and Optical Physics*, Academic Press, 253–289 (2006).

Chapter 4

Unconditional teleportation between solid-state qubits separated by three metres

W. Pfaff, B. Hensen, H. Bernien, S.B. van Dam, M.S. Blok, T.H. Taminiau, M.J. Tiggelman, R.N. Schouten, M. Markham, D.J. Twitchen and R. Hanson

Quantum teleportation allows for transferring arbitrary quantum states between remote parties that share an entangled state as resource. Such teleportation is an essential ingredient for the operation of a quantum network. Here we demonstrate deterministic teleportation of the quantum state of a nuclear spin onto an electronic spin over three metres. We combine the previously attained remote entanglement between two NV electronic spins with a local Bell-state measurement that acts on one of the entangled electronic spins and a source qubit encoded in a nuclear spin. This scheme allows us to teleport a source state prepared on the nuclear spin onto the remote electronic spin with a fidelity that clearly exceeds the classically allowed value. Our result shows that the NV is a prime candidate for the realisation of a macroscopic quantum network.

The results in this chapter have been published in *Science* **345**, 532 (2014).

4.1 Introduction

Teleportation allows quantum information to be faithfully transmitted over arbitrary distances provided the two parties ("Alice" and "Bob") have previously established a shared entangled state and can communicate classically. In the teleportation protocol (Fig. 4.1) Alice is initially in possession of the state to be teleported (qubit 1) which is most generally given by $|\psi\rangle = \alpha\,|0\rangle + \beta\,|1\rangle$. Alice and Bob each have one qubit of an entangled pair (qubits 2 and 3) in the joint state $|\Psi^-\rangle_{23} = (|01\rangle_{23} - |10\rangle_{23})/\sqrt{2}$. The combined state of all three qubits can be rewritten as

$$\begin{aligned} |\psi\rangle_1 \otimes |\Psi^-\rangle_{23} = \frac{1}{2}\big(& |\Phi^+\rangle_{12} \otimes (\alpha\,|1\rangle_3 - \beta\,|0\rangle_3) \\ & + |\Phi^-\rangle_{12} \otimes (\alpha\,|1\rangle_3 + \beta\,|0\rangle_3) \\ & + |\Psi^+\rangle_{12} \otimes (-\alpha\,|0\rangle_3 + \beta\,|1\rangle_3) \\ & - |\Psi^-\rangle_{12} \otimes (\alpha\,|0\rangle_3 + \beta\,|1\rangle_3)\big), \end{aligned} \tag{4.1}$$

where $|\Phi^\pm\rangle = (|00\rangle \pm |11\rangle)/\sqrt{2}$ and $|\Psi^\pm\rangle = (|01\rangle \pm |10\rangle)/\sqrt{2}$ are the four Bell states. To teleport the quantum state Alice performs a joint measurement on her qubits (qubits 1 and 2) in the Bell basis, projecting Bob's qubit into a state that is equal to $|\psi\rangle$ up to a unitary operation that depends on the outcome of Alice's measurement. Alice sends the outcome via a classical communication channel to Bob, who can then recover the original state by applying the corresponding local transformation.

Because the source qubit state always disappears on Alice's side, it is irrevocably lost whenever the protocol fails. Therefore, to ensure that each qubit state inserted into the teleporter unconditionally re-appears on Bob's side, Alice must be able to distinguish between all four Bell states in a single shot and Bob has to preserve the coherence of the target qubit during the communication of the outcome and the final conditional transformation. Several pioneering experiments have explored teleportation between remote nodes[1–3] but unconditional teleportation between long-lived qubits[4–6] has so far only been demonstrated within a local qubit register[7–9].

We demonstrate unconditional teleportation between diamond spin qubits residing in independent setups separated by 3 meters. This result is achieved by fully separating the generation of remote entanglement (the preparation of the teleporter) as from the two-qubit Bell-state measurement and feed-forward (the actual teleportation action). In particular, a photonic channel is used to generate heralded remote entanglement between two nitrogen-vacancy (NV) center electronic spins, while the teleportation protocol solely exploits matter qubits that – unlike photonic qubits – allow for a deterministic Bell-state measurement with current technology. The source state is encoded in a nuclear spin close to one of the NV electron spins after preparation of the teleporter. We preserve the target qubit's coherence by dynamical decoupling while the measurement outcome is forwarded and the final correction pulse is applied.

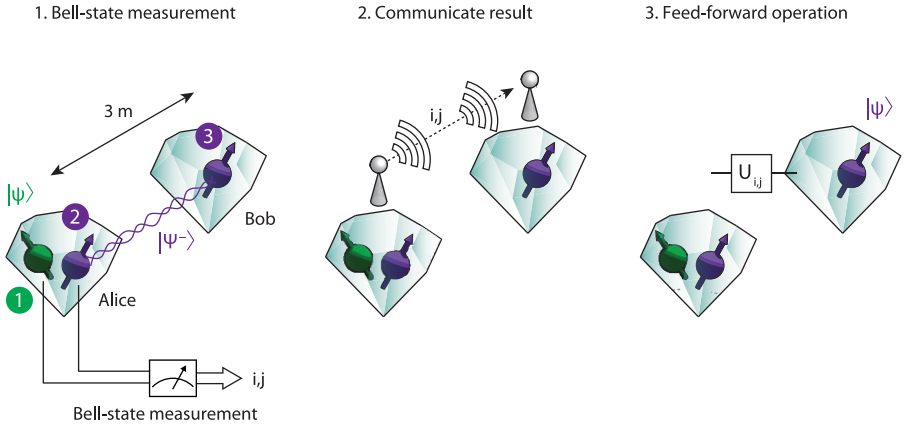

Figure 4.1 — Teleportation scheme. General scheme for teleportation. In our experiment Alice and Bob each control a single NV centre in a single-crystal CVD-grown diamond by operating an independent cryogenic confocal microscope setup (T = 8 K for Alice and T = 4 K for Bob).

This protocol ensures that the source state is successfully teleported in each of the experimental runs.

4.2 Implementation

Alice and Bob each operate an independent low-temperature confocal microscope setup that addresses a single NV centre. The two NV electronic spins (labeled as qubits 2 and 3) are initialized in the non-local entangled state $|\Psi^-\rangle_{23} = (|01\rangle_{23} - |10\rangle_{23})/\sqrt{2}$ according to the protocol described in 3.2, with the following improvements: We have further enhanced the efficiency of photon collection from our device through optimization of the SIL fabrication and by adding an anti-reflection coating. Also, we have significantly improved both the spectral stability of the NV centre's optical transition and the charge state initialization by resonant re-pumping on the neutral-charge state zero-phonon line[10]. As a result we were able to increase the generation rate of the entangled state $|\Psi^-\rangle_{23}$ fivefold to $1/250\,\mathrm{s}^{-1}$ and improve the entangled state fidelity from 0.73 to an estimated 0.87.

The additional qubit in Alice's node — essential for making the teleportation unconditional — is provided by the nitrogen-14 nuclear spin of Alice's NV (qubit 1). Before establishing the entanglement link, this nuclear spin is initialized into state $|1\rangle$ by a projective measurement via the electron spin[11]. We reinitialize the nuclear spin after each 250 entanglement attempts in order to preserve its purity (Figs. 4.2a,b). We prepare the source state after establishing remote entanglement, thus avoiding possible dephasing of the source state by repeated optical excitation of the nearby electron[12,13]

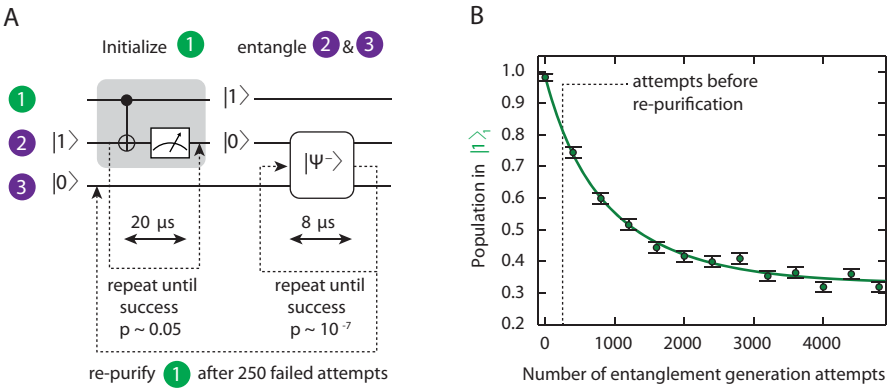

Figure 4.2 — Preparation of the teleporter. (a) Circuit diagram for the periodic measurement-based re-initialization of the nuclear spin (qubit 1) in between remote entanglement generation attempts. Both the probability for success per attempt and the time duration of a single attempt are indicated for the initialization by measurement of qubit 1 and the generation of entanglement between qubits 2 and 3. **(b)** Measured probability $\mathrm{P}(|1\rangle)$ to preserve the initialized nuclear spin state $|1\rangle$ as a function of number of entanglement generation attempts N_{ent}. A fit (solid line) to a rate-equation model yields a probability of $(0.85 \pm 0.05) \times 10^{-3}$ per entanglement generation attempt that the nuclear spin flips. The dashed line marks the maximum number of attempts before the nuclear spin is re-initialized ($N_{\mathrm{ent}} = 250$).

during entanglement generation. We employ a decoherence-protected gate[14] on Alice's side to set the nuclear spin to the source state $|\psi\rangle = \alpha\,|0\rangle + \beta\,|1\rangle$. This gate combines two nuclear spin rotations with a refocusing pulse on the electron spin such that the entangled state is efficiently preserved for the duration of the gate (Figs. 4.3a). This operation concludes the preparation of the teleporter and the insertion of the source qubit, with the three-qubit system left in the state $|\psi\rangle_1 \otimes |\Psi^-\rangle_{23} = (\alpha\,|0\rangle_1 + \beta\,|1\rangle_1) \otimes (|01\rangle_{23} - |10\rangle_{23})/\sqrt{2}$.

At the heart of unconditional qubit teleportation is a deterministic Bell-state measurement (BSM) by Alice on qubits 1 and 2 that generally involves two steps. First, the four Bell states are mapped onto the four different qubit eigenstates $|i\rangle_1\,|j\rangle_2$ by quantum gate operations. In the second step each of the two qubits is read out in a single shot and the two measurement outcomes are sent to Bob. Our implementation of this scheme is shown in Fig. 4.3a. We implement the Bell-state mapping by applying a two-qubit controlled-NOT gate (CNOT) followed by a $\pi/2$ rotation on the nuclear spin using another decoherence-protected gate. Then we read out the electron spin in a single shot (average fidelity 0.963 ± 0.005). Finally we read out the nuclear spin by mapping its state onto the electron spin followed by electron spin readout. The two single-shot readout results give the outcome of the BSM.

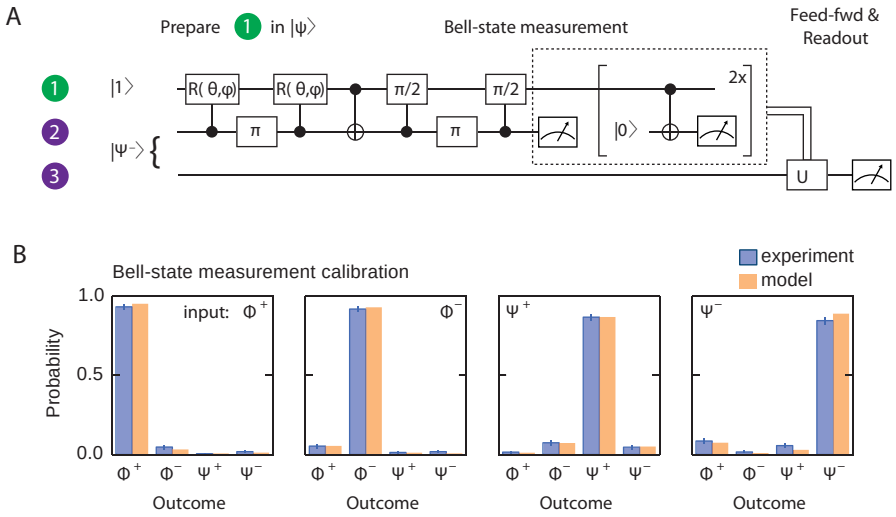

Figure 4.3 — Deterministic Bell-state measurement (BSM) and real-time feed-forward. **(a)** Circuit diagram of our implementation. The label 'e' ('N') indicates operations acting on the electron spin (nitrogen nuclear spin). To enhance the readout fidelity for the nuclear spin, we perform the mapping to the electron spin via a CNOT and the subsequent electron readout twice. While Alice is performing her BSM Bob applies an XY4 decoupling sequence on his electron qubit. After receiving the BSM outcome from Alice, Bob applies the feed-forward operation U and reads out his qubit. $\pi_{x,y}$ denote rotations around the x-axis and y-axis, respectively. **(b)** Calibration of the BSM by inserting the four different Bell states on Alice's side and determining the probability with which the ideal outcome is observed (blue bars). Data is not corrected for imperfect preparation of the input states. Expectations based on independently determined experimental imperfections are shown in orange. Error bars are two statistical s.d.

We benchmark the BSM by preparing each of the four Bell states as input states in Alice's register (Fig. 4.3b). This procedure yields an uncorrected mean fidelity, given by the probability to obtain the measurement result corresponding to the prepared Bell state, of 0.89 ± 0.02. To gain more insight into the sources of imperfections we compare the data with numerical simulations that use the independently determined infidelities of the nuclear spin initialization, CNOT gate, and electron single-shot readout as input. These simulations predict an average fidelity of 0.9 (Fig. 4.3b), in excellent agreement with the data. Taking known errors in the preparation of the input states into account, we infer a BSM fidelity of 0.93 ± 0.02.

The final challenge for successful unconditional teleportation is to maintain the coherence of Bob's target qubit (qubit 3) during the BSM and feed-forward. In our experiment, Bob's qubit is mostly affected by interactions with the surrounding nuclear spin bath. We counteract this decoherence by applying an XY4 dynamical decoupling

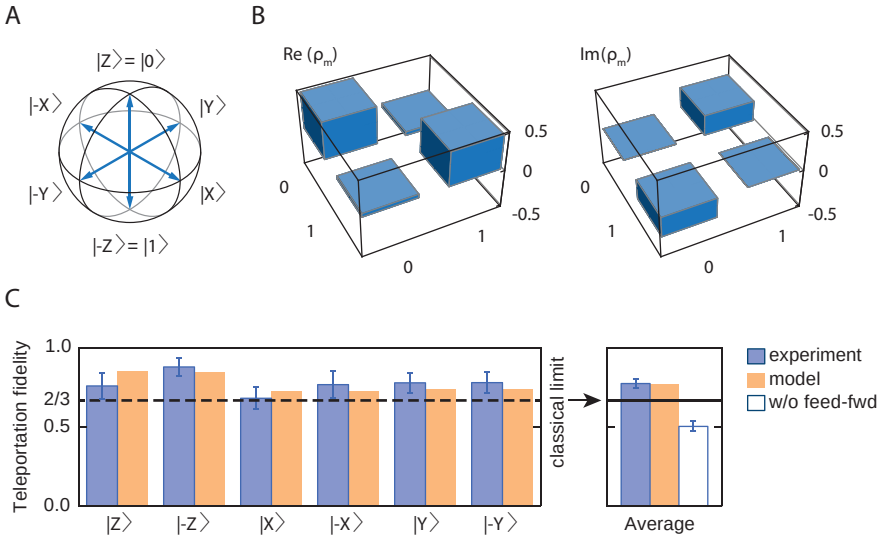

Figure 4.4 — Demonstration of unconditional quantum teleportation between remote qubits. **(a)** Bloch sphere with the six mutually unbiased basis states that we teleport. $|\pm X\rangle = (|0\rangle \pm |1\rangle)/\sqrt{2}$, $|\pm Y\rangle = (|0\rangle \pm \mathrm{i}\,|1\rangle)/\sqrt{2}$. **(b)** State tomography after teleportation of the input state $|Y\rangle$. We determine the density matrix ρ_{m} by measuring the expectation values of the Pauli spin operators, $\langle\sigma_x\rangle$, $\langle\sigma_y\rangle$, $\langle\sigma_z\rangle$, where the required qubit rotations before readout are performed conditional on the BSM outcome. The measured (ideal) entries of the density matrix are $\rho_{00} = 1 - \rho_{11} = 0.52 \pm 0.08$ (0.5) and $\rho_{01} = \rho_{10}^{*} = 0.05 \pm 0.08 - \mathrm{i}0.28 \pm \mathrm{i}0.07$ $(-\mathrm{i}0.5)$, respectively. **(c)** Average teleportation fidelity from the measured fidelities of the six states (blue bars). Sample sizes are (left to right) 54, 89, 73, 49, 52, and 47. Predictions from simulations are shown in orange. Without feed-forward, the target state is completely mixed (white bar). The horizontal line marks the classical limit of $2/3$. Data is not corrected for source state initialization errors. Uncertainties are one statistical s.d.

sequence[15]. The time between entanglement generation and the triggering of the feed-forward operation based on the BSM outcome is $300\,\mu$s. For this duration the decoupling protocol preserves the qubit state with an average fidelity of 0.96 ± 0.02.

We first verify that the teleporter is calibrated correctly by applying it to the nominal input state $|Y\rangle = (|0\rangle + \mathrm{i}\,|1\rangle)/\sqrt{2}$ and performing tomography on the state that appears on Bob's side. The reconstructed density matrix (Fig. 4.4B) shows that the target state vector is aligned well with Y and therefore that the reference frames of Alice and Bob are correctly set.

4.3 Results

To prove that our quantum teleporter outperforms any classical communication strategy, we teleport an unbiased set of six basis states $|\psi\rangle$ (Fig. 4.4A) and determine the fidelity of the teleported state on Bob's side with respect to the ideal input state. In these experiments we use a feed-forward operation that maps the ideal state of qubit 3 onto a qubit eigenstate such that the readout directly yields the teleportation fidelity. Since the feed-forward operation is conditional on the BSM outcome, ignoring the BSM outcome yields a completely mixed state and random outcomes ensuring that no information is transmitted. Without feed-forward we indeed observe an average teleportation fidelity of $\langle F\rangle = 0.50 \pm 0.03$ (Fig. 4.4C). In contrast, including the feed-forward loop we find $\langle F\rangle = 0.77 \pm 0.03$. This value exceeds the classical limit of 2/3 by more than 3 standard deviations, thus proving the quantum nature of our teleporter. We note that this fidelity presents a lower bound on the actual teleportation fidelity because it does not take into account initialization errors of the source state. Importantly, this result is obtained without any post-selection: each teleportation attempt is included in the data presented here.

We also simulate the outcomes by using independently determined infidelities in the protocol. The only unknown parameter is the fidelity of the entangled state shared by Alice and Bob. We find that our data is well reproduced by the simulations if we assume a fidelity to the ideal Bell state $|\Psi^-\rangle_{23}$ of 0.87 (Fig. 4.4C). The simulations also enable us to quantify the effect of imperfect initialization of the source qubit on the measured fidelities. In this way we estimate the teleportation fidelity to be ~ 0.86.

4.4 Conclusion

The ability to generate remote entanglement and to control and read out multiple qubits per node as shown in the present teleportation experiment makes NV centres a leading candidate for realizing a quantum network. Our teleportation scheme is both unconditional and scalable to large distances as it can mitigate photon loss by heralding and purification of the distributed entangled state[16]. In future experiments we aim to supplement our current capabilities with quantum memories that are robust against optical excitation of the electrons, enabling remote entanglement purification and the connection of multiple nodes into the network. A promising route is the use of weakly coupled nuclear spins[17–19] on which multi-qubit quantum control has very recently been demonstrated[20]. For such nuclear spins, coherence times of over 1 second under optical excitation have been reported[21], while the incorporation of NV centres into optical cavities may enable remote entanglement generation on millisecond timescales[22]. Furthermore, the entanglement and readout fidelities reported here are sufficient for a violation of a Bell inequality with the detection loophole closed, making NV centres a promising system for realizing a loophole-free Bell test and device-independent quantum key distribution[23].

4.5 Supplementary Information

4.5.1 Conventions

The basis states used for the electrons are $|0\rangle = |m_\mathrm{s} = 0\rangle$ and $|1\rangle = |m_\mathrm{s} = -1\rangle$. For the nitrogen, $|0\rangle = |m_\mathrm{I} = 0\rangle$ and $|1\rangle = |m_\mathrm{I} = -1\rangle$. When specifying joint quantum states, the first qubit is the nitrogen on site A, the second the electron on site A, and the third the electron on site B. Teleportation is performed from qubit 1 onto qubit 3.

By x, y, z we denote $\pi/2$ rotations around the $+X, +Y, +Z$ axes respectively. Bars over gate symbols indicate negative rotation sense. In the measurement sequences, rotations around $+X, +Y$ correspond to phases of the applied driving pulses of $+90°$ and $0°$, respectively. We prepare $|x\rangle \equiv (|0\rangle + |1\rangle)/\sqrt{2}$ by $y\,|0\rangle$ and $|y\rangle \equiv (|0\rangle + \mathrm{i}\,|1\rangle)/\sqrt{2} = \bar{x}\,|0\rangle$. Capital letters X, Y, Z indicate π rotations.

Hamiltonian of Alice

The relevant energy levels of the electron and nuclear spins of Alice are depicted in Fig. 4.7a. We chose the rotating frame (Fig. 4.7b) such that the relevant Hamiltonian without driving can be written as

$$\mathcal{H}_0^\mathrm{A} = \begin{pmatrix} -A & 0 & 0 & 0 \\ 0 & 0 & 0 & 0 \\ 0 & 0 & 0 & 0 \\ 0 & 0 & 0 & 0 \end{pmatrix}, \tag{4.2}$$

where $A = 2\pi \times 2.19\,\mathrm{MHz}$ is the parallel hyperfine coupling constant of electron and nitrogen at low temperatures. The spin eigenstates are $|00\rangle, |01\rangle, |10\rangle, |01\rangle$.

4.5.2 Desired state evolution

Source state preparation

After generating entanglement, we start with the state

$$|1\rangle\,(|01\rangle - |10\rangle)\,/\sqrt{2}. \tag{4.3}$$

We perform the desired rotation on the nitrogen spin for the $m_\mathrm{s} = -1$manifold, then apply a π-pulse to the electron and repeat the operation. In this way the operation on the nitrogen spin is unconditional on the electron state and the electron phase is protected by a spin-echo. With an RF operation $|1\rangle \mapsto \alpha\,|0\rangle + \beta\,|1\rangle$ this procedure yields

$$\frac{1}{\sqrt{2}}\left(\left(\mathrm{e}^{-\mathrm{i}A(t-t_0)}\alpha\,|0\rangle + \beta\,|1\rangle\right)|00\rangle + (\alpha\,|0\rangle + \beta\,|1\rangle)\,|11\rangle\right). \tag{4.4}$$

Note that the states associated with $|00\rangle$ on Alice's side accumulate a phase during free evolution time, t, due to the choice of rotating frame. t_0 is the time at which the

π-pulse on the electron is performed during preparation. By chosing the evolution time such that $A(t-t_0)$ is a multiple of 2π the initial state can be factorized. We implement the unconditional rotation of the electron spin with a CORPSE pulse that provides a π rotation that is insensitive against detuning over a range of a few MHz[24].

Bell-state measurement

The BSM consists of a CNOT rotation around the $+Y$ axis on Alice's electron spin, conditional on the nitrogen spin being in $|0\rangle$, followed by a $\pi/2$ rotation around the $+Y$ axis on the nitrogen spin. We implement the CNOT by rotating $m_{\mathrm{I}} = -1$ by π and $m_{\mathrm{I}} = 0$ by 2π, achieved by a pulse with Rabi frequency $A/\sqrt{3}$. During this pulse Alice's states $|00\rangle$ and $|01\rangle$ are not unaffected. In particular, the time-dependent phase of the state $|00\rangle$ is reduced compared to not performing the pulse (or compared to the case of an ideal CNOT gate in which only a real $\mathbb{1}$ operation would be applied to this state) because some population temporarily leaves this state. Conversely, $|01\rangle$ will acquire some phase because some population will temporarily be in $|00\rangle$. An unconditonal rotation of the nitrogen spin is achieved in the same was as for preparation, by performing the operation twice, with an electron flip in between. After these gate operations we have

$$\begin{aligned}\frac{1}{2}\Big[& |00\rangle \left(\beta\,|0\rangle - \mathrm{e}^{\mathrm{i}\lambda}\alpha\,|1\rangle\right) \\ & + |01\rangle \left(\mathrm{e}^{-\mathrm{i}A(t_1-t_0)-\mathrm{i}\kappa}\alpha\,|0\rangle + \beta\,|1\rangle\right) \\ & + |10\rangle \left(-\beta\,|0\rangle - \mathrm{e}^{\mathrm{i}\lambda}\alpha\,|1\rangle\right) \\ & + |11\rangle \left(\mathrm{e}^{-\mathrm{i}A(t_1-t_0)-\mathrm{i}\kappa}\alpha\,|0\rangle - \beta\,|1\rangle\right)\Big], \end{aligned} \tag{4.5}$$

where t_1 is the time of the π-pulse on the electron and λ, κ are the additional phases on $|00\rangle$ and $|01\rangle$.

Phase calibration

We can eliminate the undesired phases before the teleportation experiment by calibrating the rotation axis of the $\pi/2$ operation on the nitrogen in the BSM and the evolution times. After initializing the nitrogen and electron spin states of Alice into $|1\rangle\,(|0\rangle - |1\rangle)/\sqrt{2}$ (equivalent to the entanglement operation on Alice, ignoring Bob), we prepare the nitrogen in $|\bar{x}\rangle = (|0\rangle - |1\rangle)/\sqrt{2}$ (preparation operation is y) and

perform the BSM, yielding

$$\frac{1}{2\sqrt{2}}\Big[\,|00\rangle\left(-1-\mathrm{e}^{\mathrm{i}\lambda}\right) + |01\rangle\left(-1+\mathrm{e}^{-\mathrm{i}A(t_1-t_0)-\mathrm{i}\kappa}\right) + |10\rangle\left(1-\mathrm{e}^{\mathrm{i}\lambda}\right) + |11\rangle\left(1+\mathrm{e}^{-\mathrm{i}A(t_1-t_0)-\mathrm{i}\kappa}\right)\Big] \tag{4.6}$$

before readout (Fig. 4.8). We sweep the rotation axis of the RF pulse on the nitrogen (affecting the phase $\mathrm{i}\lambda$) and subsequently the evolution time between the CNOT and Y operations during the BSM (affecting the phase $-\mathrm{i}A(t_1-t_0)-\mathrm{i}\kappa$). Calibration is achieved by maximizing the probabilities for outcomes $|00\rangle$ and $|11\rangle$.

Dynamical decoupling of Bob's electron spin

To protect the target state against dephasing during the BSM, we perform an XY4 decoupling sequence in parallel. The first π-pulse of this echo sequence is the π-pulse performed during the entanglement generation attempt. The remaining X-Y-X sequence is executed during the BSM. Taking these additional rotations into account, the total state before readout, including phase calibration, is

$$\frac{1}{2}\Big[\,|00\rangle\left(\alpha\,|0\rangle+\beta\,|1\rangle\right) + |01\rangle\left(-\beta\,|0\rangle+\alpha\,|1\rangle\right) + |10\rangle\left(\alpha\,|0\rangle-\beta\,|1\rangle\right) + |11\rangle\left(\beta\,|0\rangle+\alpha\,|1\rangle\right)\Big]. \tag{4.7}$$

Because we do not intialize the nuclear spin on Bob's side we perform all electron spin rotations with CORPSE pulses[24].

Feed-forward

The required feed-forward operations to re-create $|\psi\rangle$ on the target spin can be taken straight-forward from Eq. 4.7. For the estimation of the fidelity of the teleported state with the ideal source state it is sufficient to read out in the basis aligned with the source state vector. We achieve this readout by modifying the feed-forward operation such that we rotate the target state $U_{i,j}\,|\psi\rangle$ directly into the z-basis, conditional on the outcome of the BSM. The operations we apply in practice are summarized in Table 4.1.

4.5.3 Data analysis

For each input state we determine the number of events n_0 and n_1 that give measurement outcomes $m_s = 0$ and $m_s = -1$, respectively. The probability amplitudes c_0 and c_1 for $|0\rangle$ and $|1\rangle$ are obtained by performing readout correction using the readout fidelities F_0 and F_{-1} for $m_s = 0$ and $m_s = -1$, respectively. We obtain F_0 and F_{-1} from calibration measurements performed periodically during the experiment. The teleportation fidelity of the state is given by either c_0 or c_1 (see Table 4.1).

The uncertainty of c_0 and c_1 is determined by the standard deviation of the binomial distribution with probabilities $n_0/(n_0 + n_1)$ and $n_1/(n_0 + n_1) = 1 - n_0/(n_0 + n_1)$, and the measurement uncertainties of F_0 and F_{-1} (for both readout fidelities the measurement uncertainties are ≈ 0.005).

4.5.4 Error model

In the following we describe the errors we take into account for modelling our experimental results. Any further errors are considered small in comparison and we ignore them in this discussion. In particular we assume that the preparation of the source state $|\psi\rangle$ is not subject to errors resulting from RF or microwave pulses.

Note that we model the experimental results numerically with the best guesses of the empiric parameters described below, without treatment of their uncertainties.

In general we simulate the experimental results by modelling the system by a $2 \times 2 \times 2$ dimensional density matrix that is subjected to operators that correspond to the operations physically applied. Treatment of errors is included in the description of the types of errors taken into consideration in the following. Operations for which no error is listed are assumed to be perfect.

CNOT pulses

The fidelity of Alice's electron spin rotations that are selective on the ^{14}N spin state are limited by the finite linewidth of the electron spin transitions. We simulate the effect of the pulse on the different hyperfine populations by evaluating the probability for inversion versus detuning using a master equation solver[25], and integrating over the transition line shapes. In this way we compute the probabilities for an erroneous inversion for $m_I = -1$ and non-inversion for $m_I = 0$ to be both 0.01. Our calculation is based on a finite linewidth that is determined by the electron spin dephasing time, $T_2^* = 2\,\mu$s. In our model we assume that in case of an error the spin state is dephased (i.e., we numerically set the respective coherences in the resulting density matrix to zero).

Nuclear spin initialization

When preparing the source state to be teleported, the following errors can occur: (1) Initialization by measurement into $m_I = -1$ succeeds with a fidelity p_{-1}, and fails for the initial state in either $m_I = 0$ or $m_I = +1$, with probabilities p_0 and p_{+1}, respectively; (2) After each failed attempt to generate entanglement between Alice and Bob the electron is reset by optical spin-pumping[26]. During this reset to $m_s = 0$ the nuclear spin can flip — with $\Delta m_I = \pm 1$ — with a probability p_{flip}[27].

Assuming that the conditional probability for a nuclear spin flop accompanying an electron spin flip, p_{flip}, is identical for all $\Delta m_I = \pm 1$, the equations describing the changes of populations in dependence of the number of electron spin flips, n, are

$$\begin{aligned} p_{-1}(n) - p_{-1}(n-1) &= p_{\text{flip}}\,(p_0(n-1) - p_{-1}(n-1)) \\ p_0(n) - p_0(n-1) &= p_{\text{flip}}\,(-2p_0(n-1) + p_{-1}(n-1) + p_{+1}(n-1)) \\ p_{+1}(n) - p_{+1}(n-1) &= p_{\text{flip}}\,(p_0(n-1) - p_{+1}(n-1))\,. \end{aligned} \tag{4.8}$$

The measured population of $m_I = -1$ as a function of n is shown in Fig. 4.9.

From independent calibration measurements we estimate the nuclear spin to be initialized by measurement with $p_{-1}(0) = 0.97$, $p_0(0) = 0.02$, and $p_{+1}(0) = 0.01$. Together with the nuclear spin depolarization during subsequent entanglement generation attempts we determine $\langle p_{-1}\rangle = 0.88$, $\langle p_0\rangle = 0.10$, and $\langle p_{+1}\rangle = 0.02$ from the solution of (4.8), for a maximum of 250 entanglement generation attempts before re-initialization by measurement. Here,

$$\langle p_i\rangle = \frac{1}{N}\sum_{n=0}^{N} p_i(n) \tag{4.9}$$

is the average population of the nuclear spin state i for a maximum of 2N entanglement generation attempts. Note that the electron spin is in a superposition before reset, and thus the number of spin flips is half the number of entanglement generation attempts. The probability for successful entanglement generation is independent of the attempt number.

In the simulation of the experimental data we calculate the projected outcomes for each of the nuclear spin states and determine the combined result by weighing the average with $\langle p_{-1}\rangle$, $\langle p_0\rangle$, and $\langle p_{+1}\rangle$. Because population in $m_I = +1$ is outside the simulated space of two-level systems we treat this case in a separate simulation before weighing. The net effect of detuned MW pulses in this case is determined by calculating the electron spin rotation versus detuning and integrating over the $m_I = +1$ transition line shape.

The influence of imperfect nuclear spin initialization can also be approximated inituitively as follows: for $m_{\mathrm{I}} = +1$ none of the operations on Alice's side are performed since all pulses applied are off-resonant, leading to dephasing of the state and ultimately a fully random outcome of Bob's readout. Initialization in $m_{\mathrm{I}} = 0 \equiv |0\rangle$ results in the opposite outcome than the one obtained from correct intialization in $m_{\mathrm{I}} = -1 \equiv |1\rangle$. Thus, with probability $2\langle p_0\rangle + \langle p_{+1}\rangle$ the target state is fully mixed.

Readout

The major limitation of the Bell-state measurement fidelity is the finite single-shot readout fidelity of both electron and nuclear spin on Alice's side. Electron spin readout is achieved by resonant optical excitation of E_y. Detection of a least one photon during this interval is registered as readout result $m_{\mathrm{s}} = 0$, otherwise the result is $m_{\mathrm{s}} = \pm 1$. Nuclear spin readout is achieved by re-setting the electron spin to $m_{\mathrm{s}} = 0$, mapping the nuclear spin state onto the electron spin by a CNOT, and reading out the electron spin. This procedure is performed twice in order to maximize the readout fidelity[28]. Readout result $m_{\mathrm{I}} = 0$ is obtained for detection of at least one photon during either round.

The electron spin readout is limited by finite photon collection efficiency and electron spin mixing in the excited state[28]. For Alice, we measure a mean single-shot readout fidelity of $F_{\text{e-RO}} = 0.963 \pm 0.005$. The nuclear spin readout is additionally limited by the CNOT fidelity. With two readout rounds we estimate a mean readout fidelity of $F_{\text{N-RO}} = 0.985$ from the electron spin readout and CNOT pulse simulations.

In the simulation of the experimental results we use the single-shot readout fidelities to determine the conditional density matrices that arise after measuring the electronic and nuclear spin.

Photon indistinguishability and entangled state fidelity

The entangled state between the two electronic spins can be modeled as

$$\rho = V|\Psi^-\rangle\langle\Psi^-| + \frac{(1-V)}{2}\left(|01\rangle\langle 01| + |10\rangle\langle 10|\right), \tag{4.10}$$

where the visibility V describes the distinguishability between the photons emitted from Alice and Bob. Here we assume that all other imperfections are negligible compared to the photon distinguishability. The limitations of the Bell state fidelity are discussed in detail in Bernien *et al.*[26]

For modelling we treat V as a free parameter used to match the average teleportation fidelity. Using the parameters as described above and setting $V = 0.74$ (corresponding to a Bell-state fidelity of $F_{\Psi^-} = 0.87$) our simulation yields a mean teleportation fidelity of $F = 0.77$.

4.5.5 Further analysis of the teleporter performance

Effect of the feed-forward operation

Fig. 4.4B shows the teleportation fidelity when no feed-forward is performed. This data is extracted from the teleportation data including feed-forward in the following way. We first determine the probability for obtaining the expected readout result independently for each BSM outcome by postselection. We then invert the readout result for all operations with a negative rotation sense. In this way we obtain the result that would have been measured if for each BSM outcome the same qubit rotation was performed (i.e., no feed-forward). We assume that any experimental errors in the final readout pulse are small and thus neglect them in this treatment.

Correction for intialization

After determining the entangled state fidelity as described above we can estimate the actual teleportation fidelity by assuming perfect intialization in our simulation. Setting $p_{-1} = 1$ we compute a mean teleportation fidelity of $F_{\text{corrected}} = 0.86$ (Fig. 4.10A).

Teleportation fidelity by Bell-state measurement outcome

Due to the different readout fidelities for each of the four Bell states (see above and Fig. 4.3) we can expect different teleportation fidelities as well. We find that the teleportation fidelity by outcome of the Bell-state measurement is consistent with expectations (Fig. 4.10B), but the statistical uncertainty prevents a more detailed discussion.

Probability of BSM outcomes

We verify in more detail that the teleportation works as intended by examining the distribution of BSM outcomes obtained from all teleportation events (Fig. 4.10C). The simulations are in good agreement with the data. The deviation from an equal probability of 0.25 for all BSM outcomes is mainly due to the asymmetry in the readout fidelities of the electron spin states[28].

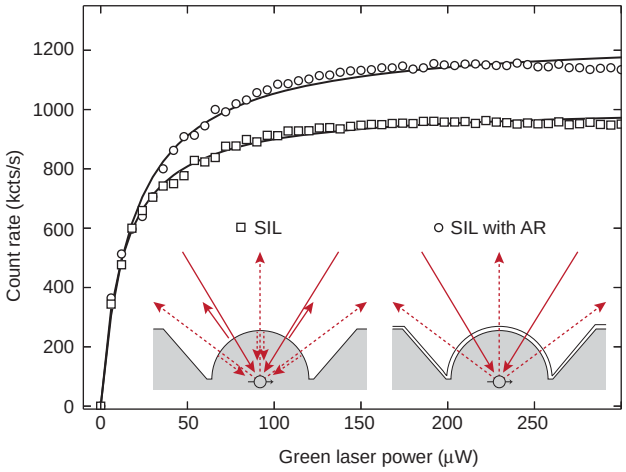

Figure 4.5 — Saturation measurements on SILs with and without antireflection coating. Fluorescence count rates as a function of off-resonant green excitation power (kcts = 1000 counts). Solid lines are fits to $A \cdot x/(x + P_{\text{sat}})$. In the case of a bare SIL, photons emitted from the NV centre and the excitation laser can be reflected at the interface due to the large refractive index of diamond. This effect is overcome by an antireflection coating which further increases the count rates and significantly reduces reflections of the excitation laser.

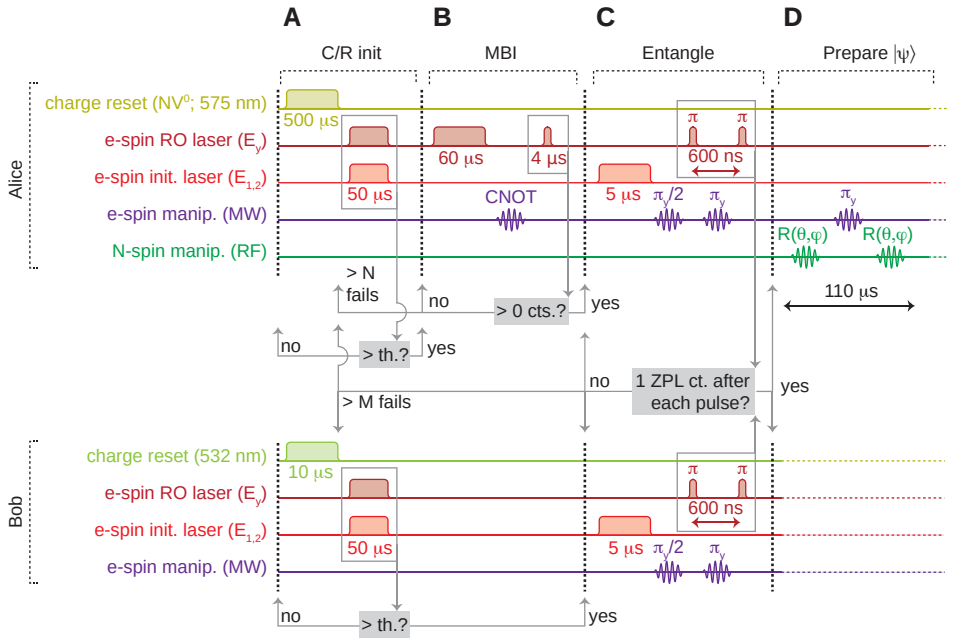

Figure 4.6 — System initialization. **A,** We verify charge and resonance condition of Alice and Bob (asynchronously) by applying laser pulses on E_y and $E_{1,2}$ simultaneously and putting a lower threshold on the number of phonon side band photons detected during those pulses. If the threshold is not met we reset the charge state: On Alice, we repump $NV^0 \rightarrow NV^-$ using a laser at 575 nm, on resonance with the ZPL of NV^0 [29]. On Bob, we use off-resonant excitation at 532 nm. We repeat verification and repump until success. **B,** Following spin-pumping into $m_s = \pm 1$ by excitation of E_y we apply a CNOT on the electronic spin, such that rotation to $m_s = 0$ is only performed for $m_I = -1$. A PSB photon detected during a short readout pulse on E_y signals a high-fidelity measurement of $m_s = 0$ and projection of the nuclear spin into $m_I = -1$. If no photon is detected, we re-try for a maximum of N times (here, $N = 100$), before charge and resonance are re-evalutated. In between attempts we apply $50\,\mu s$ of illumination on both E_y and $E_{1,2}$ in order to randomise the nuclear spin owed to off-diagonal terms in the hyperfine interaction in the optical excited state (not shown in the diagram). **C,** As soon as both Alice and Bob are initialised, we attempt to generate entanglement between them. Each attempt starts with an electron spin reset to $m_s = 0$. Two rounds of optical excitation with optical π-pulses on E_y follow, separated by a MW π-pulse. Detection of exactly one ZPL photon after each pulse heralds creation of entanglement. We perform a maximum of M attempts before re-initialisation (here, $M = 250$). **D,** When entanglement is created, we prepare the ^{14}N spin of Alice unconditional on the electron spin state, while preserving the electron spin phase. The RF pulse that generates the rotation is only resonant for $m_s = -1$; we perform the rotation twice, separated by a π-pulse on the electron.

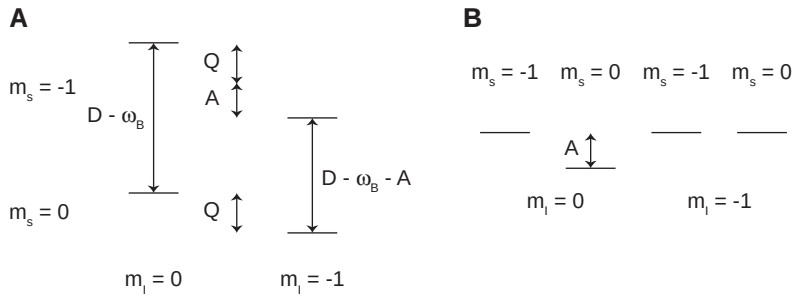

Figure 4.7 — Relevant spin states on Alice's side. **A,** Lab frame. **B,** Rotating frame chosen. $D = 2\pi \times 2.878$ GHz is the NV electron zero-field splitting, $\omega_{\mathrm{B}} \approx 2\pi \times 50$ MHz is the Zeeman splitting of the electron, $A = 2\pi \times 2.19$ MHz is the electron-nitrogen hyperfine coupling constant and $Q = 4.98$ MHz the nitrogen quadrupole splitting.

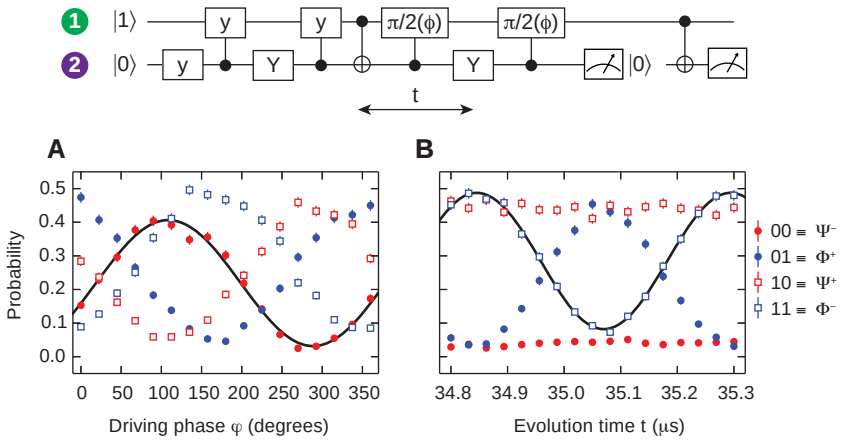

Figure 4.8 — Calibration of the Bell-state measurement. **A,** Calibration of the driving phase of the Hadamard operation, and **B,** subsequent calibration of the evolution time between the CNOT gate of the BSM and the electron π-pulse for the unconditional rotation of the nuclear spin. The solid lines are sinosoidal fits to the BSM outcomes to be maximised. The legend indicates the correspondence between two-qubit measurement results ij and Bell-state detection. The calibration is performed with the full teleportation protocol including the MW pulses during entanglement generation attempts (but without optical π-pulses). Error bars are 1 s.d.

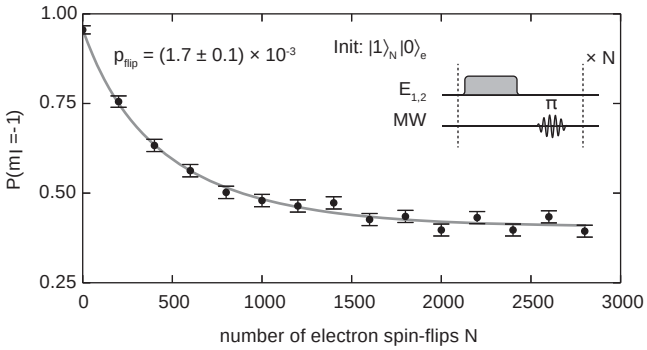

Figure 4.9 — Nuclear spin state depolarization as function of electron spin flips by optical spin-pumping. We measure nuclear spin flips that are conditional on electron spin flips when optically pumping on $E_{1,2}$. We prepare the nuclear spin in $m_{\rm s} = -1$ and measure the probability for its preservation dependent on the number of cycles of electron spin-pumping $|1\rangle \rightarrow |0\rangle$ and re-preparation of $|1\rangle$ by a microwave π-pulse. The solid line is a fit to the solution of (4.8) that is given by $p_{-1}(n) = 1/6\left(2 + (1-3p_{\rm flip})^N + 3(1-p_{\rm flip})^N\right)$ (neglecting initial population in $m_{\rm I} = 0$ and $m_{\rm I} = +1$). Because the data shown here is not corrected for finite initialisation fidelity of the nuclear spin and nuclear spin readout errors we include an offset o and scaling factor A in the fit function, $p_{-1}(n) = A/6\left(2 + (1-3p_{\rm flip})^N + 3(1-p_{\rm flip})^N\right) + o$. The fit yields a nuclear spin-flip probability of $p_{\rm flip} = (0.17 \pm 0.01)\,\%$ per spin pumping cycle, and $A = 0.83 \pm 0.02$, $o = 0.13 \pm 0.01$. Note that the data shown in Fig. 4.2D has been corrected for nuclear spin readout errors. Error bars are 1 s.d.

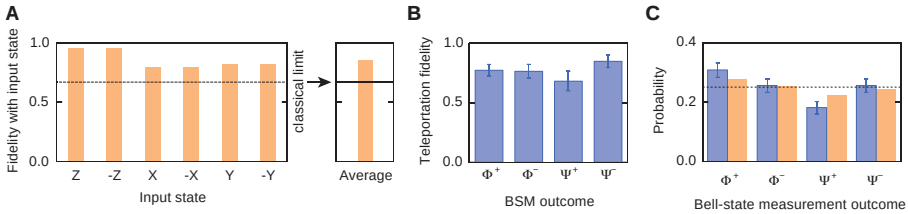

Figure 4.10 — Further analysis of the teleportation fidelity. **A,** Correction for imperfect initialization of the source qubit. We simulate the teleportation outcomes using perfect intialization, $p_{-1} = 1$. The simulation yields and average fidelity of 0.86. **B,** We determine the average teleportation fidelity for each outcome of the Bell-state measurement. Within the statistical uncertainty the fidelities do not differ substantially. **C,** Probability for each BSM outcome, as measured (blue) and predicted from the model (orange). The dashed line marks 0.25. Error bars are 1 s.d.

Table 4.1 — Feed-forward and readout operations applied for each BSM outcome.

Input	$\|00\rangle$	$\|01\rangle$	$\|10\rangle$	$\|11\rangle$	ideal result
$\|+z\rangle = Y\|1\rangle$	$\mathbb{1}$	Y	$\mathbb{1}$	Y	$\|0\rangle$
$\|-z\rangle = \mathbb{1}\|1\rangle$	Y	$\mathbb{1}$	Y	$\mathbb{1}$	$\|0\rangle$
$\|+x\rangle = \bar{y}\|1\rangle$	$\bar{y}$	y	y	$\bar{y}$	$\|0\rangle$
$\|-x\rangle = y\|1\rangle$	y	$\bar{y}$	$\bar{y}$	y	$\|0\rangle$
$\|+y\rangle = \bar{x}\|1\rangle$	$\bar{x}$	$\bar{x}$	x	x	$\|1\rangle$
$\|-y\rangle = x\|1\rangle$	x	x	$\bar{x}$	$\bar{x}$	$\|1\rangle$

4.6 Bibliography

[1] S. Olmschenk *et al.* Quantum teleportation between distant matter qubits. *Science* **323**, 486 (2009).

[2] C. Nölleke *et al.* Efficient teleportation between remote single-atom quantum memories. *Physical Review Letters* **110**, 140403 (2013).

[3] H. Krauter *et al.* Deterministic quantum teleportation between distant atomic objects. *Nature Physics* **9**, 400 (2013).

[4] D. D. Awschalom, L. C. Bassett, A. S. Dzurak, E. L. Hu and J. R. Petta. Quantum spintronics: Engineering and manipulating atom-like spins in semiconductors. *Science* **339**, 1174 (2013).

[5] M. H. Devoret and R. J. Schoelkopf. Superconducting circuits for quantum information: An outlook. *Science* **339**, 1169 (2013).

[6] C. Monroe and J. Kim. Scaling the ion trap quantum processor. *Science* **339**, 1164 (2013).

[7] M. Riebe *et al.* Deterministic quantum teleportation with atoms. *Nature* **429**, 734 (2004).

[8] M. D. Barrett *et al.* Deterministic quantum teleportation of atomic qubits. *Nature* **429**, 737 (2004).

[9] L. Steffen *et al.* Deterministic quantum teleportation with feed-forward in a solid state system. *Nature* **500**, 319 (2013).

[10] P. Siyushev *et al.* Optically controlled switching of the charge state of a single nitrogen-vacancy center in diamond at cryogenic temperatures. *Physical Review Letters* **110**, 167402 (2013).

[11] L. Robledo *et al.* High-fidelity projective read-out of a solid-state spin quantum register. *Nature* **477**, 574 (2011).

[12] L. Jiang *et al.* Coherence of an optically illuminated single nuclear spin qubit. *Physical Review Letters* **100**, 073001 (2008).

[13] M. S. Blok *et al.* Manipulating a qubit through the backaction of sequential partial measurements and real-time feedback. *Nature Physics* **10**, 189 (2014).

[14] T. van der Sar *et al.* Decoherence-protected quantum gates for a hybrid solid-state spin register. *Nature* **484**, 82 (2012).

[15] G. d. Lange, Z. H. Wang, D. Ristè, V. V. Dobrovitski and R. Hanson. Universal dynamical decoupling of a single solid-state spin from a spin bath. *Science* **330**, 60 (2010).

[16] H.-J. Briegel, W. Dür, J. I. Cirac and P. Zoller. Quantum repeaters: The role of imperfect local operations in quantum communication. *Physical Review Letters* **81**, 5932 (1998).

[17] T. H. Taminiau *et al.* Detection and control of individual nuclear spins using a weakly coupled electron spin. *Physical Review Letters* **109**, 137602 (2012).

[18] S. Kolkowitz, Q. P. Unterreithmeier, S. D. Bennett and M. D. Lukin. Sensing distant nuclear spins with a single electron spin. *Physical Review Letters* **109**, 137601 (2012).

[19] N. Zhao *et al.* Sensing single remote nuclear spins. *Nature Nanotechnology* **7**, 657 (2012).

[20] T. H. Taminiau, J. Cramer, T. v. d. Sar, V. V. Dobrovitski and R. Hanson. Universal control and error correction in multi-qubit spin registers in diamond. *Nature Nanotechnology* **9**, 171 (2014).

[21] P. C. Maurer *et al.* Room-temperature quantum bit memory exceeding one second. *Science* **336**, 1283 (2012).

[22] M. Lončar and A. Faraon. Quantum photonic networks in diamond. *MRS Bulletin* **38**, 144 (2013).

[23] N. Brunner, D. Cavalcanti, S. Pironio, V. Scarani and S. Wehner. Bell nonlocality. *Reviews of Modern Physics* **86**, 419 (2014).

[24] H. K. Cummins, G. Llewellyn and J. A. Jones. Tackling systematic errors in quantum logic gates with composite rotations. *Phys. Rev. A* **67**, 42308 (2003).

[25] J. R. Johansson, P. D. Nation and F. Nori. QuTiP 2: A Python framework for the dynamics of open quantum systems. *Computer Physics Communications* **184**, 1234 (2013).

[26] H. Bernien *et al.* Heralded entanglement between solid-state qubits separated by three metres. *Nature* **497**, 86 (2013).

[27] P. Neumann *et al.* Single-Shot Readout of a Single Nuclear Spin. *Science* **329**, 542 (2010).

[28] L. Robledo *et al.* High-fidelity projective read-out of a solid-state spin quantum register. *Nature* **477**, 574 (2011).

[29] P. Siyushev *et al.* Optically Controlled Switching of the Charge State of a Single Nitrogen-Vacancy Center in Diamond at Cryogenic Temperatures. *Phys. Rev. Lett.* **110**, 167402 (2013).

Chapter 5

Loophole-free violation of a Bell inequality using entangled spins separated by 1.3 km

B. Hensen, H. Bernien, A.E. Dréau, A. Reiserer, N. Kalb, M.S. Blok, J. Ruitenberg, R.F.L. Vermeulen, R.N. Schouten, C. Abellán, W. Amaya, V. Pruneri, M.W. Mitchell, M. Markham, D.J. Twitchen, D. Elkouss, S. Wehner, T.H. Taminiau and R. Hanson,

For more than 80 years, the counterintuitive predictions of quantum theory have stimulated debate about the nature of reality[1]. In his seminal work[2], John Bell proved that no theory of nature that obeys locality and realism[1] can reproduce all the predictions of quantum theory: in any local-realist theory, the correlations between outcomes of measurements on distant particles satisfy an inequality that can be violated if the particles are entangled. In the past decades, numerous ingenious Bell inequality tests have been reported[3–14]. However, because of experimental limitations, all experiments so far required additional assumptions to obtain a contradiction with local realism, resulting in loopholes[15–18]. Here we report on a Bell experiment that is free of any such additional assumptions and thus directly tests the principles underlying Bell's inequality. We employ an event-ready scheme[19–21] that enables the generation of high-fidelity entanglement between distant electron spins. Efficient spin readout avoids the fair sampling assumption[16,17], while the use of fast random basis selection and readout combined with a spatial separation of 1.3 kilometres ensure the required locality conditions[15]. In two experimental tests we find strong evidence against the null-hypothesis that a local-realist model for space-like separated sites could produce data with a violation at least as large as we observe, even when allowing for memory[18,22] in the devices. With improvements, our experiment could be used for testing less-conventional theories, and for implementing device independent quantum-secure communication[23] and randomness certification[24,25].

Part of the results in this chapter have been published in *Nature* **526**, 682 (2015).

5.1 Introduction

We consider a Bell test in the form proposed by Clauser, Horne, Shimony and Holt (CHSH)[26] (Fig. 5.1a). The test involves two boxes labelled A and B. Each box accepts a binary input (0 or 1) and subsequently delivers a binary output (+1 or −1). In each trial of the Bell test, a random input bit is generated on each side and input to the respective box. The random input bit triggers the box to produce an output value that is recorded. The test concerns correlations between the output values (labelled x and y for boxes A and B, respectively) and the input bits (labelled a and b for A and B, respectively) generated within the same trial.

The discovery made by Bell is that in any theory of physics that is both local (physical influences do not propagate faster than light) and realistic (physical properties are defined before, and independent of, observation) these correlations are bounded more strongly than they are in quantum theory. In particular, if the input bits can be considered free random variables (condition of "free will") and the boxes are sufficiently separated such that locality prevents communication between the boxes during a trial, then the following inequality holds under local realism:

$$S = \langle x \cdot y \rangle_{(0,0)} + \langle x \cdot y \rangle_{(0,1)} + \langle x \cdot y \rangle_{(1,0)} - \langle x \cdot y \rangle_{(1,1)} \leq 2 \tag{5.1}$$

where $\langle x \cdot y \rangle_{(a,b)}$ denotes the expectation value of the product of x and y for input bits a and b (see also Sec. 1.2.2 and Bell[27]).

Quantum theory predicts that the Bell inequality can be significantly violated in the following setting. We add one particle, for example an electron, to each box. The spin degree of freedom of the electron forms a two-level system with eigenstates $|\uparrow\rangle$ and $|\downarrow\rangle$. For each trial, the two spins are prepared into the entangled state $|\psi^-\rangle = (|\uparrow\downarrow\rangle - |\downarrow\uparrow\rangle)/\sqrt{2}$. The spin in box A is then measured along direction Z (for input bit $a = 0$) or X (for $a = 1$) and the spin in box B is measured along $(-\mathrm{Z}+\mathrm{X})/\sqrt{2}$ (for $b = 0$) or $(-\mathrm{Z}-\mathrm{X})/\sqrt{2}$ (for $b = 1$). If the measurement outcomes are used as outputs of the boxes, then quantum theory predicts a value of $S = 2\sqrt{2}$, which shows that the combination of locality and realism is fundamentally incompatible with the predictions of quantum mechanics.

Bell's inequality provides a powerful recipe for probing fundamental properties of nature: all local-realist theories that specify where and when the free random input bits and the output values are generated can be experimentally tested against it.

Violating Bell's inequality with entangled particles poses two main challenges: excluding any possible communication between the boxes (locality loophole[15]) and guaranteeing efficient measurements (detection loophole[16,17]). First, if communication is possible, a box can in principle respond using knowledge of *both* input settings, rendering the Bell inequality invalid. The locality conditions thus require boxes A and B and their respective free-input-bit generations to be separated in such a way that

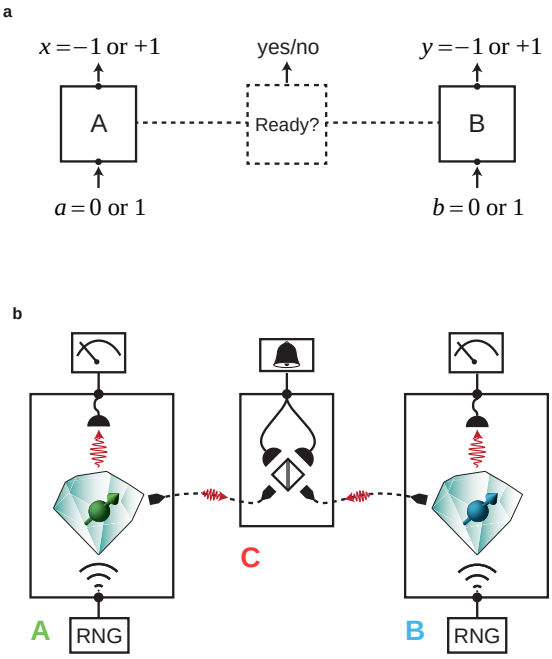

Figure 5.1 — Bell test schematic (a) Bell test setup: Two boxes, A and B, accept binary inputs (a, b) and produce binary outputs (x, y). In an event-ready scenario, an additional box C gives a binary output signalling that A and B were successfully prepared. **(b)** Experimental realisation. The setup consists of three separate laboratories, A, B and C. The boxes at locations A and B each contain a single NV centre in diamond. A quantum random number generator (RNG) is used to provide the input. The NV electronic spin is read out in a basis that depends on the input bit, and the resultant signal provides the output. A third box at location C records the arrival of single photons that were previously emitted by, and are entangled with, the spins at A and B. The detection of two such photons constitutes the event-ready signal.

signals travelling at the speed of light (the maximum allowed under special relativity) cannot communicate the local input setting of box A to box B, before the output value of box B has been recorded, and vice versa*. Second, disregarding trials in which a box does not produce an output bit (that is, assuming fair sampling) would allow the boxes to select trials based on the input setting. The fair sampling assumption thus opens a detection loophole: the selected subset of trials may show a violation even though the set of all trials may not.

The locality loophole has been addressed with pairs of photons separated over a large enough distance in combination with fast settings changes[4] and later with settings determined by fast random number generators[6,10]. However, these experiments left open the detection loophole, owing to imperfect detectors and inevitable photon loss during the spatial distribution of entanglement. The detection loophole has been closed in different experiments[7–9,11,13,14], but these did not close the locality loophole. So far, no experiment has closed all the loopholes simultaneously.

A Bell test that closes all experimental loopholes at the same time - commonly referred to as a loophole-free Bell test[17,21,28] is of foundational importance to the understanding of nature. In addition, a loophole-free Bell test is a critical component for device-independent quantum security protocols[23] and randomness certification[24,25]. In such adversarial scenarios, all loopholes are ideally closed because they allow for security breaches in the system[29].

An elegant approach for realizing a loophole-free setup was proposed by Bell himself[19]. The key idea is to record an additional signal (dashed box in Fig. 5.1a) to indicate whether the required entangled state was successfully shared between A and B, that is, whether the boxes were ready to be used for a trial of the Bell test. By conditioning the validity of a Bell-test trial on this event-ready signal, failed entanglement distribution events are excluded upfront from being used in the Bell test.

5.2 Implementation

We implemented an event-ready Bell setup[11,20,21] with boxes that use the electronic spin associated with a single nitrogen-vacancy (NV) defect centre in a diamond chip (Fig. 5.1b). The diamond chips are mounted in closed-cycle cryostats ($T = 4$K) located in distant laboratories named A and B (Fig. 5.2a). We control the electronic spin state of each NV centre with microwave pulses applied to on-chip striplines (Fig. 5.2a, inset). The spins are initialized through optical pumping and read out along the Z axis via spin-dependent fluorescence[30]. The readout relies on resonant excitation of a spin-selective cycling transition (12 ns lifetime), which causes the NV centre to emit many photons when it is in the bright $m_s = 0$ spin state, while it remains dark when

*Also, the input bits should not be able to influence the preparation of the entangled state.

it is in either of the $m_s = \pm 1$ states. We assign the output value +1 ($m_s = 0$) to the output if we record at least one photo-detector count during the read-out window, and the output value -1 ($m_s = \pm 1$) otherwise. Read-out in a rotated basis is achieved by first rotating the spin, followed by read-out along Z.

We generate entanglement between the two distant spins by entanglement swapping[20] in the Barrett-Kok scheme[31,32] using a third location C (roughly midway between A and B; see Fig. 5.2c). First we entangle each spin with the emission time of a single photon (time-bin encoding). The two photons are then sent to location C, where they are overlapped on a beam-splitter and subsequently detected. If the photons are indistinguishable in all degrees of freedom, then the observation of one early and one late photon in different output ports projects the spins at A and B into the maximally entangled state $|\psi^-\rangle = (|\uparrow\downarrow\rangle - |\downarrow\uparrow\rangle)/\sqrt{2}$, where $m_s = 0 \equiv |\uparrow\rangle$, $m_s = -1 \equiv |\downarrow\rangle$. These detections herald the successful preparation and play the role of the event-ready signal in Bell's proposed setup. As can be seen in the space-time diagram in Fig. 5.3a, we ensure that this event-ready signal is space-like separated from the random input-bit generation at locations A and B.

The separation of the spins by 1280 m defines a 4.27 μs time window during which the local events at A and B are space-like separated from each other (see the space-time diagram in Fig. 5.3b). To comply with the locality conditions of the Bell test, the choice of measurement bases and the measurement of the spins should be performed within this time window. For the basis choice we use fast random-number generators with real-time randomness extraction[33,34]. We reserve 160 ns for the random basis choice, during which time one extremely random bit is generated from 32 partially random raw bits (Sec. 5.9.8). The random bit sets the state of a fast microwave switch that selects one out of two preprogrammed microwave pulses implementing the two possible read-out bases (Fig. 5.2a). Adding the durations of each of the above steps yields a maximum time from the start of the basis choice to the start of the readout of 480 ns. We choose the readout duration to be 3.7 μs, which leaves 90 ns to cover any uncertainty in the distance between the laboratories and the synchronization of the setup (estimated total error is at most 16 ns, see Sec. 5.9.7). For this readout duration, the combined initialisation and single-shot readout fidelity of sample A is $(97.1 \pm 0.2)\%$ (Fig. 5.3c); sample B achieves $(96.3 \pm 0.3)\%$. In summary, the use of the event-ready scheme enables us comply with the strict locality conditions of the Bell setup by using photons to distribute entanglement, while simultaneously using the single-shot nature of the spin read-out to close the detection loophole.

Before running the Bell test we first characterized the setup and the preparation of the spin-spin entangled state. Fig. 5.4a displays correlation measurements on the entangled spin-photon states to be used for the entanglement swapping. For both location A and B we observe near-unity correlations between spin state and photon time bin when spin readout errors are accounted for. We then estimate the degree of indistinguishability[35] of the single photons emitted at locations A and B in a

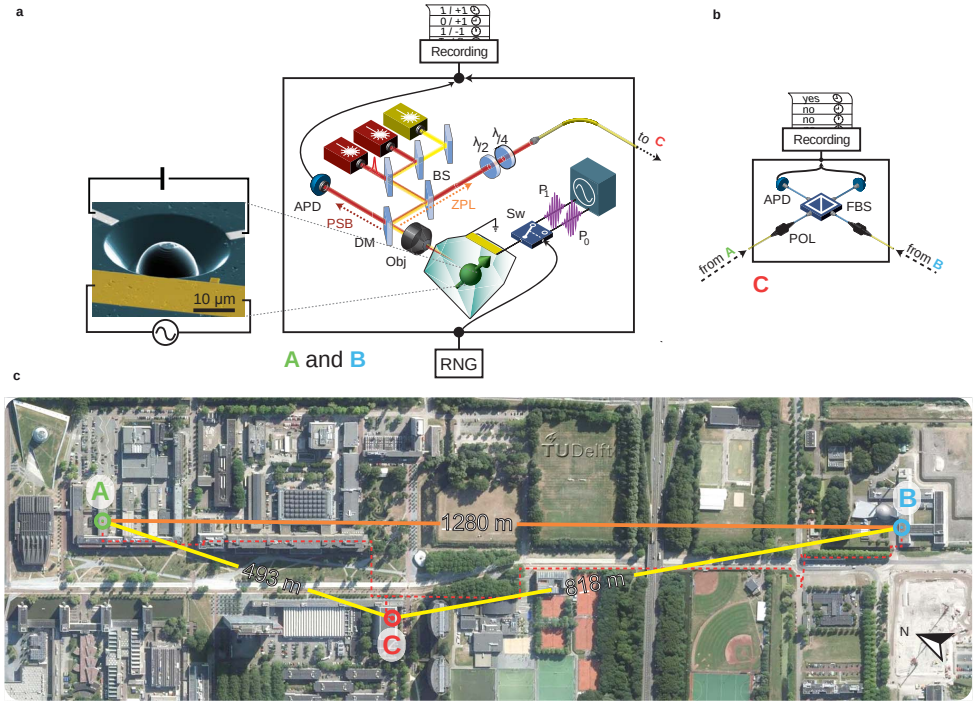

Figure 5.2 — Bell test experimental realisation. (a) Detailed experimental setup at A and B. The NV centre is located in a low temperature confocal microscope setup (Obj). Depending on the output of the RNG, a fast switch (Sw.) transmits one of two different microwave pulses (P_0 and P_1) into a gold line deposited on the diamond surface (inset, scanning electron microscope image). Pulsed red and yellow lasers are used to resonantly excite the optical transitions of the NV centre. The emission (dashed arrows) is spectrally separated into an off-resonant part (phonon side band, PSB) and a resonant part (zero-phonon line, ZPL), using a dichroic mirror (DM). The PSB emission is detected with a single-photon counter (APD). The ZPL emission is transmitted through a beam-sampler (BS, reflection $\leq 4\%$) and two wave plates ($\lambda/2$ and $\lambda/4$), and sent to location C through a single-mode fibre. **(b)** Setup at location C. The fibres from A and B are connected to a fibre-based beam splitter (FBS) after passing a fibre-based polarizer (POL). Photons in the two output ports are detected using single photon counters, and detection events are recorded. **(c)** Aerial photograph of the campus of Delft University of Technology indicating the distances between locations A, B and C. The red dotted line marks the path of the fibre connection.

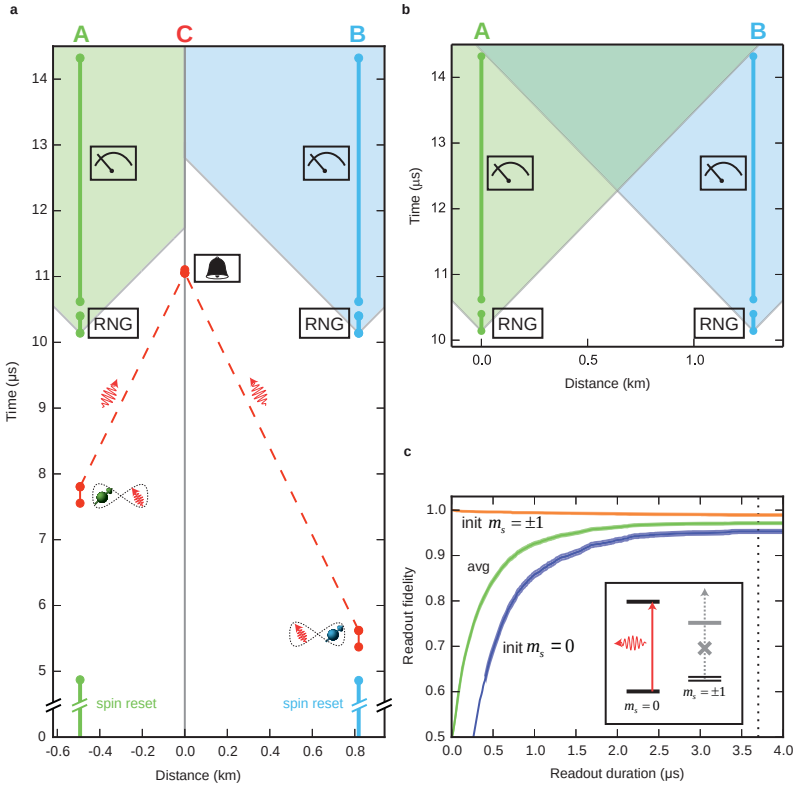

Figure 5.3 — Space-time analysis of the experiment. **(a)** Space-time diagram of a single repetition of the entanglement generation. The x-axis denotes the distance along the lines A-C and C-B. After spin initialization, spin-photon entanglement is generated, such that the two photons from A and B arrive simultaneously at C where the detection time of the photons is recorded. Successful preparation of the spins is signalled (bell symbol) by a specific coincidence detection pattern. Independent of the event-ready signal, the setups at locations A and B choose a random basis (RNG symbol), rotate the spin accordingly and start the optical spin-readout (measurement symbol). Vertical bars indicate the durations. The event-ready signal lies outside the future light cone (coloured regions) of the random basis choices of A and B (see main text for details). **(b)** Space-time diagram of the Bell test. The x-axis denotes the distance along the line A-B. The readout on each side is completed before any light-speed signal can communicate the basis choice from the other side. The uncertainty in the depicted event times and locations is much smaller than the symbol size. **(c)** Single-shot spin readout fidelity at location A as a function of readout duration (set by the latest time that detection events are taken into account). Blue (orange) line, fidelity of outcome $+1$ (-1) when the spin is prepared in $m_s = 0$. ($m_s = \pm 1$); green line, average readout fidelity; dotted line, Readout duration used (3.7 μs). The inset shows the relevant ground and excited-state levels (not to scale).

Hong-Ou-Mandel[36] two-photon interference experiment at location C, that is, after the photons have travelled through a combined length of 1.7 km of single-mode optical fiber. Using the observed two-photon interference contrast of 0.90 ± 0.06 and the spin-photon correlation data we estimate that the fidelity to the ideal state $|\psi^-\rangle$ of the spin-spin entangled states generated in our setup is 0.92 ± 0.03 (Sec. 5.9.3). Combined with measured readout fidelities the generated entangled state is thus expected to violate the CHSH-Bell inequality with $S = 2.28 \pm 0.08$.

As a final characterization we ran the full Bell sequence including random-number generation and fast readout, but with co-linear measurement bases (ZZ and XX) such that spin-spin correlations could be observed with optimal contrast. To test the fast basis selection and rotation, the Z (X) basis measurements are randomly performed along the +Z (+X) and −Z (−X) axis. The observed correlations, shown in Fig. 5.4c (orange bars), are consistent with the estimated quantum state and the independently measured readout fidelities (dotted bars), which confirms that the setup is performing as expected and that the desired entangled state is generated.

We find a success probability per entanglement generation attempt of about 6.4×10^{-9}, which yields slightly more than one event-ready signal per hour. Compared to our previous heralded entanglement experiments over 3 meter[32] this probability is reduced, mainly owing to additional photon loss (8 dB/km) in the 1.7 km optical fibre. To ensure the required long-term operation, we exploit active stabilization on different relevant timescales via automated feedback loops (Sec. 5.9.9). We note that the distance between the entangled electrons is nearly two orders of magnitude larger than it was in any previous experiment[37] with entangled matter systems.

Using the results of the characterization measurements we determine the optimal readout bases for our Bell test. A numerical optimization yields the following angles for the readout bases with respect to Z: 0 (for $a = 0$), $+1/2\pi$ (for $a = 1$), $-3/4\pi - \epsilon$ (for $b = 0$), $3/4\pi + \epsilon$ (for $b = 1$), with $\epsilon = 0.026\pi$. Adding the small angle ϵ is beneficial because of the stronger correlations in ZZ compared to XX. Furthermore, we use the characterization data to determine the time window for valid photon-detection events at location C to optimally reject reflected laser light and detector dark counts. We choose this window conservatively to optimize the entangled-state fidelity at the cost of a reduced data rate. These settings are then fixed and used throughout the actual Bell test. As a final optimization we replaced the photo-detectors at location C with the best set we had available.

5.3 Results

We ran $n = 245$ trials of the Bell test during a total measurement time of 220 hours over a period of 18 days. Fig. 5.5a summarizes the observed data, from which we find $S = 2.42$ in violation of the CHSH-Bell inequality $S \leq 2$. We quantify the significance of this violation for two different scenarios (see Fig. 5.5b). First, similar

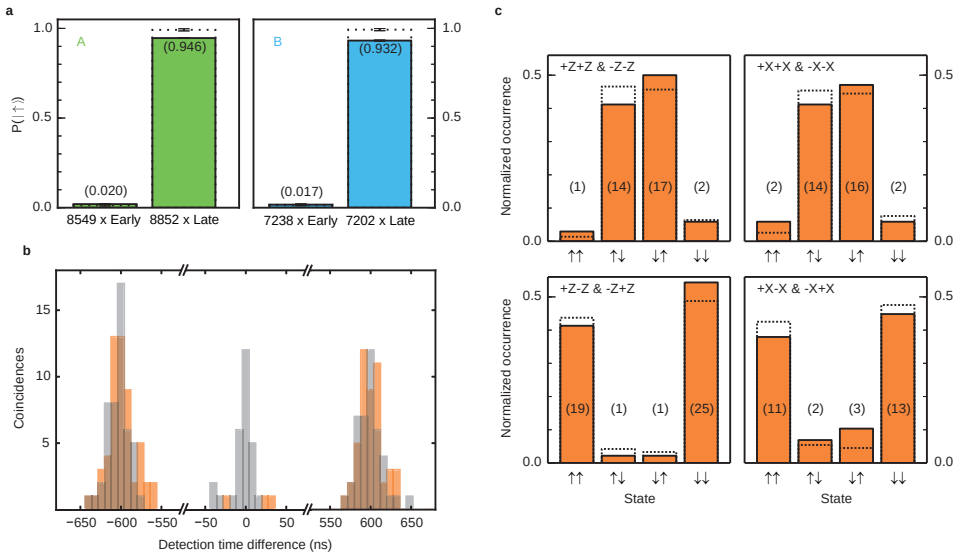

Figure 5.4 — Characterization of the setup and the entangled state. (a) The probability to read out the spin state $|\uparrow\rangle$ at location A (left panel) or B (right panel) when a single photon is detected in the early or late time bin at location C. In the left (right) panel, only emission from A (B) was recorded. Dotted bars are corrected for finite spin read-out fidelity and yield remaining errors of 1.4 ± 0.2 % (1.6 ± 0.2 %) and 0.8 ± 0.4 % (0.7 ± 0.4 %) for early and late detection events, respectively, from setup A (B). These errors include imperfect rejection of the excitation laser pulses, detector dark counts, microwave pulse-errors and off-resonant excitation of the NV. **(b)** Two-photon quantum interference signal. When the NV centres at A and B emit indistinguishable photons (orange), coincident detections of two photons, one in each output arm of the beam-splitter at C, are expected to vanish. The observed contrast between the cases of indistinguishable (orange) and distinguishable (grey) photons (3 versus 28 events in the central peak) yields a visibility of (90 ± 6)% (see Sec. 5.9.2). **(c)** Characterization of the Bell setup using (anti-)parallel read-out angles. The spins at A (left arrows on the x axis) and B (right arrows on the x axis) are read out along the $\pm$Z-axis (left panels), or along the $\pm$X-axis (right panels). Strong correlations (anti-correlations) are observed for the case where the readout axes are anti-parallel, lower panel (parallel, upper panel), as expected for the $|\psi^-\rangle$ state. The numbers in brackets are the raw number of events. The dotted lines represent the expected correlation based on the measured readout fidelity and the characterisation measurements presented in panels a and b (Sec. 5.9.3). Error bars are 1 s.d.

to previous work[4,6–10]., we analyse the data under the assumptions that the Bell trials are independent of each other, that the recorded random input bits have zero predictability and that the outcomes follow a Gaussian distribution. This analysis (which we term "conventional") yields a standard deviation of 0.20 on S. In this case, the null hypothesis that a local-realist model for space-like separated sites describes

our experiment is rejected with a p-value of 0.019.

The assumptions made in the conventional analysis are not justified in a typical Bell experiment. For instance, although the locality conditions outlined earlier are designed to ensure independent operation during a *single* trial, the boxes can in principle have access to the entire history including results from all *previous* trials and adjust their output to it[18,22]. Our second analysis (which we term "complete") allows for arbitrary memory, takes the partial predictability of the random input bits into account and also makes no assumption about the probability distributions underlying the data (Sec. 5.10). In this case, the null hypothesis that an *arbitrary* local-realist model of space-like separated sites governs our experiment is rejected with a p-value of 0.039 (Fig. 5.5b). This P value might be further tightened in future experiments.

5.4 Second run

After finishing the first Bell experiment in July 2015, both the A(lice) and B(ob) setups were modified and used in various local experiments. In December 2015, we rebuilt the Bell setup for performing a second run of the Bell test, with three small modifications compared to the first run:

First, we add a source of classical random numbers for the input choices. A random basis choice is now made by applying an XOR operation between a quantum random bit generated as previously[33,34] and classical random bits based on Twitter messages, as proposed by Pironio[38]. In particular, we generate two sets of classical random numbers, one for the basis choice at A, and one for the basis choice at B (see details in the following sections). At each location, 8 of these bits are fed into an FPGA. Just before the random basis rotation, the 8 Twitter bits and 1 quantum random bit are combined by subsequent XOR operations. The resulting bit is used as the input of the same microwave switch as used in the first run[39]. The XOR operation takes 70 ns of additional time, shifting the start of the readout pulse forward by the same amount. We leave the end of the readout window unchanged, resulting in the same locality conditions as in the first test.

We note that the Twitter-based classical random bits by themselves do not close the locality loophole: the raw data is available on the Internet well before the trials and the protocol to derive the bits is deterministic and programmed locally. The only operations that are performed in a space-like separated manner are the XOR operations between 8 stored bits. Therefore, strictly speaking only the quantum-RNG is providing fresh random bits. Since a loophole-free Bell test is described solely by the random input bit generation and the outcome recording at A and B (and in our case the event-ready signal recording at C), the second run can test the same null hypothesis as the first run as these events are unchanged. That being said, the use of the Twitter-based classical randomness puts an additional constraint on local-hidden-variable models attempting to explain our data.

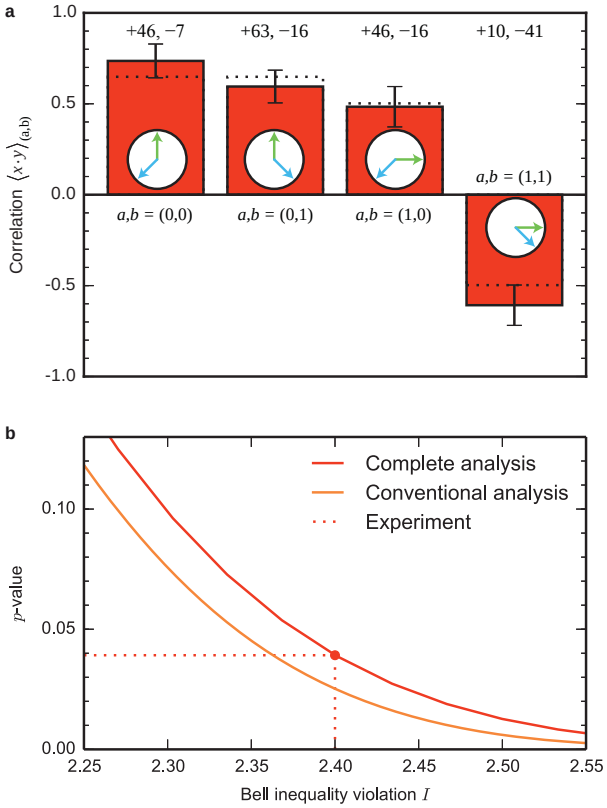

Figure 5.5 — Loophole-free Bell inequality violation. **(a)** Summary of the data and the CHSH correlations. We record a total of $n = 245$ trials of the Bell test. The readout bases corresponding to the input values are indicated by the green (for A) and blue (for B) arrows. Dotted lines indicate the expected correlation on the basis of the spin readout fidelities and the characterization measurements presented in Fig. 5.4 (Sec. 5.9.3). Numbers above the bars represent the number of correlated and anti-correlated outcomes, respectively. Error bars shown are $\sqrt{\left(1 - \langle x \cdot y \rangle^2_{(a,b)}\right)} / n_{(a,b)}$, with $n_{(a,b)}$ the number of events with inputs (a, b). **(b)** Statistical analysis for $n = 245$ trials. We test the null-hypothesis that the data can be explained by any local realist model of space-like separated sites, using an analysis allowing arbitrary memory in the devices and taking the measured imperfections of the random number generators into account (Sec. 5.10). For this analysis, the dependence of the p-value versus the I-value is shown (Complete analysis, red). Here $I := 8(\frac{k}{n} - \frac{1}{2})$, with k the number of times $(-1)^{(a \cdot b)} x \cdot y = 1$. (Note that I equals S from formula (5.1) , for equal $n_{(a,b)}$). A small p-value indicates strong evidence against the null hypothesis. We find $k = 196$, which results in a rejection of the null-hypothesis with a p-value ≤ 0.039. For comparison, we also plot the p-value for an analysis (Conventional analysis, orange) assuming independent and identically distributed (i.i.d.) trials, Gaussian statistics, no memory and perfect random number generators.

Second, we set larger (i.e. less conservative) heralding windows at the event-ready detector in order to increase the data rate compared to the first experiment. We start the heralding window about 700 picoseconds earlier, motivated by the data from the first test (grey line in Fig. 5.7). We predefine a window start of 5426.0 ns after the sync pulse for channel 0, and 5425.1 ns for channel 1. We set a window length of 50 ns.

Finally, we also use the ψ^+- Bell state, which is heralded by two photo-detection events in the *same* beamsplitter output arm at the event-ready station. In general the fidelity of this Bell state is lower than that of ψ^- due to detector after-pulsing[32] (note that for ψ^- the after-pulsing is not relevant because ψ^- is heralded by photo detection events in *different* beamsplitter output arms). However, we found the after-pulsing effect to be small enough for the detectors used in this run. We set an adapted window length of the second window of 4 ns and 2.5 ns for channels 0, 1 respectively, where the exponentially decaying NV emission is still large relative to the after-pulsing probability. As described below, we can combine the ψ^--related and ψ^+-related Bell trials into a single hypothesis test[40].

Apart from these modifications, all settings, analysis software, calibrations and stabilisation routines were identical to those in the first run[39].

In this test we set the total number of Bell trials $n_2 = 300$. After 210 hours of measurement over 22 days during 1 month, we find $S_2 = 2.35 \pm 0.18$, with S_2 the weighted average of equation (5.1) for ψ^- heralded events (different detectors clicked), and $S_{\psi^+} = \langle x \cdot y \rangle_{(0,0)} + \langle x \cdot y \rangle_{(0,1)} - \langle x \cdot y \rangle_{(1,0)} + \langle x \cdot y \rangle_{(1,1)}$ for ψ^+ (same detectors clicked). See Fig. 5.6.

This yields a P-value of 0.029 in the conventional analysis[39] (which assumes independent trials, perfect random number generators and Gaussian statistics), and with $k_2 = 237$ a P-value of 0.061 in the complete analysis[39] (which allows for arbitrary memory between the trial, partially predictable random inputs and makes no assumptions about the probability distributions).

5.5 Combined P-value for the two tests

We now turn to analysing the statistical significance of the two runs combined. Extending the conventional analysis, we take the weighted sum of the CHSH parameters obtained for both tests to find $S_{\text{combined}} = 2.38 \pm 0.136$, yielding a P-value of $2.6{\cdot}10^{-3}$. For the complete analysis, we give here two cases. The first case is where the tests are considered to be fully independent; we can then combine the P-value using Fisher's method, resulting in a joint P-value of $1.7 \cdot 10^{-2}$ for the complete analysis. In the second case we consider the two runs as a single test; we can then combine the data, and find $k_1 + k_2 = 433$ for $n_1 + n_2 = 545$, resulting in a joint P-value of $8.0{\cdot}10^{-3}$ for the complete analysis. We emphasize that these are extreme interpretations of a

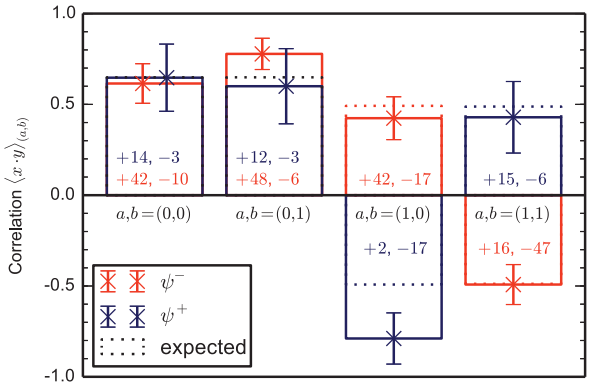

Figure 5.6 — Second Loophole-free Bell test results. (a) Summary of the data and the CHSH correlations. We record a total of $n_2 = 300$ trials of the Bell test. Dotted lines indicate the expected correlation based on the spin readout fidelities and the characterization measurements presented in Fig. 5.4. Shown are data for both ψ^- heralded events (red, two clicks in different APD's at location C), and for ψ^+ heralded events (orange, two clicks in the same APD). Numbers in bars represent the amount of correlated and anti-correlated outcomes respectively, for ψ^- (red) and ψ^+ (orange). Error bars shown are $\sqrt{\left(1 - \langle x \cdot y \rangle^2_{(a,b)}\right)/n_{(a,b)}}$, with $n_{(a,b)}$ the number of events with inputs (a, b).

subtle situation and these P-value should be considered accordingly.

5.6 Choosing different heralding window settings in post-processing

Although the predefined event-ready filter settings were used for the hypothesis tests presented, the datasets recorded during the Bell experiments contain all the photon detection times at location C. This allows us to investigate the effect of choosing different heralding windows in post-processing. Such an analysis does not yield reliable global P-value(look-elswehere effect), but can give insight in the physics and optimal parameters of the experiment. In Fig. 5.7 we present the dependence of the recorded Bell violation S, and number of Bell trials n, if we offset the start of the windows. For negative offsets, photo-detection events caused by reflected laser light starts to play an important role, and as expected the Bell violation decreases since the event-ready signal is in that regime no longer a reliable indicator of the generation of an entangled state. The observed difference between the runs in offset times at which the laser reflections start to play a role are caused by the less aggressive filter settings in the second run. However, we see that in both runs the S-value remains constant up a

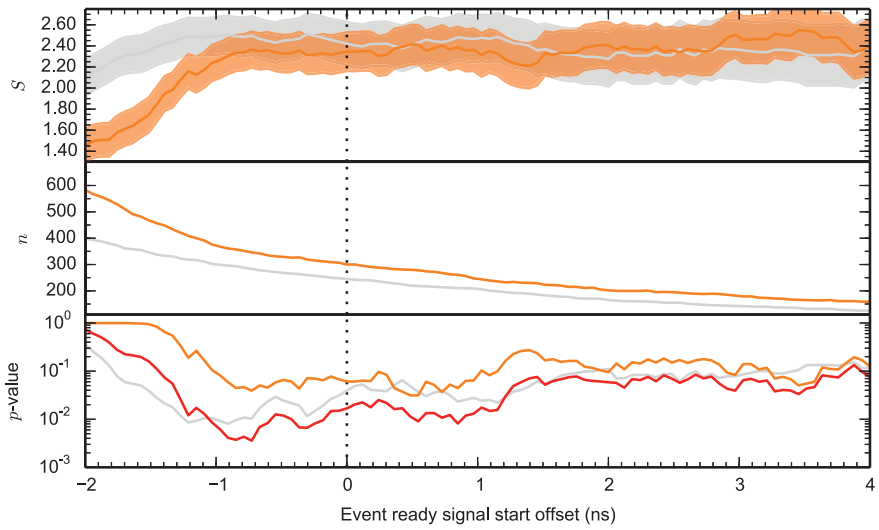

Figure 5.7 — CHSH parameter S, number of Bell trials n, and post-selected P-value versus window start offset for the event-ready photon detections at location C, for the first (grey) and second (orange) dataset. A combined P-value using Fischer's method is also shown in red. The time offset shown is with respect to the windows given in Sections 5.9.5 and 5.4 for the first and second run, respectively. Thus, the dotted line at zero denotes the settings as defined prior to starting the Bell experiment and used in e.g. Figs. 5.5 and 5.6. Confidence region shown is one sigma, calculated according to the conventional analysis. Shifting the window back in time, the relative fraction of heralding events caused by clicks from the excitation laser reflections increases, thereby reducing the observed Bell violation.

negative offset of about 0.8 ns, indicating that the filter settings were still chosen on the conservative side.

5.7 Bell violation for shorter readout duration

The data presented in Figs. 5.5 and 5.6 considered the maximum integration time allowed for the spin readout, given a 160 ns time for the generation of a random number, that still ensures the required locality conditions. By shortening the integration time-window in post-processing, we can explore testing additional models beyond those included in our null hypothesis. In particular, shortening the readout window while still observing a violation can test theories where the inputs are already determined earlier by some unknown physics. We can shift the proposed determination of the

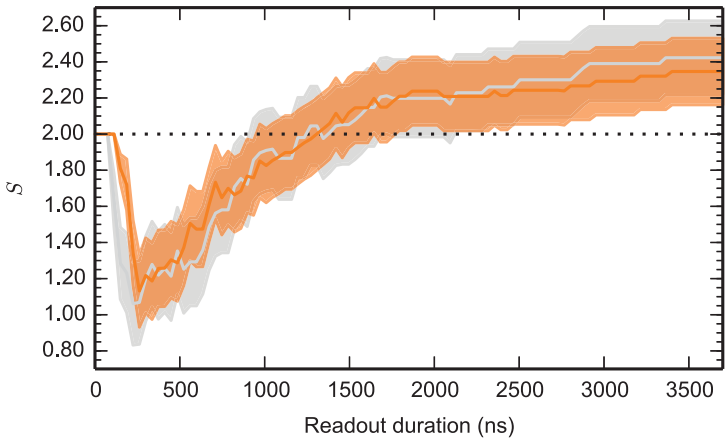

Figure 5.8 — CHSH parameter S versus readout integration time at locations A and B, for the first (grey) and second (orange) dataset. Confidence region shown is one sigma, calculated according to the conventional analysis.

inputs further back in time, until the event-ready signal will no longer be space-like separated from the random input at location A (see Fig. 5.3a). At this point we have 690 ns for the generation of a random bit. Shortening the readout to retain the required locality conditions given the earlier determined inputs, we find a violation of $S = 2.39 \pm 0.21$ and $S_2 = 2.30 \pm 0.19$, which would correspond to a joint P-value using Fisher's method of 0.034 for the complete analysis. Note however that our null hypothesis formulated before the test is based on using a 3700 ns readout duration, and further analysis may be required to find the actual P-value for shorter readout durations. Alternatively, one can test theories that predict a maximum speed of physical influences beyond the speed of light. Fig. 5.8 shows the dependence of the S parameter on the readout integration time.

5.8 Conclusion

Our experiment realizes the first Bell test that simultaneously addresses both the detection loophole and the locality loophole. Being free of the experimental loopholes, the setup tests local-realist theories of nature without introducing extra assumptions such as fair-sampling, a limit on (sub-)luminal communication or the absence of memory in the setup. Our observation of a statistically significant loophole-free Bell inequality violation thus indicates rejection of *all* local-realist theories that accept that the number generators produce a free random bit in a timely manner and that the outputs are final once recorded in the electronics. This result places the strongest

restrictions on local realistic theories of nature to date.

Strictly speaking, no Bell experiment can exclude all conceivable local-realist theories, because it is fundamentally impossible to prove when and where free random input bits and output values came into existence[15]. Even so, our loophole-free Bell test opens the possibility to progressively bound such less conventional theories: by increasing the distance between A and B (for example, to test theories with increased speed of physical influence); using different random input bit generators (to test theories with specific free-will agents, for example, humans), or by repositioning the random input bit generators (to test theories where the inputs are already determined earlier, sometimes referred to as "freedom-of-choice"[10]). In fact, our experiment already enables tests of all models that predict that the random inputs are determined a maximum of 690 ns before we record them, because the inequality is still violated for a much shorter spin readout (Sec. 5.7).

Combining the presented event-ready scheme with higher entangling rates (for example, through the use of optical cavities) provides prospects for the implementation of device-independent quantum key distribution[23] and randomness certification[24,25]. In combination with quantum repeaters, this might enable the realization of large-scale quantum networks that are secured through the very same counter-intuitive concepts that inspired one of the most fundamental scientific debates for 80 years[1,2].

5.9 Supplementary Information - Experimental

5.9.1 Experimental setup

The experiments are performed on individual NV centres that are naturally present in high purity type IIa chemical-vapor deposition diamond samples (Element Six), with a $\langle 111 \rangle$ crystal orientation. In its negative charge state, the NV centre ground state is an electronic spin triplet with total spin 1. The zero-field splitting separates the $|m_s = 0\rangle$ and $|\mathrm{m}_s = \pm 1\rangle$ levels by 2.88 GHz. Additionally we split the $|\mathrm{m}_s = \pm 1\rangle$ levels by 0.14 GHz using a static magnetic field applied along the defect axis. We use the two levels $|m_s = 0\rangle$ and $|m_s = -1\rangle$, denoted as $|\uparrow\rangle$ and $|\downarrow\rangle$, respectively. We use microwave control pulses, applied via a gold stripline deposited on the sample surface, to rotate the electronic ground state spin. The carrier frequency of the pulses is resonant with the $|\mathrm{m}_s = 0\rangle$ to $|\mathrm{m}_s = -1\rangle$ ground state transition. The electronic spin resonance spectrum of both NV centres is split into three lines by the hyperfine interaction with the host nitrogen nuclear spin of the defect. Therefore, we chose a Hermite pulse envelope shape, which provides a broad and flat spectral distribution. In this way, we achieve a π rotation within 180 ns with a fidelity exceeding 99.8% without initializing the nitrogen nuclear spin state.

The samples are kept at a temperature of 4 K in closed-cycle cryostats (Montana Instruments) to enable resonant optical excitation of spin-dependent transitions. This

enables fast single-shot readout and high-fidelity optical initialization of the electronic spin state. The design of the electronics and optical setup is described in detail in previous work[32,41]. To initialize the electronic spin into $|\downarrow\rangle$, we apply resonant excitation on the $|m_s = \pm 1\rangle \leftrightarrow |E'\rangle$ optical transition, achieving an initialization fidelity of more than 99.8% within 5 μ s. Electronic spin readout is accomplished by resonant excitation of the $E_x(E_y)$ transition for the sample in setup A (B). To guarantee a high readout fidelity by minimizing the spin mixing in the excited state, we chose samples with low transversal strain splitting and additionally use d.c. Stark tuning by applying d.c. electric fields to the on-chip electrodes (Fig. 5.2a inset). The average strain splitting during the experiment was 1.8 (2.3) GHz in sample A (B).

A high photon collection efficiency is a prerequisite for high fidelity optical single-shot readout and high-efficiency entanglement. To overcome the limitation of total internal reflection of the emitted photons, we fabricate solid immersion lenses in the diamond surface around preselected NVs (oriented along the $\langle 111 \rangle$ crystal direction) using a focused ion beam. In addition, we deposit a single-layer aluminium oxide anti-reflection coating. We select devices with a particularly high phonon-sideband (PSB, wavelength > 640 nm) photon collection efficiency in our home-built confocal microscope setups, which we measure to be $(13 \pm 2)\%$. Note that this value includes the 80% quantum efficiency of the detectors. The zero-phonon line (ZPL) photon emission of each NV is separated from the PSB using a dichroic long-pass and an additional tunable bandpass filter. Per optical excitation, we collect on average $2.9 \cdot 10^{-4}$ ($1.7 \cdot 10^{-4}$) ZPL photons at location C after propagation through a single mode fibre from location A (B). Measured fiber losses are 6 dB from A to C and 9 dB from B to C. On setup A, we use adaptive optics to couple the ZPL emission into the single mode fiber, increasing the efficiency by about a factor of two, compared to using standard optics (Sec. 5.9.12). We use two polarisers at C to block unwanted reflections from the excitation pulse. To compensate for polarization drift inside the fibers, an automated polarization control feedback loop adjusts two waveplates in front of the fiber couplers at A and B.

Synchronization of the individual setups is achieved via separate glass fiber connections. Distances between locations are determined using cartographic and altimetric data (Sections 5.9.6, 5.9.7).

One of the main challenges in performing the Bell experiment, is to maintain the required stability of all the involved NV centres, instruments, lasers and detection optics over a week time-scale. In Sec. 5.9.9 we list the various checks, optimisations and calibrations performed to achieve this goal.

5.9.2 Two-photon quantum interference (Fig. 5.4b)

Measurement of photon coincidences in different output ports of a beam splitter has become a standard tool to investigate the indistinguishability of single photons

generated by different sources. To account for potentially unequal efficiency of the sources, one can compare the case where the photons are indistinguishable to one where they are made distinguishable on purpose. In our experimental system, using orthogonal polarization is prohibited by in-line fibre polarisers. We instead program the experimental sequence such that setup A generates photons in an 'early' time window and setup B in a 'late' time window which is delayed with respect to the early one by 300 ns. Since this is much longer than the optical lifetime of the NV centre, this allows us to clearly distinguish which of the setups has emitted a given detected photon. During the measurement this distinguishable setting is alternated (every 3750 excitation pulses) with the indistinguishable setting, in which both setups produce photons that arrive at the same time at the beamsplitter.

In the data analysis for the distinguishable setting the arrival times of the photons in the late time window (coming from setup B) are shifted back by 300 ns in order to overlap them with those from setup A. In this way, we can present the data in a more familiar way (Fig. 5.4b). Note also that the data in Fig. 5.4b is taken on a different NV pair than the one used in the other experiments; the two pairs are very similar and are therefore expected to yield equivalent results.

5.9.3 Model of the entangled state (Figs. 5.4c and 5.5a)

We estimate the readout fidelities of NV A and B from the daily calibration measurements during the recording of the XX and ZZ entanglement data (Fig. 5.4c). We find: $F_0^A = 0.9536 \pm 0.0030$, $F_1^A = 0.9940 \pm 0.0011$, $F_0^B = 0.9390 \pm 0.0034$, $F_1^B = 0.9982 \pm 0.0006$. Using these values, we correct the spin-photon correlation data of Fig. 5.4a for readout errors[41], to obtain the residual errors made in the spin-photon correlation, $e^{A,B}_{\text{early,late}}$ presented in the caption of Fig. 5.4a.

To obtain an estimate for the fidelity of the generated entangled state, we model the state of the two NVs after a successful heralding event by a density matrix of the following form (See SI of[41]):

$$\rho = \frac{1}{2}\begin{pmatrix} 1-F_z & 0 & 0 & 0 \\ 0 & F_z & -VF_z & 0 \\ 0 & -VF_z & F_z & 0 \\ 0 & 0 & 0 & 1-F_z \end{pmatrix}. \tag{5.2}$$

Here we set

$$F_z = \frac{1}{2}\left((1-e^A_{\text{early}})(1-e^B_{\text{late}}) + (1-e^B_{\text{early}})(1-e^A_{\text{late}})\right), \tag{5.3}$$

V can be estimated from the measured interference contrast in Fig. 5.4b, in combination with the expected 3% reduction in phase coherence from the instability in excitation laser frequency (see section 5.9.11 below). The statistical uncertainty in the estimated V is large because of the small number of events in the interference experiment. Our

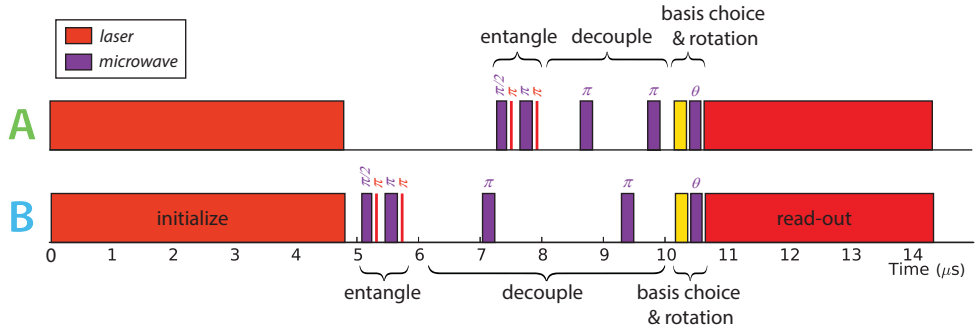

Figure 5.9 — Pulse sequence of the experiment. First, the spins at A (top) and B (bottom) are initialized by optical pumping. Then we perform the entangling sequence, consisting of two microwave and two optical pulses, followed by a dynamical decoupling sequence consisting of two microwave π-pulses that preserves the spin coherence. Finally, the readout basis is chosen and implemented and the spins are read out.

best estimate is $V \approx 0.9 * 0.97 = 0.873 \pm 0.060$. This yields an estimate for the state fidelity $\langle \Psi^- | \rho | \Psi^- \rangle = 0.92 \pm 0.03$. To get the expected correlation values for Fig. 5.4c, we numerically perform the corresponding final basis rotations $U_{a,b}$ on ρ and apply the expected readout-errors on the obtained density matrix. We use the same model to numerically find the best basis settings for the Bell experiment and to calculate the expected correlators in Fig. 5.5a. This results in an expected S-parameter of 2.30 ± 0.07.

5.9.4 Dynamical decoupling sequence

The coherence of the NV centre spins is limited by the interaction with a bath of ^{13}C nuclear spins, resulting in a dephasing time T_2^* of a few μ s. To counteract this dephasing we apply a dynamical decoupling sequence that consists of two microwave (MW) π-pulses with appropriate spacing. The full experimental pulse sequence is shown in Fig. 5.9. To quantify the remaining detrimental effect of spin dephasing during the experiment, we omit the two optical π-pulses used to generate the spin-photon entanglement and replace the last MW rotation by a $\pi/2$ pulse. Ideally, this sequence should bring the spin to the state $|\downarrow\rangle$. The measured probability to end up in this state is above 99 % showing that decoherence is efficiently mitigated.

5.9.5 Event-ready signal settings

The signal that heralds successful entanglement, recorded at location C, consists of one photon detection event in an early time window and one in a late time window, each in a different output port of the beam splitter. We have to define the start- and stop times of these 2×2 windows. Ideally the windows only contain detection

events due to photons emitted by the NV centres at location A and B. The start time of the window should be late enough such that unwanted reflections from the laser excitation pulse are filtered out, while the stop time should be early enough such that the background count-rate is not dominating the detection probability.

We use the characterisation data of the ZZ and XX entanglement runs presented in Fig. 5.4c to decide on time-window settings for the event-ready signal, prior to starting the Bell experiment. Fig. 5.10 illustrates the method used to obtain a good window start-time and length, for each of the two channels, for the early time-window. For the late time-window we use the same settings, but shifted by the fixed time between the two laser excitation pulses in the entanglement protocol (250 ns).

5.9.6 Location and distances

The experiment comprises three locations, A, B and C, defined as the position of the three time-tagging devices used. For locations A and B, the random number generators were located within 1 metre distance from the time-taggers, and the diamond samples and local photon detectors within 2 metre distance. For location C, the beam-splitter and photon detectors were located within 1 metre distance from the time-tagger. For each location X,Y and Z coordinates are determined in the following way:

First, a reference point on the outer wall of the building containing the setup is chosen. Then, the XYZ coordinates of the reference point are determined using the Large Scale Standard Map of The Netherlands (GBKN[42]), which has an accuracy better than 0.3 m, combined with the current elevation map of the Netherlands (AHN)[43], with a horizontal accuracy better than 0.5 m, and a vertical accuracy better then 0.1 m. Note that this accuracy is comparable to what can be obtained with GPS aided measurements. Finally, the relative position of the setup to the reference point is determined by manual distance measurements. The coordinates obtained in this manner are shown in Table 5.1. By converting to 3-dimensional Cartesian coordinates, the relative distances between the three locations is calculated with an uncertainty of less than ± 1.5 m.

5.9.7 Synchronisation of the experimental setups

Direct communication between the three labs A, B and C is implemented by means of electronic-optical converters (Highland Technology J720/J724/J730) and infrared optical fibres. To synchronize A and B during the Bell test, we send and record a common start reference time before every entanglement attempt. Towards this end, a trigger signal is sent by the arbitrary waveform generator (AWG) of B to both the time-tagger at C and the AWG at A. We calibrate the static trigger delays between A-B and B-C by measuring the round trip delays, including AWG trigger delay and local cable delays. The measured values are shown in Table 5.2.

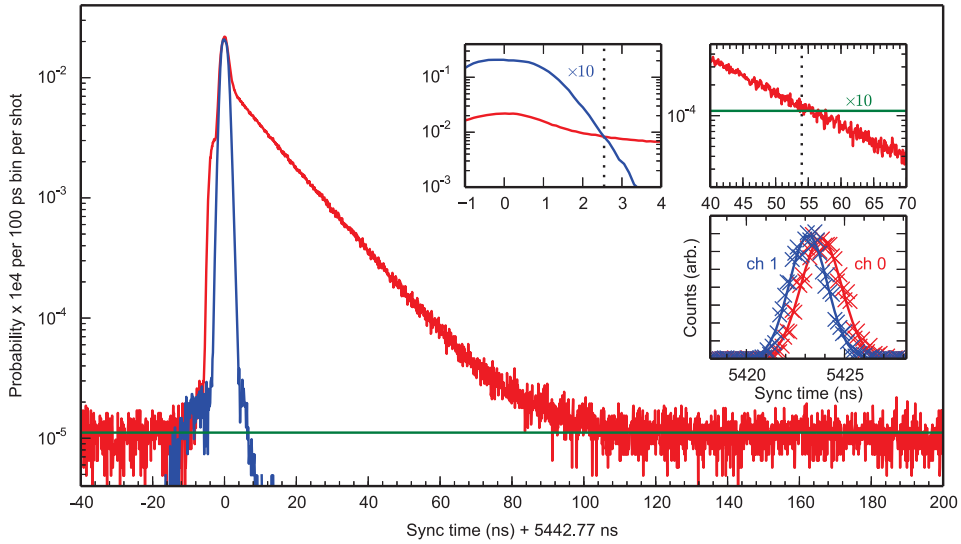

Figure 5.10 — Obtaining time-window settings for the event-ready signal. Red line: Histogram of the arrival times of the early time-bin photons from both setups together, during the XX entanglement characterisation, measured at location C. We can clearly distinguish the 2 ns, Gaussian shaped excitation pulse, followed by the exponential decaying emission from the NV's, and finally the constant background countrate. (The 1 ns plateau observed just before the laser pulse was caused by a reflection on an optical element in the excitation path of setup A). From simulations we expect to obtain $S > 2$ only when the probability to obtain a click from either NV is at least 10 times larger than the probability to obtain a spurious click from either the laser pulse or the background. Using the independently measured shape of the laser pulse (blue line), and the background count-rate fitted from the histogram after 120 ns (green line), we determine the start and stop of the filter window that satisfies this criterion (upper insets). We find a time window of $2.55 - 55$ ns after the centre of the laser-pulse. Before starting the Bell experiment, we measured the arrival of the laser pulse for the (different) detectors used, for each channel (lower inset). From the Gaussian fit, we find the centre of the laser pulse to be at 5423.80 ± 0.01 ns and 5423.15 ± 0.01 ns after the arrival of the sync pulse, for detectors 0 and 1 respectively. We then fixed the window settings for heralding events at C, to be used in the Bell test: the early window starts 5426.35 (5425.70) ns after the sync-pulse, and stops 5478.80 (5478.15) ns after the sync-pulse for channel 0 (channel 1). A fit of the exponential part of the curve yields a excited state lifetime of 12.20 ± 0.02 ns

Table 5.1 —Coordinates of the relevant locations. RD XY coordinates are Dutch RD coordinate system[44], Z coordinates are NAP according to the NLGEO2004 definition[44]. Latitude, longitude and height are calculated WGS84, using RDNAPTRANS™(2008) transformations.

Location	RD X (m) latitude (°)	RD Y (m) longitude (°)	NAP height (m) geometric height (m)
A	85441.0 (N 52.001358)	446371.7 (E 4.374233)	-1.75 (41.7)
B	85920.3 (N 51.990753)	445185.0 (E 4.381451)	-3.43 (40.0)
C	85490.9 (N 51.996959)	445881.5 (E 4.375059)	-3.41 (40.1)

As a cross check, we use the independently measured trigger delay between A-C, and verify that the time delay between the routes B-C and A-B-C matches the expected value. Any potential instability in the trigger delays during the measurement would immediately be detected at the time-tagger at C by a shift in the arrival time of the laser pulse-photons coming from A and B.

Table 5.2 —Trigger delays between lab locations. For A-C, the AWG trigger delay is included. The given uncertainty values assume a worst case scenario, where all individual uncertainties add up linearly.

Trigger delays	Time (ns)	Uncertainty (ns)
A - B	9347	10
B - C	5526	8
A - C	3391	8

5.9.8 Random number generation

We use two accelerated laser phase diffusion quantum random number generators[45] (QRNGs) of identical construction, designed and built at ICFO - The Institute of Photonic Sciences. The design, modelling, and testing of these devices is described in detail in[34]. As described there, each QRNG continually generates partially random "raw" bits at a rate of 200 MHz and performs a running parity calculation to output processed bits that aggregate the randomness from all previous raw bits. At the time an output bit is taken for use as a measurement setting, only the most recent k raw bits will still be space-like separated from the distant measurement station, and thus only these k bits contribute local randomness. Based on the timing diagram shown in Fig. 5.3, and subtracting delays in the QRNG device (10 ns), internal delays of the sampling FPGA (30 ns), and cable delay to the time-taggers (10 ns), the window for generation of space-like separated raw bits is 160 ns, and thus $k = 32$.

The predictability $\mathcal{P}$ of the output (ideally $\mathcal{P} = 1/2$ for a perfect random bit source) is $\mathcal{P} \leq \frac{1}{2} + \tau^{(k)}$, where $\tau^{(k)}$ bounds the excess predictability of the extracted bit. Due to the parity calculation, $\tau^{(k)}$ decreases by roughly a factor of ten for each increment of k, reaching $\tau^{(k)} \leq 10^{-5}$ for $k \geq 6$. The model uses a 6σ bound on untrusted noise sources and "fully paranoid" assumptions about how these noises combine[34].

While the derived predictability errors $\mathcal{P}$ for $k = 32$ are too small to be tested (verifying this would require an impractical quantity of data), we can verify the validity of the predictions up to a given statistical significance. Prior to the experiment the QRNGs were tested at $k = 4$, achieved by keeping only every fourth output bit. Note that $k = 4$ output should, by the same model, have predictability errors $\leq 10^{-4}$. We applied the test suites NIST SP800-22 (1.5 Gb for each QRNG) and more extensively TestU01 Alphabit battery (210 Gb and 255 Gb), always finding results consistent with ideal randomness. The largest files tested contained $2^{33} \approx 8$ Gb and $2^{34} \approx 17$ Gb, respectively. Using the statistical uncertainty of a test of length 2^{33}, we obtain a 2σ error bound of $\mathcal{P} < \frac{1}{2} + 2\frac{1}{2\sqrt{2^{33}}} = \frac{1}{2} + 1.08 \times 10^{-5}$. We use this latter number as the predictability error τ in the P-value calculation, but note that this is conservative as the theoretical model predicts that the $k = 32$ predictability error is smaller.

During the experiment, the continued performance of the QRNGs was monitored in two ways: First, the regulated reference voltage of the comparator after the pin photo-diode (see Fig. 1 of[34]) was checked every 10 seconds to exclude failure of the phase-locked loop, laser, interferometer, and photo-detector. Second, we recorded a subset of 2^{23} random bits, generated during the course of the Bell experiment, observing means of $\frac{1}{2} + 5.8 \times 10^{-5}$ and $\frac{1}{2} + 1.3 \times 10^{-4}$, consistent with the zero bias of a properly functioning device, considering the statistical uncertainty of $\frac{1}{2\sqrt{2^{23}}} = 1.7 \times 10^{-4}$.

5.9.9 Experimental control and stability

A typical experimental run proceeds as follows (see Fig. 5.11): Both Adwin controllers perform a charge-resonance check (CR check, see below). Adwin A sends a trigger signal to B when the CR-check is successful. When Adwin B is also ready, it triggers AWG B, which in turn sends out an initial 'sync-pulse' signal, to trigger AWG A. AWG B waits for the pre-calibrated A-B trigger delay (see Table 5.2), and then proceeds with 250 repetitions of the programmed pulse sequence (Fig. 5.9). Similarly, AWG A runs 250 repetitions of its sequence, as soon as it receives the initial sync-pulse. When finished, both AWGs trigger their Adwin to start the next CR check. This cycle repeats itself until the run is quit manually, or until the 45 minute run time is over.

A major challenge for our experiment is to keep a complex setup with many critical components stable over the long integration time necessary to collect data, in order to ensure entanglement generation, spin rotations and spin readout with a high fidelity that is required to observe a violation of the Bell inequality. To maintain stable operation for a period of several weeks, we employ a combination of pre-selection,

parameter feedback, periodic calibration and optimisation measurements. Additionally, we monitor various key experimental indicators while running the Bell experiment. If an indicator is outside of the pre-defined range, the current run is either stopped completely, or a signal is recorded in the data to indicate that the setup is in an invalid state (see section 5.9.10). Note that if this happens, no data from previous trials or the current trial is discarded (only trials that were marked as invalid in advance are affected).

Below we list all aspects of the setups that were actively stabilized and monitored, from short to long time-scale.

- Every 250 entanglement attempts (3.75 ms), we ensure that both NVs are negatively charged and on resonance with the excitation lasers (CR-check, see[30]). We excite both the $|\mathrm{m}_s = \pm 1\rangle \leftrightarrow |E'\rangle$ and the $|\mathrm{m}_s = 0\rangle \leftrightarrow |E_x(E_y)\rangle$ optical transitions during 50 μ s for setups A (B), while counting the number of detected photons. If no photon is detected, the NV centre is assumed to be in its neutral charge state NV^0 and a yellow laser, resonant to the NV^0 zero-phonon line, is applied to transfer the centre back to NV^-. If, however, the number of photons exceeds a pre-set threshold (between 30-40 counts), the experiment proceeds with the entanglement sequence. Otherwise, the experiment repeats the check, until the threshold is met.

- An automated feedback loop stabilizes the NV excitation and emission frequency to the two red excitation lasers, by tuning the d.c. electric field applied to the gold gate-electrodes. Before each CR check, the arrival of photon detections are correlated with a 0.1 V, 50 μ s period modulation of the gate electrode. This signal is averaged over about 1000 CR checks (few seconds), and serves as the error signal for the feedback. In a similar manner the laser frequency of the yellow laser is stabilized to the NV^0 zero-phonon line, using a modulation of the AOM driving frequency, while counting photon detections during the yellow repump phase.

- Every 10 seconds, both setups check proper functioning of a few key devices (AWG, wavemeters, laser stabilisation). If a check fails, the run is stopped and the setup waits for human intervention. Additionally, the control program monitors:

  - The average counts during the CR-check. If too low, we assume that the automated gate voltage feedback has failed. A slow scan of the gate voltage, spanning a larger range than the feedback loop, is made to find back the optimum point. During the scan, the recorded attempts are marked invalid. If still too low, or too high, we assume that the NV dipole polarization has drifted. This requires the excitation polarisation to be adjusted manually.

  - The average counts obtained during the yellow repump phase. If too low, we assume the automated yellow laser frequency feedback has failed. A slow sweep of the yellow laser frequency is made, and the optimum point is set. During the scan, the recorded attempts are marked invalid.
  - The strain splitting, calculated from the current red laser frequencies. If this splitting is not within the predefined range (1.5 - 1.8 GHz for NV A, 1.5 - 2.4 GHz for setup B), the subsequent data is marked invalid until the strain splitting is within range again. This is typically achieved by manually tuning the readout laser excitation frequency.
  - The amount of unwanted reflections of the excitation light from the surface of the diamond. If this is above a predefined threshold, the setup performs an automated scan of the waveplate angles in the ZPL emission path (see Fig. 5.2a) to improve the polarisation rejection of the excitation laser. The reflections are measured for both setups independently by integrating a specific time-window of the arrival of photons at location C. During the spin-initialisation part of the protocol, we identify parts in the histogram for which only photons from one of the setups arrive. If the amount of reflections integrated in a time-window corresponding to the arrival of the 2 nanosecond laser excitation pulse is higher than the integrated NV emission, the subsequent attempts are marked as invalid.

- Every 5 minutes, we scan the spin pumping laser, and set it to the point producing optimal CR-counts. The data recorded during the scan is marked invalid.

- After each 45-minute run, the spatial positions of both objectives are optimized to ensure reproducible NV excitation and photon collection. Furthermore, the laser powers are recalibrated.

- Every day, we perform a spin-photon correlation measurement as presented in Fig. 5.4a. If the obtained correlations show errors higher than expected, the microwave pulses for spin rotations are recalibrated. We also check the performance of the final basis rotation (fast microwave switch), spin-coherence and spin readout. Finally, we check the photon detection probabilities per optical excitation at location C, from both setups. If the detection probability drops below 2.3×10^{-4} (1.4×10^{-4}) for setup A (B), we re-align the detection optics of the ZPL emission.

5.9.10 Data recording and processing

The time-tagging devices at locations A and B record the following events:

- R_0: a 'zero' was generated by the QRNG;

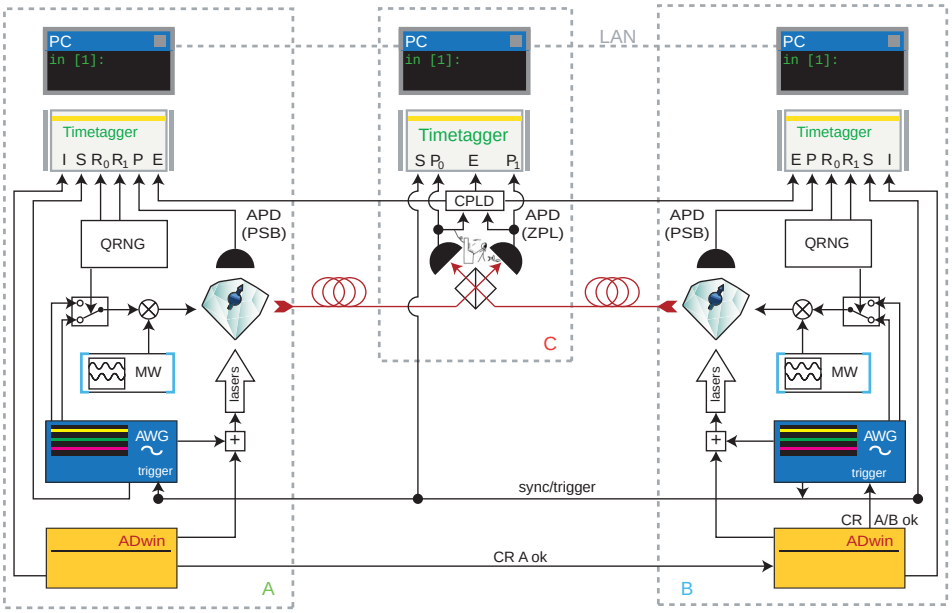

Figure 5.11 — Control schematic of the experiment. The experiment is performed in three separate laboratories A, B and C (grey dashed lines). The experiments at A and B use a real-time control unit (Jäger ADWIN Pro II). Each repetition starts by repeatedly checking whether the NV emission frequency is on resonance with the excitation lasers (CR). Once this check is successful on setup A, its ADWIN passes a signal to setup B. When B has also successfully passed the test, ADWIN B triggers AWG B, which in turn triggers AWG A. Both AWGs then output a synchronization signal (S) which is recorded by their respective time-taggers, whose signal is read out in blocks using a PC. The AWGs also output the fast control sequence that is applied to the NV centres. Towards this end, they control the laser pulses and output two different microwave (MW) pulses that perform the basis rotations in the Bell experiment. A microwave switch controls which of these two pulses is applied to the NV centre, depending on the output of the QRNG. The value of the generated random bit (R0 or R1) is recorded by time-tagging devices, alongside with the NV spin state readout signal (P) that is detected by single photon detectors (APD). At location C, two APDs detect upcoming ZPL photons, whose arrival time is recorded by another time-tagger. Upon consecutive detection of two photons, a programmable logic device (CPLD) outputs a signal that is used to mark these instances in the time-tagging data (input E). This allows the PCs at A and B to directly discard experimental runs in which no entanglement was generated, thus keeping the amount of stored data in reasonable bounds.

- R_1: a 'one' was generated by the QRNG;
- P: a click was detected in the local phonon-side band emission;
- E: an entanglement heralding signal was received from the CPLD at location C;
- I: One of the benchmark indicators (section 5.9.9) is outside of the pre-defined range, which causes the Adwin to send a pulse to this channel every 250 entanglement attempts.

For each of these recorded events, the total number of sync-pulses (S) detected since the start of the run is saved, as well as the time passed since the last sync-pulse. Every few hundred milliseconds, the recorded events are transferred to the PC. During the experiment, about 2 megabyte of data is generated every second. To keep the size of the generated data-set manageable, blocks of about 100000 events are saved to the hard drive only if an entanglement heralding event (E) is present in that block.

The time-tagging device at location C records the following events:

- P_0: a click was detected in output port 0 of the beam-splitter;
- P_1: a click was detected in output port 1 of the beam-splitter;
- E: an entanglement heralding signal was received from the CPLD;

For each of these events, the current number of detected sync-pulses (S) since the start of the run is recorded, as well as the time passed since the last sync-pulse and the total time passed since the start of the run. As the data-rate is orders of magnitude lower here, all data is saved to the hard-drive.

For each run, we first extract the data of those attempts where entanglement was successfully generated, i.e. all data that has the same sync-pulse number as an entanglement heralding signal E. We then determine if this is a valid trial of the Bell experiment, determined by following criteria:

1. At location C, the recorded photon arrival times were within the bounds of the pre-defined filters (see Sec. 5.9.5).
2. At location A and B, there was no invalid marker I recorded in one of the previous 250 attempts.
3. At location A and B, no local photon P was recorded in a time-window of 200 ns after the two optical excitations for entanglement generation.

We emphasize that all events that determine whether or not an iteration is a valid Bell trial either are recorded in the past light-cone of the random basis choice (2. and 3.) or are space-like separated from the random basis choice (1.) of both A and B.

All rounds that fulfil the above criteria are a Bell trial, corresponding to $t = 1$, in the language of the statistical analysis presented in Sec. 5.10.1 below. For these events, we extract the generated random numbers and readout results of both setups A and B. For setup A, an event on channel R_0 corresponds to $a = 0$, an event on R_1 indicates $a = 1$. The readout result $x = +1$ is assigned if within the readout integration time-window (as defined by the spacetime analysis presented in Fig. 5.3), there is at least one readout detection event (channel P) recorded and $x = -1$ otherwise. For setup B, b and y are assigned analogous.

5.9.11 Stabilization of the excitation laser frequency

In our previous demonstration of entanglement between remote spins separated by 3 meters[32], both NV defects were excited by the same laser, and the difference in optical path length from this laser to either of the NV centres was much smaller than the coherence length of the laser. Therefore, the relative phase between early and late time-bin of the photonic wavepacket could be described in a common rotating frame - that of the laser source. In the present experiment, the large separation between the two setups requires excitation by two independent laser systems. Retaining the common reference frame upon interference of the time-bin encoded photonic qubits requires that the source lasers in both setups imprint the same phase difference between early and late time bin. To accomplish this, a digital feedback loop is used to stabilize the frequency of one laser to that of the other.

Fig. 5.12 shows a schematic of this feedback loop. A small fraction of the excitation laser of setup A is frequency-shifted by 135 MHz by an acousto-optical modulator. Using a fibre-based beamsplitter, this laser field is interfered with a part of the light of laser B, which has been transmitted to laboratory A using an additional optical fibre of 1.6 km length.

To stabilize the relative frequency of the lasers, the interference signal is recorded using a fast amplified photodetector (Thorlabs PDA10). The beat frequency is compared to the RF source signal that drives the AOM using a digital phase-frequency detector (Menlo systems DXD200). The output of this device is applied to the current of laser diode A, shifting its frequency and thus closing the feedback loop. The remaining 200 kHz (FWHM) relative frequency deviation is an effect of the limited short-term stability of the used diode lasers (Toptica TA-SHG pro). An additional fibre delay line of 1 km length reduces the effect of drifts in the frequency of laser B on the relative frequency difference of the pulses that excite the NV centres.

In this configuration, we measured the fluctuations in the phase of the driving lasers using an analog phase detector to be about 0.2π FWHM at the 250 ns time difference

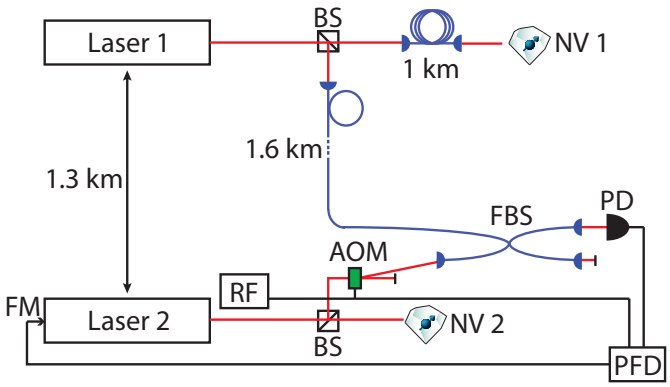

Figure 5.12 — Schematic of the relative laser frequency stabilization. FM: Laser frequency modulation input. RF: Radiofrequency source. BS: Beam splitter. FBS: Fibre beam splitter. PD: Photodiode. PFD: Phase-frequency detector. NV: Nitrogen-vacancy centre. AOM: Acousto-optical modulator.

between the two excitation pulses. According to our calculations, this should lead to a fidelity reduction of the XX correlations of about 3%. Further improvement would be possible by reducing the laser linewidth, e.g. with an external reference cavity, or by decreasing the temporal separation between the two time-bins.

5.9.12 Adaptive optics

We use a deformable mirror (Boston Micromachines) in the ZPL detection path of setup A to compensate for optical aberrations due to fabrication imperfections of the solid immersion lens. To optimize the mirror surface, the NV centre is off-resonantly excited by a 532-nm green laser and the collected fluorescence signal is optimized by step-wise varying the mirror surface according to Zernike polynomials up to eleventh order[46]. The optimized shape of the mirror surface is represented in the inset of Fig. 5.13. The increase in collection efficiency is characterized by comparing saturation curves measured locally on the setup A for a flat and optimized mirror configuration, as shown on Fig. 5.13. The evolution of the ZPL count rates versus the excitation power P_{e} is fit to the function :

$$A_{sat}\frac{P_{\mathrm{e}}}{P_{\mathrm{e}}+P_{\mathrm{sat}}} \tag{5.4}$$

with the maximum count rate A_{sat} and the saturation power P_{sat} as free parameters. We find $A_{sat} = 18(1)$ kcts when the mirror surface is flat, and $A_{sat} = 35(2)$ kcts after optimizing. Thus, for this particular solid immersion lens, the use of adaptive optics allows for an increase in collection efficiency by a factor of 1.9(1).

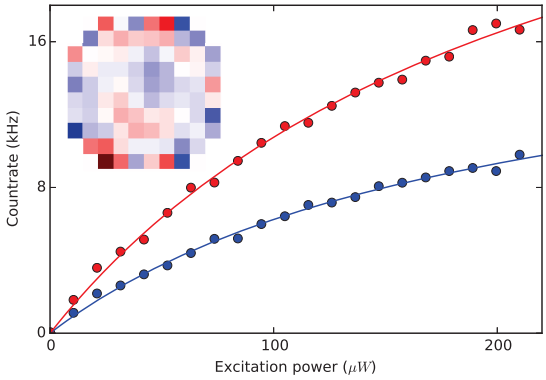

Figure 5.13 — Saturation curve. The NV is excited with a green laser of varying power and the resulting emission into the zero-phonon line is measured with a flat (blue data) and with an optimized (red data) mirror surface. From the fit curves (red and blue lines), we deduce an increase in collection efficiency by a factor of 1.9. The inset shows a heat map of the actuator voltages, where red (blue) rectangles denote positive (negative) excursion.

5.10 Supplementary Information - Statistical Analysis

Local hidden variable models (LHVM) predict concrete limitations on the statistics that can be observed in a Bell experiment. These are typically phrased in terms of probabilities or expectation values. Naturally, however, in any experiment we can only observe a finite number of events, and not probabilities. We thus need to quantify the statistical evidence against an LHVM given a finite number of events.

A common way to analyse statistics in Bell experiments is to compute the number of standard deviations that separate the observed data from the best LHVM. However, this method has well known flaws [18,22,47] (see [48] for a detailed discussion). In particular, we would have to assume Gaussian statistics and independence between subsequent attempts, allowing for the memory loophole. Fortunately, it is possible to rigorously analyze the statistics even when allowing for memory as was first done by Gill [49]. Instead of the standard deviation, intuitively, one bounds the probability of observing the experimental data, if nature was indeed governed by an LHVM. In the language of hypothesis testing, this is known as the P-value, where the null hypothesis is that the experiment can be modelled as an LHVM (see e.g. [50]). Informally, we thus have

$$P\text{-value} = \max_{\text{LHVM}} \Pr\left[\begin{array}{l|r} \text{data at least as} & \text{experiment is} \\ \text{extreme as observed} & \text{governed by LHVM} \end{array}\right]. \tag{5.5}$$

A small P-value can be interpreted as strong evidence against the null hypothesis, that is, that the experiment was governed by an arbitrary LHVM. There is an extensive literature regarding methods for evaluating the P-value in Bell experiments [18,22,48–60]

and discussions regarding the analysis of concrete experiments and loopholes[14,61–67].

Here, we focus on the case of the CHSH inequality as relevant for our experiment. For the simple case of the CHSH inequality, it has been shown how to derive tight bounds on the P-value if the settings are chosen uniformly. Such a bound was first informally derived in[18], and later rigorously developed by Bierhorst[51] whose approach we will follow closely with two modifications: First, the analysis of[51] was done for uniform and independent choices of measurement settings. We extend the approach of[51] to the case where A and B use a partially predictable RNG[34]. Second, although our experiment can readily be seen to correspond to an event-ready scheme in the sense of Bell, we formally include the event-ready procedure in our analysis.

5.10.1 How to compute the P-value

See Fig. 5.1a; an event-ready Bell experiment consisted of m entanglement attempts. Let $\mathbf{t}^m = (t_i)_{i=1}^m$ denote the output signal of the "event-ready"-box, where the tag $t_i = 0$ corresponds to a failure (no, not ready) event, and $t_i = 1$ to a successful preparation (yes, ready) of the boxes A and B. We will reserve the word *trial* for the attempts that correspond to a successful preparation. Throughout, we use superscripts m to remind ourselves a sequence $\mathbf{t}^m$ has m elements. Let $\mathbf{a}^m = (a_i)_{i=1}^m, \mathbf{b}^m = (b_i)_{i=1}^m$ denote the inputs to boxes A and B in Fig. 5.1a, where $a_i, b_i \in \{0, 1\}$. Furthermore, let $\mathbf{x}^m = (x_i)_{i=1}^m, \mathbf{y}^m = (y_i)_{i=1}^m$ with $x_i, y_i \in \{\pm 1\}$ denote the output of boxes A and B.

We denote by $|\mathbf{t}^m|$ the number of ones in the binary sequence $\mathbf{t}^m$. Since we will use only the attempts where $t_i = 1$, let us define

$$n := |\mathbf{t}^m| = \sum_{i=1}^{m} t_i \tag{5.6}$$

to be the number of attempts in which $t_i = 1$, where n is fixed as discussed below. Given the observed values $\mathbf{a}^m, \mathbf{b}^m, \mathbf{x}^m, \mathbf{y}^m$, and $\mathbf{t}^m$ recorded in the experiment, we can compute the CHSH function

$$k := \sum_{i=1}^{m} t_i \cdot \frac{(-1)^{a_i b_i} x_i y_i + 1}{2} \ . \tag{5.7}$$

Note that k is the number of times that $(-1)^{a_i b_i} x_i y_i = 1$. When viewing CHSH as a non-local game[15], k is thus the number of times that Alice and Bob win the CHSH game. For large n, and uniform distribution of the inputs, we have $k \approx n(S + 4)/8$, where S is the value of the familiar CHSH correlator. We prove that

$$P\text{-value} \leq P_{n,k}(\mathbb{B}_\xi) = \sum_{j=k}^{n} \binom{n}{j} \xi^j (1 - \xi)^{n-j} \ , \tag{5.8}$$

where $P_{n,k}(\mathbb{B}_\xi)$ is the probability that n i.i.d. (independent and identically distributed) Bernoulli trials with probability

$$\xi = 3/4 + 3(\tau + \tau^2) \tag{5.9}$$

have at least k successes. Here τ denotes a partial predictability of the inputs given the history of the experiment, defined in (5.12) and (5.13) below, where we take $\tau = \max\{\tau_A, \tau_B\}$. The value for τ used in the experiment is given in Sec. 5.9.8. We remark that n is fixed in this analysis, i.e., we stop the experiment if a certain number n of trials have been collected, where n was decided independently of the data observed.

Even though we allowed that the LHVM could depend on previous attempts, thus making no extra assumptions on the memory of the devices, the upper bound is the tail probability of an i.i.d. distribution. This is not at all uncommon for sums of random variables, and there are many other examples where such a simplification occurs (see for instance[68] and[69]).

5.10.2 Properties of the tested models

We introduce the sequence of random variables $(A_i, B_i, X_i, Y_i, T_i, H_i)_{i=1}^m$ in correspondence with the concrete outcomes as described above, where i is used to label the i-th element: let $\mathbf{A}^m = (A_i)_{i=1}^m, \mathbf{B}^m = (B_i)_{i=1}^m$ denote the inputs to the boxes, $\mathbf{X}^m = (X_i)_{i=1}^m, \mathbf{Y}^m = (Y_i)_{i=1}^m$ the outputs of the boxes, $\mathbf{T}^m = (T_i)_{i=1}^m$ the sequence of event-ready signals, and $\mathbf{H}^m = (H_i)_{i=1}^m$ the histories of attempts previous to the i-th attempt. We make no assumptions regarding the statistics of the event-ready procedure, which may be under full control of the LHVM, and can depend arbitrarily on the history of the experiment. The random variable H_i models the state of the experiment prior to the measurement. As such, H_i includes any hidden variables, usually denoted using the λ symbol[15]. It also includes the history of all possible configurations of inputs and outputs of the prior attempts $(A_j, B_j, X_j, Y_j, T_j)_{j=1}^{i-1}$.

We consider all models that restrict the random variables in the following way:

1. *Local randomness generation.* Conditioned on the history of the experiment the inputs A_i, B_i are independent of each other

$$\forall i, A_i \perp\!\!\!\perp B_i \mid H_i \ , \tag{5.10}$$

and of the output of the event-ready signal

$$\forall i, A_i \perp\!\!\!\perp T_i, B_i \perp\!\!\!\perp T_i \mid H_i \ . \tag{5.11}$$

We allow A_i and B_i to be partially predictable given the history of the experiment:

$$\forall(i, a_i, h_i), \Pr\left(A_i = a_i | H_i = h_i\right) \leq \frac{1}{2} + \tau_A \ , \tag{5.12}$$

$$\forall(i, b_i, h_i), \Pr\left(B_i = b_i | H_i = h_i\right) \leq \frac{1}{2} + \tau_B \ . \tag{5.13}$$

2. *Locality.* The outputs x_i and y_i only depend on the local input settings and history: they are independent of each other and of the input setting at the other side, conditioned on the previous history and the current event-ready signal:

$$\forall i, (X_i, A_i) \perp\!\!\!\perp (Y_i, B_i) | H_i, T_i \ . \tag{5.14}$$

3. *Sequentiality of the experiments.* Every one of the m attempts takes place sequentially such that any possible signalling between different attempts beyond the previous conditions is prevented[18].

Except for these conditions the variables might be correlated in any possible way.

Given the experimental setup and sequence as described in this chapter and Figs. 5.1, 5.2 and 5.3, all local realist theories that predict that the number generators produce a free random bit in a timely manner, and that the output is final once recorded in the electronics, satisfy these restrictions.

5.10.3 Proof outline

Let us briefly sketch the idea of the proof - full details can be found in the online version of the Supplementary Information of Hensen *et al.*[39], or in Elkouss and Wehner[40]. The p-value is the probability that if the null hypothesis were true - i.e. a LHVM can model the experiment - we observe at least k or more times $(-1)^{a_i b_i} x_i y_i = 1$, for *any* possible LHVM. In the language of non-local games, this means that the p-value is the probability that Alice and Bob win the CHSH game at least k times, maximized over all possible LHVM strategies. Note that since we wait until n successful entanglement events (trials) are made, the LHVM can use a much larger number m of entanglement attempts than observed in our experiment in order to win at least k times in n trials. Our proof consists of the following three steps.

Step 1 is to bound the probability that $(-1)^{a_i b_i} x_i y_i = 1$ for a particular entanglement attempt i, conditioned on the entire history of the experiment, as well as the value of the event-ready signal. I.e., we bound the probability that Alice and Bob win the next game, conditioned on anything in the past. This is essentially a derivation of the CHSH inequality. The history of the experiment includes any prior state of the experimental apparatus, hidden-variables and inputs and outputs of the boxes in previous attempts. To obtain this bound, we use conditions 1,2 in Sec. 5.10.2.

Step 2 is to replace the conditioning on the entire history of the experiment, with a conditioning only on values previously recorded in the experiment. This is a consequence of the law of total probability. The motivation for this step is to condition on things actually recorded, while the general history is not accessible to an experimenter.

Step 3 then bounds the probability that Alice and Bob win at least k times on n trials by an inductive argument: intuitively we peel off trial by trial, where at each peel we apply the analysis of Step 2 to bound the probability of the next trial given the previous ones.

5.11 Supplementary Information - Second dataset

5.11.1 Random numbers from Twitter

After each potential heralding event (corresponding to the E-events described in Sec. 5.9.10), both at location A and B we take 8 new bits from a predefined random dataset (one for A and one for B) based on Twitter messages, to send to the FPGA-based random-number combiner.

The random dataset for A was obtained by collecting 139952 messages from Twitter trending topic with hash-tag #2DaysUntilMITAM, starting from 14:47:58 November 11th, 2015. The messages were collected using the Python Tweepy-package (www.tweepy.org). Only the actual message text was used (no headers), consisting of at most 140 Unicode characters. From each message a single bit was obtained by first converting each character into an integer representing its Unicode code point, converting the integer to the smallest binary bit-string representing that number and finally taking the parity of all the resulting bit-strings together (even or uneven number of ones). The dataset for B was similarly obtained from 134501 messages with the hash-tag #3DaysTillPURPOSE, streamed prior to the dataset A, starting from 16:52:44 November 10th, 2015.

We note that although one may expect the Justin Bieber and One Direction fan-bases to be sufficiently disjoint to produce an uncorrelated binary dataset, the hashtag from dataset B featured in 2 out of 139952 tweets of dataset A, and vice-versa in 4 out of 134501 tweets. Still, a Fisher-exact independence test of A (first 134501 bits) and B's dataset results in a P-value of 0.63. The bias of the 8-bit parity sets were 0.44% and 0.95%, with statistical uncertainty ($\frac{1}{2\sqrt{N}}$) of 0.38% and 0.39% for A,B receptively. As these bits are XOR'ed with bits from the quantum random number generator with much smaller bias, this has no expected effect on the bias in the used input settings. Finally, we characterized the performance of the FPGA combiners, which showed no errors on 10^8 XOR operations.

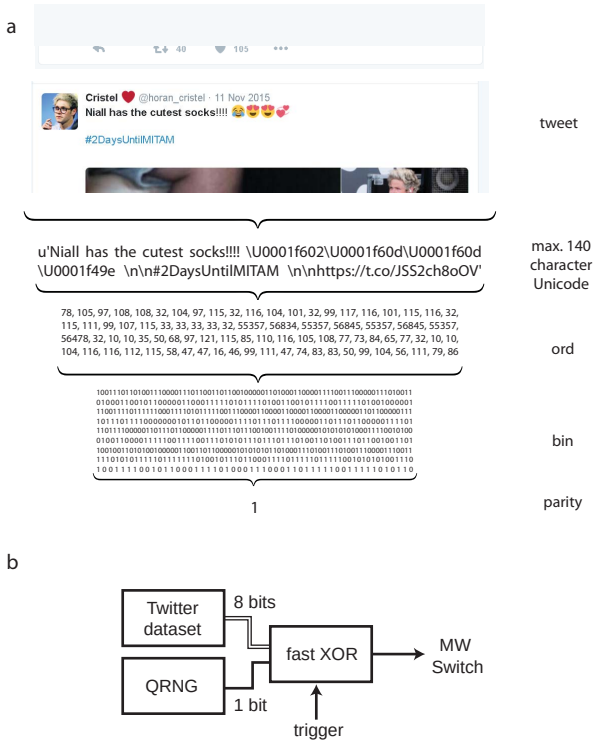

Figure 5.14 — Extracting random bits from twitter messages. Schematic of random input bit generation by combining bits from a quantum random number generator (QRNG) and classical random bits from a dataset based on Twitter messages.

5.11.2 APD replacement

After 5 days of measurement, the APD at location C corresponding to channel 0 broke down during the daily calibration routine and was subsequently replaced. To take into account the changed detection-to-output delay for the event-ready filter settings, the laser pulse arrival time was recorded for the new APD before proceeding. Fig. 5.15 shows a laser pulse arrival time histogram taken just before the start of the second Bell run, and just after replacing the APD. We adapted the start of the event-ready window for channel 0 accordingly, and used this for all the data taken afterwards.

5.11.3 Joint P-value for ψ^- and ψ^+ heralded events

Here we expand the statistical analysis given in Sec 5.10 to incorporate the ψ^- and ψ^+ events into one hypothesis test. For each of these states we perform a different

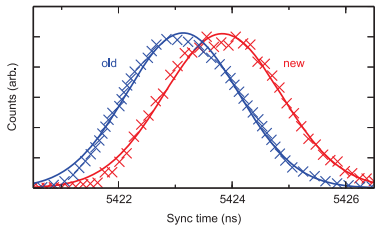

Figure 5.15 — New detector delay Arrival of the excitation laser pulse measured at location C, with respect of the arrival of the sync-pulse, for the channel 0 APD, before and after replacing the broken APD. From the Gaussian fits we find that the new detector detects the laser pulse (700 ± 14) picoseconds earlier than the initial detector.

variant of the CHSH game, and then use the methods of Elkouss and Wehner[40] to combine the two: The output signal of the "event-ready"-box $\mathbf{t}^m = (t_i)_{i=1}^m$ now has three possible outcomes, where the tag $t_i = 0$ still corresponds to a failure (no, not ready) event. We now distinguish two different successful preparations of the boxes A and B: $t_i = -1$ corresponds to a successful preparations of the ψ^- Bell state, and $t_i = +1$ to a ψ^+ Bell state. In terms of non-local games, Alice and Bob are playing two different games, where in case $t_i = -1$ they must have $(-1)^{a_i b_i} x_i y_i = 1$ in order to win, and in case of $t_i = +1$ they must have $(-1)^{a_i (b_i \oplus 1)} x_i y_i = 1$ to win. Note that both games have the same maximum winning probabilities. This means that we can take $k := k_- + k_+$, with k_- the number of times $(-1)^{a_i b_i} x_i y_i = 1$, and k_+ the number of times $(-1)^{a_i (b_i \oplus 1)} x_i y_i = 1$; the remainder of the analysis remains the same and in particular the obtained bound to the P-value is unchanged (see also Elkouss and Wehner[40], in particular the discussion on page 20). We then have for the adapted CHSH function (Eq. 5.7):

$$k' := \sum_{i=1}^{m} |t_i| \cdot \frac{(-1)^{a_i (b_i + \frac{t_i+1}{2})} x_i y_i + 1}{2} , \tag{5.15}$$

and adapted total number of events (Eq. 5.6) then becomes:

$$n' := |\mathbf{t}^m| = \sum_{i=1}^{m} |t_i|. \tag{5.16}$$

5.11.4 Statistical analysis of settings choices

For both the Bell tests presented in this chapter, we are testing a single well-defined null hypothesis formulated before the experiment, namely that a local-realist model for space-like separated sites could produce data with a violation at least as large as we observe. The settings independence is guaranteed by the space-like separation

of relevant events (at stations A, B and C). Since no-signalling is part of this local realist model, there is no extra assumption that needs to be checked in the data. We have carefully calibrated and checked all timings to ensure that the locality loophole is indeed closed.

Nonetheless, one can still check (post-experiment) for many other types of potential correlations in the recorded dataset if one wishes to. However, since now many hypotheses are tested in parallel, P-value should take into account the fact that one is doing multiple comparisons (the look-elsewhere effect, LEE). Failure to do so can lead to too many false positives, an effect well known in particle physics. In contrast, there is no LEE for a single pre-defined null hypothesis as in our Bell test.

Formulation and testing of multiple hypotheses can result in obtaining almost arbitrarily low local P-value, which may have almost no global significance. As an example, recalculating the P-value for the local realist hypothesis, given the first dataset for a window start offset of -900 picoseconds compared to the predefined window starts, results in a local P-value of 0.0081 using the complete analysis (see Fig. 5.7). Taking this to the extreme by doing a search of the window start offsets for both channels independently and the joint window length offset, results in a local P-value of 0.0018. These examples clearly illustrate that without taking into account that multiple hypotheses are being tested, such local P-value can not be used to assign significance.

With these considerations in mind we analyse the settings choices in the two sub-sections below.

Settings choices in the first and second dataset

The distribution of the 245 input settings in the first dataset (see Fig. 5.5) is $(n_{(0,0)}, n_{(0,1)}, n_{(1,0)}, n_{(1,1)}) = (53, 79, 62, 51)$, with $n_{(a,b)}$ the number times the inputs (a, b) were used. This realisation looks somewhat unbalanced for a uniform distribution, and one could be motivated to test the null hypothesis that the RNGs are uniform. Performing a Monte-Carlo simulation of 10^5 realisations of a uniform multinomial distribution with size $n = 245$ we find a local P-value of 0.053 to get such a distribution or more extreme. We can get further insight by looking at all the setting choices recorded during the test. Around every potential heralding event about 5000 settings are recorded, for which we find a local P-value of 0.57 (Table 5.3), consistent with a uniform setting distribution.

Many additional tests can be performed on equally many slices or subsets of the data, where one or more of the filters (Sec. 5.9.10) is relaxed. In Table 5.3 we list the individual (local) P-value for a set of 4 hypotheses regarding the settings choices, for both the first and second dataset.

1. RNG A is uniform

dataset		$n_{(0,0)}$	$n_{(0,1)}$	$n_{(1,0)}$	$n_{(1,1)}$	n	RNG A	RNG B	RNG A&B	Pearson	Fisher	$p_{\text{threshold}}$	p_{joint}
Run 1	All recorded data	4938847	4942101	4939328	4942337	19762613	0.872	0.159	0.568	0.956		0.016	0.144
	Bell trials	**53**	**79**	**62**	**51**	**245**	0.250	0.371	0.054		0.029	0.021	0.121
Run 2	All recorded data	4529615	4530943	4528295	4526440	18115293	0.171	0.901	0.486	0.455		0.016	0.144
	Bell trials	**69**	**69**	**78**	**84**	**300**	0.184	0.773	0.545		0.817	0.018	0.131
Bell trials of both runs combined		**122**	**148**	**140**	**135**	**545**	**0.864**	**0.392**	**0.452**		**0.211**	**0.020**	**0.138**

Table 5.3 —From left to right each column corresponds with: dataset on which statistics are computed, local P-value for the null hypothesis RNG A is uniform, local P-value for the null hypothesis RNG B is uniform, local P-value for the null hypothesis RNG A&B is uniform, Fisher's test, Pearson's test, and $p_{\text{threshold}}$ and joint P-valuep_{joint}. The joint P-value for a set of hypotheses is the probability that for at least one of the hypotheses we observe a P-value less than α where here $\alpha = 0.05$. This captures the fact that the more hypotheses we test, the more likely it becomes that one of them will fall below the significance threshold. The value $p_{\text{threshold}}$ the largest threshold for individual tests for which the joint P-value for that row is less than 0.05. The local P-value in the row should this be compared to this number. This captures the fact that when testing multiple hypothesis, the local P-value of the individual ones actually need to be much smaller for the overall test to be significant. The local P-value in columns RNG A, RNG B, Fisher and Pearson are exact calculations. The columns RNG A&B, $p_{\text{threshold}}$ and p_{joint} are approximations obtained via 10^5, 10^4 and 10^4 trials of a Monte-Carlo simulation, respectively.

2. RNG B is uniform
3. RNG A and RNG B are jointly uniform
4. Fisher's exact test[70] for $n < 5000$, Pearson's χ^2 test[71] for $n > 5000$)

For tests 1 and 2 we evaluate a two tailed binomial test with equal success probability. For test 3 we perform a Monte-Carlo simulation of 10^5 realisations of a uniform multinomial distribution with size fixed to the number of observations in that particular row, i.e. $n = 245$ for the second row in Table 5.3.

We observe that only one local P-value is below 0.05: Fisher's exact test on the distribution of the settings in the first data set yields a local P-value of 0.029. However, as described in Sec. 5.11.4 below, when properly taking the look-elsewhere effect into account this does not result in a significant rejection of the uniform settings hypothesis at the 0.05 level. Finally, the valid Bell trials of the first and second dataset combined, shown in the last row of Table 5.3, are also consistent with uniformly chosen input settings.

Significance and look-elsewhere effect

We now analyse the significance of the local P-value in Table 5.3 by taking into account the look-elsewhere effect. Say we are looking for correlations between parameters that are in fact completely independent. Looking at one correlation, it is as if we take one random sample from a distribution; the probability that it is at 2 sigma or

more extreme is thus about 0.05. If we look for 4 different correlations (assuming all parameters are independent), it is similar to taking 4 random samples, and thus the probability that at least one is at 2 sigma or more extreme is $1-(1-0.05)^4 = 0.18$. In reverse, assuming fully independent hypotheses, the local P-value p' should have obeyed roughly $1-(1-p')^4 < 0.05$, so $p' < 0.013$, to be statistically significant at the 0.05 level.

In our case it is actually more complicated because there can be dependencies between hypotheses. We can numerically get some of these numbers. For instance, we have simulated the random number generation (RNG) using Monte-Carlo under the assumption of independent uniform outputs and calculated local P-value for the four hypotheses listed above. The probability that at least one of these yield local P-value $p' < 0.05$ turns out to be about 0.13 for the 245 events in the Bell test. This is different from $1-(1-0.05)^4 = 0.18$ because of correlations between the tests, but it is clearly much higher than 0.05. In reverse, to arrive at an overall probability of 0.05 of finding at least one test yielding local P-value $p' < p_{\text{threshold}}$ for the data in the first Bell dataset, we find $p_{\text{threshold}} = 0.021$. In other words, if we would only be looking at the settings corresponding to the valid Bell trials, then a local P-value below 0.021 would signal a statistically significant violation of our hypothesis at the 0.05 level. We do not find such evidence for the valid Bell trial data (see first row in Table 5.3).

The last column gives the probability that at least one of the hypothesis tests on the data in that row yields a local P-value $p' < 0.05$, given uniform settings. In the one-but-last column we give $p_{\text{threshold}}$, again only for the data set in that row, for a significance at the 0.05 level. These values assume that we would only be testing our hypotheses on that particular row. Since we are now looking at different rows, $p_{\text{threshold}}$ for each row is a strict upper bound to the $p_{\text{threshold}}$ for the full table, as we are looking at different cross-sections of the raw data set at the same time; the $p_{\text{threshold}}$ for the full table will thus be lower but it is not trivial to compute this, given the large dependence between the subsets of data used for each row. However, since we do not find any local P-value to be below $p_{\text{threshold}}$ for the corresponding row, we can conclude that the data does not allow rejection of the settings independence hypothesis, even without calculating the global $p_{\text{threshold}}$ for the full Table.

5.12 Bibliography

[1] A. Einstein, B. Podolsky and N. Rosen. Can quantum-mechanical description of physical reality be considered complete? *Physical Review* **47**, 777 (1935).

[2] J. Bell. On the einstein-podolsky-rosen paradox. *Physics* **1**, 195 (1964).

[3] S. J. Freedman and J. F. Clauser. Experimental test of local hidden-variable theories. *Physical Review Letters* **28**, 938 (1972).

[4] A. Aspect, J. Dalibard and G. Roger. Experimental test of bell's inequalities using time- varying analyzers. *Physical Review Letters* **49**, 1804 (1982).

[5] W. Tittel, J. Brendel, H. Zbinden and N. Gisin. Violation of bell inequalities by photons more than 10 km apart. *Physical Review Letters* **81**, 3563 (1998).

[6] G. Weihs, T. Jennewein, C. Simon, H. Weinfurter and A. Zeilinger. Violation of bell's inequality under strict einstein locality conditions. *Physical Review Letters* **81**, 5039 (1998).

[7] M. A. Rowe *et al.* Experimental violation of a bell's inequality with efficient detection. *Nature* **409**, 791 (2001).

[8] D. N. Matsukevich, P. Maunz, D. L. Moehring, S. Olmschenk and C. Monroe. Bell inequality violation with two remote atomic qubits. *Physical Review Letters* **100**, 150404 (2008).

[9] M. Ansmann *et al.* Violation of bell's inequality in josephson phase qubits. *Nature* **461**, 504 (2009).

[10] T. Scheidl *et al.* Violation of local realism with freedom of choice. *Proceedings of the National Academy of Sciences* **107**, 19708 (2010).

[11] J. Hofmann *et al.* Heralded entanglement between widely separated atoms. *Science* **337**, 72 (2012).

[12] W. Pfaff *et al.* Demonstration of entanglement-by-measurement of solid-state qubits. *Nature Physics* **9**, 29 (2013).

[13] M. Giustina *et al.* Bell violation using entangled photons without the fair-sampling assumption. *Nature* **497**, 227 (2013).

[14] B. G. Christensen *et al.* Detection-loophole-free test of quantum nonlocality, and applications. *Physical Review Letters* **111**, 130406 (2013).

[15] N. Brunner, D. Cavalcanti, S. Pironio, V. Scarani and S. Wehner. Bell nonlocality. *Reviews of Modern Physics* **86**, 419 (2014).

[16] A. Garg and N. D. Mermin. Detector inefficiencies in the einstein-podolsky-rosen experiment. *Physical Review D* **35**, 3831 (1987).

[17] P. H. Eberhard. Background level and counter efficiencies required for a loophole-free einstein-podolsky-rosen experiment. *Physical Review A* **47**, R747 (1993).

[18] J. Barrett, D. Collins, L. Hardy, A. Kent and S. Popescu. Quantum nonlocality, bell inequalities, and the memory loophole. *Physical Review A* **66**, 042111 (2002).

[19] J. S. Bell. Bertlmann's socks and the nature of reality. *Le Journal de Physique Colloques* **42**, C2 (1981).

[20] M. Żukowski, A. Zeilinger, M. A. Horne and A. K. Ekert. Event-ready-detectors" bell experiment via entanglement swapping. *Physical Review Letters* **71**, 4287 (1993).

[21] C. Simon and W. T. M. Irvine. Robust long-distance entanglement and a loophole-free bell test with ions and photons. *Physical Review Letters* **91**, 110405 (2003).

[22] R. D. Gill. Time, finite statistics, and bell's fifth position. *Proc. of "Foundations of Probability and Physics - 2.* Växjö Univ. Press (2003), *Ser. Math. Modelling in Phys., Engin., and Cogn. Sc.*, volume 5, 179–206.

[23] A. Acín *et al.* Device-independent security of quantum cryptography against collective attacks. *Physical Review Letters* **98**, 230501 (2007).

[24] R. Colbeck. *Quantum and Relativistic Protocols for Secure Multi-Party Computation.* Ph.D. thesis, University of Cambridge (2007).

[25] S. Pironio *et al.* Random numbers certified by bell's theorem. *Nature* **464**, 1021 (2010).

[26] J. F. Clauser, M. A. Horne, A. Shimony and R. A. Holt. Proposed experiment to test local hidden-variable theories. *Physical Review Letters* **23**, 880 (1969).

[27] J. S. Bell. *Speakable and Unspeakable in Quantum Mechanics: Collected Papers on Quantum Philosophy.* Cambridge University Press, 2 edition (2004).

[28] P. G. Kwiat, P. H. Eberhard, A. M. Steinberg and R. Y. Chiao. Proposal for a loophole-free bell inequality experiment. *Physical Review A* **49**, 3209 (1994).

[29] I. Gerhardt *et al.* Experimentally faking the violation of bell's inequalities. *Physical Review Letters* **107**, 170404 (2011).

[30] L. Robledo *et al.* High-fidelity projective read-out of a solid-state spin quantum register. *Nature* **477**, 574 (2011).

[31] S. D. Barrett and P. Kok. Efficient high-fidelity quantum computation using matter qubits and linear optics. *Physical Review A* **71**, 060310 (2005).

[32] H. Bernien *et al.* Heralded entanglement between solid-state qubits separated by three metres. *Nature* **497**, 86 (2013).

[33] C. Abellán *et al.* Ultra-fast quantum randomness generation by accelerated phase diffusion in a pulsed laser diode. *Optics Express* **22**, 1645 (2014).

[34] C. Abellán, W. Amaya, D. Mitrani, V. Pruneri and M. W. Mitchell. Generation of fresh and pure random numbers for loophole-free bell tests. *Physical Review Letters* **115**, 250403 (2015).

[35] H. Bernien *et al.* Two-photon quantum interference from separate nitrogen vacancy centers in diamond. *Physical Review Letters* **108**, 043604 (2012).

[36] C. K. Hong, Z. Y. Ou and L. Mandel. Measurement of subpicosecond time intervals between two photons by interference. *Physical Review Letters* **59**, 2044 (1987).

[37] S. Ritter *et al.* An elementary quantum network of single atoms in optical cavities. *Nature* **484**, 195 (2012).

[38] S. Pironio. Random 'choices' and the locality loophole. *arXiv:1510.00248 [quant-ph]* (2015).

[39] B. Hensen *et al.* Loophole-free bell inequality violation using electron spins separated by 1.3 kilometres. *Nature* **526**, 682 (2015).

[40] D. Elkouss and S. Wehner. (nearly) optimal p-values for all bell inequalities. *arXiv:1510.07233 [quant-ph]* (2015).

[41] W. Pfaff *et al.* Unconditional quantum teleportation between distant solid-state quantum bits. *Science* **345**, 532 (2014).

[42] GBKN. GBKN, de standaard basiskaart van Nederland (2015).

[43] AHN. AHN - Actueel Hoogtebestand Nederland (2015).

[44] A. De Bruijne, J. Van Buren, A. Kösters and H. Van der Marel. *Geodetic reference frames in the Netherlands, Definition and specification of ETRS89, RD and NAP, and their mutual relationships.* NCG, Nederlandse Commissie voor Geodesie, Netherlands Geodetic Commission, Delft, The Netherlands (2005).

[45] C. Abellan *et al.* Ultra-fast quantum randomness generation by accelerated phase diffusion in a pulsed laser diode. *Optics Express* **22**, 1645 (2014).

[46] A. Hill, J. Nash, M. Graham, D. Hervas and P. Kwiat. Adaptive Optics for Single-Photon Fiber Coupling of Ions. OSA (2014), JW2A.128.

[47] P. Bierhorst. A rigorous analysis of the clauser-horne-shimony-holt inequality experiment when trials need not be independent. *Foundations of Physics* **44**, 736 (2014).

[48] Y. Zhang, S. Glancy and E. Knill. Asymptotically optimal data analysis for rejecting local realism. *Physical Review A* **84**, 062118 (2011).

[49] R. D. Gill. Accardi contra bell (cum mundi): The impossible coupling. *Lecture Notes-Monograph Series* 133–154 (2003).

[50] W. Van Dam, R. D. Gill and P. D. Grunwald. The statistical strength of nonlocality proofs. *Information Theory, IEEE Transactions on* **51**, 2812 (2005).

[51] P. Bierhorst. A rigorous analysis of the Clauser-Horne-Shimony-Holt inequality experiment when trials need not be independent. *Foundations of Physics* **44**, 736 (2014).

[52] A. Peres. Bayesian analysis of Bell inequalities. *Fortschritte der Physik* **48**, 531 (2000).

[53] J.-Å. Larsson and R. D. Gill. Bell's inequality and the coincidence-time loophole. *EPL (Europhysics Letters)* **67**, 707 (2004).

[54] A. Acín, R. Gill and N. Gisin. Optimal Bell tests do not require maximally entangled states. *Phys. Rev. Lett.* **95**, 210402 (2005).

[55] S. Pironio *et al.* Random numbers certified by Bell's theorem. *Nature* **464**, 1021 (2010).

[56] Y. Zhang, E. Knill and S. Glancy. Statistical strength of experiments to reject local realism with photon pairs and inefficient detectors. *Physical Review A* **81**, 032117 (2010).

[57] S. Pironio and S. Massar. Security of practical private randomness generation. *Physical Review A* **87**, 012336 (2013).

[58] Y. Zhang, S. Glancy and E. Knill. Efficient quantification of experimental evidence against local realism. *Physical Review A* **88**, 052119 (2013).

[59] R. D. Gill. Statistics, causality and bell's theorem. *Statist. Sci.* **29**, 512 (2014).

[60] P. Bierhorst. A robust mathematical model for a loophole-free Clauser-Horne experiment. *Journal of Physics A: Mathematical and Theoretical* **48**, 195302 (2015).

[61] J. E. Pope and A. Kay. Limited measurement dependence in multiple runs of a Bell test. *Physical Review A* **88**, 032110 (2013).

[62] J.-D. Bancal, L. Sheridan and V. Scarani. More randomness from the same data. *New Journal of Physics* **16**, 033011 (2014).

[63] J. Kofler and M. Giustina. Requirements for a loophole-free Bell test using imperfect setting generators. *arXiv preprint arXiv:1411.4787* (2014).

[64] J.-A. Larsson *et al.* Bell-inequality violation with entangled photons, free of the coincidence-time loophole. *Phys. Rev. A* **90**, 032107 (2014).

[65] J.-Å. Larsson. Loopholes in Bell inequality tests of local realism. *Journal of Physics A: Mathematical and Theoretical* **47**, 424003.

[66] B. Christensen *et al.* Analysis of coincidence-time loopholes in experimental Bell tests. *arXiv preprint arXiv:1503.07573* (2015).

[67] E. Knill, S. Glancy, S. W. Nam, K. Coakley and Y. Zhang. Bell inequalities for continuously emitting sources. *Phys. Rev. A* **91**, 032105 (2015).

[68] V. Bentkus. On Hoeffding's inequalities. *Annals of probability* 1650–1673 (2004).

[69] I. Pinelis. Binomial upper bounds on generalized moments and tail probabilities of (super) martingales with differences bounded from above. *High dimensional probability*, Institute of Mathematical Statistics, 33–52 (2006).

[70] R. A. Fisher. On the interpretation of chi extasciicircum2 from contingency tables, and the calculation of p. *Journal of the Royal Statistical Society* **85**, 87 (1922).

[71] K. F. Pearson. X. on the criterion that a given system of deviations from the probable in the case of a correlated system of variables is such that it can be reasonably supposed to have arisen from random sampling. *Philosophical Magazine Series 5* **50**, 157 (1900).

Chapter 6

Conclusions and outlook

B.J. Hensen

6.1 Conclusions

The results of this thesis can be summarized as follows:

- We can generate entanglement between remote NV centre electronic spin qubits using a photonic heralded entanglement protocol.
- We can use this entanglement in combination with the control over the nitrogen nuclear spin to teleport an unknown quantum state from a nuclear spin in one diamond to the electron spin in another, unconditional on the result of the required local Bell-state measurement.
- The spin-photon entanglement using time-bin encoding makes the entanglement generation robust over longer fibre links that exhibit polarisation drifts.
- The spin-spin entanglement can be extended to 1.3 kilometres.
- We found strong evidence against the combined assumptions of free choice, local causality and macro-realism.

This thesis reports the first loophole-free Bell violation, challenging the classical notion of a non-superdeterministic, realistic, local universe. At the same time, the result strengthens our trust in the predictions of quantum theory. These results establish the NV centre spin register as a leading platform for building a - potentially device independent - quantum network. In the following sections we will discuss an outlook for future research directions with spins in diamond.

6.2 Foundational experiments

We have obtained evidence against the combined assumptions of free choice, local causality and macro-realism. The result triggers us to consider alternative hypotheses, not reject-able by our current experiment, that could be tested in future Bell-like experiments.

One option is to surrender local causality and accept that the fundamental limit is signal-locality: things are fine as long as we cannot actually use the theory (quantum theory) to signal faster than light. However, as Bell[1] writes:

> *The assertion that 'we cannot signal faster then light' immediately provokes the question: Who do we think* we *are?* We *who can make 'measurements',* we *who can manipulate 'external fields',* we *who can 'signal' at all, even if not faster than light? Do* we *include chemists, or only physicists, plants or only animals, pocket calculators or only mainframe computers?*

Alternatively, one can challenge the assumptions (1)-(3) in Sec. 1.2.2:

(1) If a macro-reality does not emerge at all or not quick enough (1b), our Bell violation does not imply nonlocality. Indeed if a macro-reality emerges too late it effectively opens up a locality loophole[2]: a local model could postpone its macro-realistic outcome until it has heard of the setting and outcome of the other side.

The emergence of a definite macro-reality from quantum theory is closely related to the traditional problem of quantum measurement. Going back to Bell[3]:

> *Thus in contemporary quantum theory it seems that the world must be divided into a wavy 'quantum system', and a remainder which is in some sense 'classical'. The division is made one way or another, in a particular application, according to the degree of accuracy and completeness aimed at. For me it is the indispensability, and above all the shiftiness, of such a division that is the big surprise of quantum mechanics.*

If one insists on a the existence macro-reality, then in this context a better description of how or when a macro-reality emerges from our quantum description is highly desirable. Future experiments that test physical collapse theories[4,5] can be studied experimentally[6,7] using for instance ultra-long coherence times of nuclear spins[8,9], in combination with long distance entanglement. A Bell-like test setup provides a natural test-bed for such theories, that do not necessarily need to assume quantum theory[10].

Due to the fundamentally subjective nature of human observation, one intriguing future Bell experiment could involve humans to do both the basis selection and the recording of events. Such an experiment would require a large distance to close the locality loophole, on the order of the distance Earth-Moon. Although

such a human centred experiment seems somewhat questionable from a scientific point of view, as Howard Wiseman recently put it[11]:

Such an Earth–Moon experiment is a worthy challenge for the next 50 years.

(2) One can assume the existence of special structures allowed by Einstein's theory of general relativity, such as closed time-like loops[12] or wormholes. In this case, locally, the causal structure of spacetime remains intact, but the space-time is weirdly shaped. It seems unlikely that such ad hoc appearance of exotic space-time structures around entangled particles would go unnoticed, perhaps an experiment could be imagined to exclude such possibility.

On the other hand, v-causal models[13–15] explain quantum nonlocality by causal influences travelling at a finite-speed, but faster than the speed of light. Future Bell experiments could further restrict the minimum speed, by increasing the distance between A and B. Recently it was shown that v-causal models imply access to superluminal signalling distributions of outcomes using 4-partite entangled states[16], suggesting an experimental test: such a test could in fact be embedded in a quantum network structure of 4 spatially separated nodes.

(3) Theories that predict that the settings used in the Bell test were determined by some earlier event, can explain the observed correlations locally, because the locality loophole effectively opens again[2,17]. Future Bell experiments could push the occurrence of such an event back in time by physically separating the sources of the setting-choices *and* the recording of the choices*. Again, using human setting choices is intriguing from a philosophical perspective, as we perceive ourself to have some kind of free choice.

Finally, note that full rejection of the free choice of input settings requires a conspiracy on a very large scale. Such a rejection goes beyond for example simple determinism, as even in a deterministic world one should not expect the extremely fine-tuned correlations of physical randomness devices and Twitter messages, required to explain the observed Bell violation. Such models are called super-deterministic, and are deemed beyond the reach of experimental methods.

6.3 Towards quantum networks with spins in diamond

A quantum network[19] refers to a model for quantum information processing that consist of nodes, containing stationary quantum systems that can be used as memory or small processing units, linked to other nodes by entanglement generated by exchange of flying quantum systems, generally photons. Such a quantum network provides an ideal setting for various implementations of secure quantum communication, as well as

*One such proposed experiment[18], that uses variations in light emitted by quasars on opposite sides of the universe, additionally requires the assumption that the light was not altered along the way.

a way of connecting future quantum computing nodes together, or even allowing secure execution of a client's programs on a larger quantum server. A recent proposal to implement a topological error correcting code using this quantum network architecture showed that the fault-tolerance thresholds of the entanglement generation process can be reasonably high ($\approx 10\%$) if the local error rates for initialization, control and measurement are on the order of one percent[20]. Finally a quantum network could be a test bed to test our notions of nonlocality in multipartite-, or otherwise more extreme scenarios[16,21].

An ideal node for a future quantum network consists of a stationary, few qubit register that can be initialized, controlled and projectively read out with high fidelity. It possesses an optical interface that allows high-fidelity spin-photon entanglement. At least part of the register should remain undisturbed by the operation of the optical interface, and have a long coherence time. The optical interface of each node should be able to emit indistinguishable photons, preferably with a short lifetime, a wavelength in the telecom-band and a efficient collection into single-mode fibre optics. Other desirable features are a somewhat scalable setup, with preferably no free-space optics and operation at liquid helium- or even room temperature.

The NV centre does not score top marks on the above wish-list, but does score averagely on all its individual points. The NV centre shows photoluminescence under excitation with visible light and is a stable single-photon emitter[22]. It has an electronic spin that can be initialized and read out optically, and manipulated with standard magnetic resonance techniques[23]. The NV's electronic spin naturally couples to a register of 3-10 nuclear spin qubits that can be initialized, controlled and read out via the electron spin with fidelities exceeding 90%[24–26]. The electron spin can be entangled with a single photon[27]. The results presented in this thesis further highlight the possibility of creating spin-spin entanglement though an optical link[28–30]. Recent results suggest that the nuclear spin-register can preserve its coherence for a significant number of rounds of entanglement generation[31]. The optical emission is at 637 nm, resulting in about 8 dB loss per kilometre of fibre. The optical lifetime of 12 nanoseconds results in reasonable count-rates, however the branching ratio of the phonon-side-band versus the zero-phonon line results in only 4% of the emission suitable for entanglement generation. Most characterized NV centres found in bulk diamond have similar properties, but not identical, and about 10% can currently be brought onto resonance using current DC stark tuning methods. The optical setup is currently free-space, and requires cooling of the diamond sample to liquid helium temperatures.

To improve the score and suitability of the NV centre as the node in a future quantum network, the foremost challenge to overcome is the optical interface efficiency. Both the non-ideal wavelength for fibre connections, and the small fraction of resonant photons should be targeted.

To change the branching ratio of the phonon-side-band versus the zero-phonon

line of the NV centre emission, the NV's interactions with either the vibrational or optical modes have to be altered. The most straightforward solution is to include the NV centre in an optical cavity. The Purcell effect can enhance the emission into the cavity mode relative to the other decay paths. If the cavity is resonant with the ZPL emission, this will increase the fraction of ZPL photons. Increased emission into the cavity mode can also enhance the collection efficiency, compared to the omnidirectional dipole emission. Various approaches to embed the NV in an optical cavity are being pursued[32–34]. To obtain a Purcell enhancement, ($F_P \sim Q\frac{\lambda^3}{V} \gg 1$) a high quality factor Q or small mode volume V with respect to the optical wavelength λ have to be attained. To obtain a small mode volume using photonic crystal or other solid-state cavities, the bulk diamond in general has to be micro-structured and NV's have to be implanted, or nano-sized diamond crystals have to be used. Obtaining table optical emission properties for NV's in such structures can be challenging[35,36]. A promising approach uses bulk diamond that is thinned down to micrometer thickness, coupled to a fibre based Fabry-Perot cavity[37–39].

To reduce fibre losses during the photonic entanglement generation, ideally the photon wavelength should be in the telecom-bands around 1300 or 1500 nm. This could be achieved by down-converting the single photons emitted by the NV centre using non-linear frequency difference generation[40,41]. Challenges in implementing this novel method are obtaining a high conversion efficiency, signal-to-noise ratio, and stable operation.

Finally, to further increase the coherence time of the register during the remote entanglement operation, a system could be envisaged consisting of two NV's spaced close enough to be dipole-coupled[42]. Here the nuclear spin register of one NV could form a memory that is very robust against optical manipulation of the other NV, that would be used for remote entanglement generation.

6.4 Bibliography

[1] J. S. Bell. La nouvelle cuisine. *Speakable and Unspeakable in Quantum Mechanics: Collected Papers on Quantum Philosophy*. Cambridge University Press (2004), 232–248.

[2] N. Brunner, D. Cavalcanti, S. Pironio, V. Scarani and S. Wehner. Bell nonlocality. *Reviews of Modern Physics* **86**, 419 (2014).

[3] J. S. Bell. Six possible worlds of quantum mechanics. *Speakable and Unspeakable in Quantum Mechanics: Collected Papers on Quantum Philosophy*. Cambridge University Press (2004), 181–195.

[4] N. Gisin. Quantum measurements and stochastic processes. *Physical Review Letters* **52**, 1657 (1984).

[5] G. C. Ghirardi, A. Rimini and T. Weber. Unified dynamics for microscopic and macroscopic systems. *Physical Review D* **34**, 470 (1986).

[6] D. Salart, A. Baas, J. A. W. van Houwelingen, N. Gisin and H. Zbinden. Spacelike separation in a bell test assuming gravitationally induced collapses. *Physical Review Letters* **100**, 220404 (2008).

[7] I. Pikovski, M. Zych, F. Costa and a. Brukner. Universal decoherence due to gravitational time dilation. *Nature Physics* **advance online publication** (2015).

[8] G. Balasubramanian *et al.* Ultralong spin coherence time in isotopically engineered diamond. *Nat Mater* **8**, 383 (2009).

[9] M. Zhong *et al.* Optically addressable nuclear spins in a solid with a six-hour coherence time. *Nature* **517**, 177 (2015).

[10] C. Pfister *et al.* Understanding nature from experimental observations: a theory independent test for gravitational decoherence. *arXiv:1503.00577 [gr-qc, physics:quant-ph]* (2015).

[11] H. Wiseman. Physics: Bell's theorem still reverberates. *Nature* **510**, 467 (2014).

[12] S. Aaronson and J. Watrous. Closed timelike curves make quantum and classical computing equivalent. *Proceedings of the Royal Society of London A: Mathematical, Physical and Engineering Sciences* **465**, 631 (2009).

[13] P. H. Eberhard. A realistic model for quantum theory with a locality property. W. Schommers (editor), *Quantum Theory and Pictures of Reality*. Springer Berlin Heidelberg (1989), 169–215.

[14] D. Salart, A. Baas, C. Branciard, N. Gisin and H. Zbinden. Testing the speed of 'spooky action at a distance'. *Nature* **454**, 861 (2008).

[15] B. Cocciaro, S. Faetti and L. Fronzoni. A lower bound for the velocity of quantum communications in the preferred frame. *Physics Letters A* **375**, 379 (2011).

[16] J.-D. Bancal *et al.* Quantum non-locality based on finite-speed causal influences leads to superluminal signalling. *Nature Physics* **8**, 867 (2012).

[17] T. Scheidl *et al.* Violation of local realism with freedom of choice. *Proceedings of the National Academy of Sciences* **107**, 19708 (2010).

[18] J. Gallicchio, A. S. Friedman and D. I. Kaiser. Testing bell's inequality with cosmic photons: Closing the setting-independence loophole. *Physical Review Letters* **112**, 110405 (2014).

[19] H. J. Kimble. The quantum internet. *Nature* **453**, 1023 (2008).

[20] N. H. Nickerson, Y. Li and S. C. Benjamin. Topological quantum computing with a very noisy network and local error rates approaching one percent. *Nature Communications* **4**, 1756 (2013).

[21] D. Rosset *et al.* Nonlinear bell inequalities tailored for quantum networks. *Physical Review Letters* **116**, 010403 (2016).

[22] C. Kurtsiefer, S. Mayer, P. Zarda and H. Weinfurter. Stable solid-state source of single photons. *Physical Review Letters* **85**, 290 (2000).

[23] L. Robledo *et al.* High-fidelity projective read-out of a solid-state spin quantum register. *Nature* **477**, 574 (2011).

[24] L. Childress *et al.* Coherent dynamics of coupled electron and nuclear spin qubits in diamond. *Science* **314**, 281 (2006).

[25] W. Pfaff *et al.* Demonstration of entanglement-by-measurement of solid-state qubits. *Nature Physics* **9**, 29 (2013).

[26] T. H. Taminiau, J. Cramer, T. v. d. Sar, V. V. Dobrovitski and R. Hanson. Universal control and error correction in multi-qubit spin registers in diamond. *Nature Nanotechnology* **9**, 171 (2014).

[27] E. Togan *et al.* Quantum entanglement between an optical photon and a solid-state spin qubit. *Nature* **466**, 730 (2010).

[28] H. Bernien *et al.* Heralded entanglement between solid-state qubits separated by three metres. *Nature* **497**, 86 (2013).

[29] W. Pfaff *et al.* Unconditional quantum teleportation between distant solid-state quantum bits. *Science* **345**, 532 (2014).

[30] B. Hensen *et al.* Loophole-free bell inequality violation using electron spins separated by 1.3 kilometres. *Nature* **526**, 682 (2015).

[31] M. S. Blok, N. Kalb, A. Reiserer, T. H. Taminiau and R. Hanson. Towards quantum networks of single spins: analysis of a quantum memory with an optical interface in diamond. *Faraday Discussions* **184**, 173 (2015).

[32] T. v. d. Sar *et al.* Deterministic nanoassembly of a coupled quantum emitter-photonic crystal cavity system. *Applied Physics Letters* **98**, 193103 (2011).

[33] J. Riedrich-Möller *et al.* One- and two-dimensional photonic crystal microcavities in single crystal diamond. *Nature Nanotechnology* **7**, 69 (2012).

[34] R. Albrecht, A. Bommer, C. Deutsch, J. Reichel and C. Becher. Coupling of a single nitrogen-vacancy center in diamond to a fiber-based microcavity. *Physical Review Letters* **110**, 243602 (2013).

[35] Y. Chu *et al.* Coherent optical transitions in implanted nitrogen vacancy centers. *Nano Letters* **14**, 1982 (2014).

[36] Y. Shen, T. M. Sweeney and H. Wang. Zero-phonon linewidth of single nitrogen vacancy centers in diamond nanocrystals. *Physical Review B* **77**, 033201 (2008).

[37] Y. Colombe *et al.* Strong atom-field coupling for bose-einstein condensates in an optical cavity on a chip. *Nature* **450**, 272 (2007).

[38] D. Hunger *et al.* A fiber fabry-perot cavity with high finesse. *New Journal of Physics* **12**, 065038 (2010).

[39] E. Janitz *et al.* Fabry-perot microcavity for diamond-based photonics. *Physical Review A* **92**, 043844 (2015).

[40] R. Ikuta *et al.* Wide-band quantum interface for visible-to-telecommunication wavelength conversion. *Nature Communications* **2**, 1544 (2011).

[41] S. Zaske *et al.* Visible-to-telecom quantum frequency conversion of light from a single quantum emitter. *Physical Review Letters* **109**, 147404 (2012).

[42] F. Dolde *et al.* Room-temperature entanglement between single defect spins in diamond. *Nature Physics* **9**, 139 (2013).

Summary

In this thesis we experimentally investigate quantum nonlocality: entangled states of spatially separated objects. Entanglement is one of the most striking consequences of the quantum formalism developed in the 1920's; the predicted outcomes of independent measurements on entangled objects reveal strong correlations that cannot be explained by classical physics. Early on, such predictions led physicists to doubt the validity and completeness of quantum theory. At the same time, entanglement is a key resource for applications in quantum information processing and a pre-requisite for many tasks in quantum communication and computation.

This thesis attempts to answer two application driven questions: Firstly, can we generate useful entangled states of solid state spins for applications in quantum information processing? Secondly, can we use such entangled states as a resource to teleport an unknown quantum state?

Finally, we ask a foundational question: Are our entangled states indeed inconsistent with the classical notions of free choice, locality and realism? Can we prove this experimentally, under the minimal assumptions of a loophole-free Bell test?

To answer these questions we use single spins in ultra-pure diamonds. In particular, we use the electronic and nuclear spins associated with single nitrogen-vacancy (NV) defects. The NV centre is a point defect in diamond, consisting of a substitutional nitrogen (N) atom and a neighbouring missing carbon atom (vacancy, V). The NV centre possesses bound electronic states, whose energy levels lie well within the bandgap of the diamond host and whose spin degree of freedom can be used as a quantum bit (qubit). Because of the large diamond bandgap and the 99% spin free ^{12}C environment, the electronic spin qubit has exceptional coherence properties even at room temperature. Optical and microwave fields allow control of the electronic spin, which in turn allows control of nearby nuclear spins (the host nitrogen nuclear spin, and nearby ^{13}C spins). At liquid helium temperatures, spin-preserving optical transitions provide a powerful optical interface to the electronic spin, allowing, for example, projective readout of the spin state.

By employing a protocol where entanglement is heralded by the detection of a single photon from each of two NV centres in diamonds separated by three metres, in Chapter 3 we find we can answer the first question in the affirmative. We show for the first time heralded entanglement between solid state quantum systems separated by a human-scale distance.

Then, by combining the heralded entanglement with a deterministic local Bell state measurement and fast feed-forward, in Chapter 4 we show for the first time unconditional quantum teleportation over human-scale distances. We teleport an unknown quantum state from a nuclear spin in one diamond to an electronic spin in a diamond three meters away.

Finally, in Chapter 5, by employing techniques from the previous chapters, we implement the first loophole-free Bell test. We separate two diamonds by 1.3 kilometres and optimize all operational fidelities, collection efficiencies and rates. This allows us to generate heralded entanglement between them approximately once an hour. The distance provides us with time to read out the electronic spin state in each diamond, faster than any lightlike signal could travel between them. The high-fidelity entangled state preparation and spin readout are sufficient to violate the Clauser-Horne-Shimony-Holt Bell-inequality. Combined with fast random number generators and a robust statistical analysis, we find a significant rejection of the local-realist hypothesis, without requiring additional experimental assumptions.

The results in this thesis open the door to various applications in quantum information processing. In particular, a remote photonic entangling operation may enable future quantum networks. In such a network the nodes would be formed by the NV centre's combined electronic and nuclear spin register. The nodes would be linked by photonic entanglement operations. Such a network could be used for long distance secure communication, provide a connection between separated quantum computers, or form the basis of a fault tolerant quantum computer by itself. Furthermore, a loophole-free Bell test demonstrates the possibility to do device independent randomness generation and key distribution, that could form the basis for future secure communication channels.

Samenvatting

In dit proefschrift bestuderen we met behulp van experimenten de niet-lokale structuur van de quantum theorie: ruimtelijk van elkaar verwijderde deeltjes in een verstrengelde toestand. Verstrengeling is een van de meest opvallende eigenschappen van het quantum-formalisme, zoals dat zich in de jaren twintig van de vorige eeuw ontwikkelde. De voorspelde uitkomsten van onafhankelijke metingen op verstrengelde deeltjes zouden sterke correlaties vertonen, die geen klassieke uitleg verstonden. Al snel leidden deze voorspellingen tot twijfel bij natuurkundigen over de juistheid en compleetheid van de quantum theorie. Tegelijkertijd bleek verstrengeling een kerningrediënt te zijn voor vele toepassingen in de quantum informatie technologie en zelfs een vereiste voor bepaalde onderdelen van de quantum computer.

Het proefschrift tracht twee toepassingsgerichte vragen te beantwoorden: Ten eerste, is het mogelijk verstrengelde toestanden te genereren tussen spins in de vaste-stof, die nuttig zijn voor toepassingen in de quantum informatie technologie? Ten tweede, kunnen we dergelijke verstrengelde toestanden inzetten om een onbekende quantum toestand te teleporteren? Daarnaast stellen we een fundamentele vraag: Zijn onze verstrengelde toestanden inderdaad in conflict met de klassieke premissen van vrije keuze, lokaliteit en realisme? Kunnen we dit experimenteel aantonen, met de minimale aannames van een *loophole-free Bell test*?

Om deze vragen te beantwoorden gebruiken we individuele spins in ultra-puur diamant. Om precies te zijn gebruiken we de elektronspin en kernspins horende bij individuele stikstof-holte defecten (*Nitrogen-Vacancy centres, NV*). Het NV-defect bestaat uit een stikstofatoom op de plek van een koolstof atoom in het diamant kristalrooster, met een naburig missend koolstofatoom. Het defect beschikt over gebonden elektronen-toestanden, waarvan de energieniveaus ruimschoots binnen de *band gap* van het diamant liggen. De spintoestand van deze elektronen kunnen tevens gebruikt worden om een quantum-bit (*qubit*) in te coderen. Door de beschermende band gap en de 99% kernspin-vrije ^{12}C omgeving heeft zo'n elektronspin-qubit uitzonderlijk goede coherentie-eigenschappen, zelfs bij kamertemperatuur. Met behulp van optische- en microgolfvelden kunnen we controle uitoefenen op de elektronspins. Tevens kunnen we via het elektronspin ook de kernspin van het stikstof atoom en nabijgelegen ^{13}C kernspins controleren en gebruiken als qubit. Bij vloeibaar helium-temperaturen kunnen we spin-behoudende optische transities gebruiken van het elektronspin, waarmee we bijvoorbeeld de spin projectief kunnen uitlezen. Met behulp van een protocol waarbij verstrengeling wordt aangekondigd door de detectie van een enkel foton van elk van twee NV-centra in verschillende diamanten, drie meter van elkaar verwijderd, kunnen we in Hoofdstuk 3 de eerste bovenstaande vraag bevestigend beantwoorden. We demonstreren voor het eerst aangekondigde verstrengeling over menselijke afstanden tussen vaste-stof quantum systemen.

Daarna combineren we de verstrengelingsoperatie met een deterministische lokale

meting in de Bell basis en snelle feed-forward, zodat we in Hoofdstuk 4 voor het eerst onvoorwaardelijke quantum teleportatie over een menselijke afstand kunnen demonstreren. We teleporteren een onbekende quantum toestand van een kernspin in een diamant naar een elektronspin in een diamant drie meter verderop.

Ten slotte implementeren we in Hoofdstuk 5, met behulp van de technieken ontwikkeld in de voorgaande hoofdstukken, de eerste loophole-free Bell test. We plaatsen twee diamanten 1.3 kilometer uit elkaar en optimaliseren de accuraatheid van de gebruikte operaties, de collectie-efficiëntie en snelheid van herhalingen, resulterend in een succesvolle verstrengelingsoperatie tussen de elektronspins, ongeveer eens per uur. De afstand is voldoende om onze elektronspins uit lezen voordat een signaal met de lichtsnelheid van de een naar de ander kan reizen. De accuraatheid van de verstrengelde toestand en spinuitlezing zijn voldoende om de Clauser-Horne-Shimony-Holt Bell ongelijkheid te schenden. In combinatie met snelle random nummer generatoren en een robuuste statistische analyse vinden we dan een significante afwijzing van de lokaal-realistische nulhypothese, zonder verdere experimentele aannames te hoeven doen.

De resultaten in dit proefschrift bieden verscheidende mogelijke toepassingen op het gebeid van de quantum informatie technologie. Een verstrengelingsoperatie die met behulp van fotonen over een grote afstand verstrengeling tot stand kan brengen kan een toekomstig quantumnetwerk mogelijk maken. In zo'n netwerk zouden de knooppunten gevormd kunnen worden door de qubits van het NV-defect: elektronspin en kernspins. De knooppunten zouden verbonden kunnen worden door de verstrengelingsoperatie die met behulp van fotonen. Een quantum netwerk kan gebruikt worden voor inherent veilige communicatie over lange afstanden, een verbinding vormen tussen toekomstige quantum computers, of zelf de basis vormen van een quantum computer. Daarnaast toont een loophole-free Bell test aan dat het mogelijk is quantum protocollen voor veilige communicatie en random nummer generatie op zo'n manier te doen dat men geen aannames hoeft te doen over de apparaten die het protocol fysiek implementeren.

Acknowledgements

I am very grateful to have been able to work in such an inspiring environment that is QT. It seems hard to imagine a place with a more enthusiastic, motivated group of staff and researchers, working on such a broad variety of systems. Already during my time as a Master student in Ronald's group I experienced the QT-family-feeling at first hand, attending my first PhD defences with ensuing borrels and the famous QT-uitje to Geneve and beyond. Working hard and playing hard for the next 4 years was indeed a great experience, and I have many people to thank for this inspiring and exciting time.

Firstly, many thanks to my amazing promoter: Ronald, you are an excellent scientist, supervisor and manager. I know of no-one with a better skill at imposing intrinsic motivation. I greatly enjoyed our discussions on Bell, the measurement problem and many other subjects.

I want to thank off course Team Diamond! Toeno and Gijs it was great to join the group that you helped build, and follow in your footsteps! Toeno, I remember being inspired by your hospitality during the first Diamond dinner I attended. Lucio, thanks for helping me with my MSc thesis project, and showing me how you programmed the first CR check in the Adwin. Lily, your guidance during my MSc thesis project was indispensable, not to mention the Insecure String Pickle watching over us in the lab. Andreas, Anaïs, Norbert, Hannes, Machiel and Just, I am very proud to have formed the Bell team with you guys, and for sticking with what became a long-distance marathon experiment. Just, I enjoyed very much supervising your MSc project! It was certainly not an easy project but crucial to the success of Bell. I will always remember you pointing the end of one of the long fibers at the webcam to get some light across the campus! Tom and Mark, it was great to be able to work with you on your BSc projects, with very useful results already (Hermite!), or in the near future (Carbon Grape?). Tim, I think your precision, knowledge, perseverance were vital to Diamond's successes of the past years, thanks again for all the good discussions and comments. Good luck with your new lab! Julia, thanks for all the good talks, joint complaining and then concluding it's not so bad. I am sure you will find your way in science, science-communication or anything really, and be very successlful! Cristian I can still remember the fantastic spaghetti you cooked after the Leiden Singel-loop - I guess it was like making a sandwich for you. Wolfgang, for being Wolfgang, but also for your programming and organising skill and your enthusiasm. Machiel for indeed epic debugging sessions, train discussions and more generally for making my life decisions by example one year in advance. Hannes I have learned so much from you, while you were still my MSc supervisor, and after that while working on LDE together. I daresay we were quite a good team in the lab. Above all I am very happy for the good times we had outside the lab, and I'm sure it's not the last of it! Thanks to all the other former Team Diamond members for contributing to the lab as it is.

I am very grateful for our recently gained, indispensable support on the theoretical side! Thanks to Stephanie for always dropping in on her way out to see how the experiment was going, David for immense precision and accuracy, and both of you for your patience in answering silly experimentalist questions. Thanks to Kenneth Goodenough for being a good uniform Twitter-Justin-Bieber-Based random number generator.

Many thanks belong to the greater Q(u)-T(ech) family. None of the work in this thesis could have been done without the great support staff at QT: Thanks to Bram for great historical knowledge (the tunnel!) and the characteristic hallway sound. Special thanks to the genius Raymond Schouten, equally for helping me countless times with quick-fixes and great ideas on electronics, but also for discussing the latest improvements of the ultimate synthesizer. Thanks to Raymond jr. en Marijn for building and helping out with the CPLD and random number generators. Jelle, Remco and Mark, you form a solid technical basis for QT. Many thanks to the excellent support of Marja, Yuki and later Chantal, Simone and Heera! Maaike, Visa, Chris, Hannes and Machiel, what a great pleasure to form the second incarnation of the QT band with you, we did rock! Vincent, Stephanie, Johan it was great fun to organize the Ardennen QT-uitje with you. Thanks to my great (former) roomies at QT!

Many other enthusiastic people helped to make the Bell project a reality. A very big thanks to René Zwagerman for being the pivot between the many parties involved in the logistics of getting two new labs on campus and the fibre connection ready within the timespan of only a few months. Thanks to the mythical Teus for popping out of the TU underground tunnel at the right time, and for supervising the installation of our precious cable together with Rico. Thanks to "de mannen" at RID: Renee and Iko for answering countless questions and helping with the intricately complex structure that is the TU Delft access-card-system. The RID security for allowing me in on Sundays and only frowning when we stumbled in with another car-or-bike-load of laboratory equipment, or exited through the revolving door with a desktop PC under the arm. Thanks to Morgan and co-workers at ICFO, and thank you Carlos for building the QRNGs and bringing them here in person. Michel van Baal: thank you for teaching me how to get from Victoria Beckham's boob-job to secure quantum communication, smoothly, in one sentence; and of course for providing us with that fantastic fraudulent statue.

Thanks to all the regular Monday-soccer players, especially to Felix and Ruben for being team-captains, if we do our best I think we can still become first this season (of the loser competition;).

I am also grateful to Julia, Niels, Peter, Anaïs for proofreading parts of my thesis!

Thanks to all my teachers: from primary school until now - special thanks to Kees Hooyman for setting up the course on computational modelling that got me hooked on physics; the lecturers of the BSc- and MSc-programme in Delft, and those in

Cambridge; Jeremy Butterfield for getting me interested in the measurement problem; Roel at Topdesk for teaching me the morals of good programming. Thanks also to everyone at the VvTP, and Bestuur 76 in particular, I learned many things there. Lieven and Lan, it was great to do my BSc project under your supervision. I was so happy I could do my own low-temperature measurements at the time. You taught me a lot and made sure I was keen to return to QT later for my MSc project!

Thanks to all my friends, family and family in law for persisting in asking me questions about my research! I wish I could explain it better!

Evert, Thea, Hanna en Joris, lieve Rosanne, dank dat jullie er altijd voor me zijn.

List of Publications

1. *Loophole-free Bell test using electron spins in diamond: second experiment and additional analysis.*
   B. Hensen, N. Kalb, M.S. Blok, A.E. Dréau, A. Reiserer, R.F.L. Vermeulen, R.N. Schouten, M. Markham, D.J. Twitchen, D. Elkouss, K. Goodenough, S. Wehner, T.H. Taminiau, and R. Hanson.
   Submitted. Preprint at arXiv:1603.05705.

2. *Een Belltest met alle achterdeurtjes dicht.*
   B. Hensen and R. Hanson
   Nederlands Tijdschrift voor Natuurkunde **82**, 110 (2016).

3. *Loophole-free Bell inequality violation using electron spins separated by 1.3 kilometres.*
   B. Hensen, H. Bernien, A.E. Dréau, A. Reiserer, N. Kalb, M.S. Blok, J. Ruitenberg, R.F.L. Vermeulen, R.N. Schouten, C. Abellán, W. Amaya, V. Pruneri, M.W. Mitchell, M. Markham, D.J. Twitchen, D. Elkouss, S. Wehner, T.H. Taminiau, and R. Hanson.
   Nature **526**, 682 (2015).

4. *Repeated quantum error correction on a continuously encoded qubit by real-time feedback.*
   J. Cramer, N. Kalb, M.A. Rol, B. Hensen, M.S. Blok, M. Markham, D.J. Twitchen, R. Hanson, and T.H. Taminiau.
   In press.

5. *Unconditional quantum teleportation between distant solid-state qubits.*
   W. Pfaff, B. Hensen, H. Bernien, S. van Dam, M.S. Blok, T.H. Taminiau, M.J. Tiggelman, R.S. Schouten, M. Markham, D.J. Twitchen, and R. Hanson.
   Science **345**, 532 (2014).

6. *Heralded entanglement between solid-state qubits separated by three meters.*
   H. Bernien, B. Hensen, W. Pfaff, G. Koolstra, M.S. Blok, L. Robledo, T.H. Taminiau, M. Markham, D.J. Twitchen, L. Childress, and R. Hanson.
   Nature **497**, 86 (2013).

7. *High-fidelity projective read-out of a solid-state spin quantum register.*
   L. Robledo, L. Childress, H. Bernien, B. Hensen, P.F.A. Alkemade, and R. Hanson
   Nature **497**, 86 (2013).

Curriculum Vitae

Bas Jorrit Hensen

Jul. 20, 1986	Born in Leiden, The Netherlands.
1998 - 2004	Secondary school, St. Bonifatiuscollege, Utrecht.
2005 - 2008	B. Sc. Applied Physics, *Delft University of Technology.* Graduation research in the Quantum Transport group. Supervisor: Prof. dr. ir. L.M.K. Vandersypen.
2009 - 2010	Master of Advanced Study in Mathematics, *University of Cambridge.*
2010 - 2012	M. Sc. Applied Physics, *Delft University of Technology.* Graduation research in the Quantum Transport group. Supervisor: Prof. dr. ir. R. Hanson.
2011	Research internship, *FOM Institute for Plasma Physics.* Research project in the Plasma surface interactions group. Supervisor: Dr. G. De Temmerman.
2012 - 2016	Ph.D. researcher, *Delft University of Technology.* Subject: Quantum Nonlocality with Spins in Diamond Group: QuTech and Quantum Transport, Kavli Institute of Nanoscience. Promoter: Prof. dr. ir. R. Hanson.

Casimir PhD series 2016-11